The Fault in our Hill: Characterisation of the Rangitawa Tephra, and Insight into Tectonic Influences at Hillcrest Road.

A thesis submitted in partial fulfilment
of the requirements for the degree
of
Master of Science
at
The University of Waikato
by
Vittoria Kate Gibbons

THE UNIVERSITY OF
WAIKATO
Te Whare Wānanga o Waikato

2020

Abstract

This study aimed to identify deformation and characterise the Rangitawa Tephra in terms of geomechanical and geochemical properties, and relate these properties to the deformation potential/activity. It was hypothesised there is a fault present in the site at 59 Hillcrest Road, and that the Rangitawa Tephra deforms plastically and accommodates deformation thereby reducing the amount of deformation in the geological units above.

Field analyses included stratigraphic observations, unit descriptions, structural observations and anomaly identification, sensitivity measurements, and description of soft sediment deformation structures. Laboratory analyses consisted of particle-size, mineralogy, chemistry, and microstructure analyses and geomechanical behaviour identification through Atterberg Limits and Triaxial shear testing.

Field analyses showed the presence of soft sediment deformation in the form of offset and deformed bedding at the base of the Rangitawa Tephra unit, and in the Hamilton Ash Formation above, along with a significant offset of approximately 6 metres within the cutting at 59 Hillcrest Road. This is inferred to be a normal fault, with the surrounding deformation seismites resulting from seismic triggers in the area along this fault plane.

Laboratory analyses were used to characterise the Rangitawa Tephra at Hillcrest Road based on geomechanical, chemical, and mineralogical properties indicated the Rangitawa is bimodal extra-fine silt and extra-fine sand with an average of medium silt texture, behaving as a low compressibility silt. The clay mineralogy present as halloysite, dehydrated in Atterberg Limits testing, but hydrated otherwise. Triaxial shear testing identified the Rangitawa Tephra at Hillcrest to be of normally consolidated material, exhibiting ductile-plastic characteristics. The properties indicated during laboratory analyses were used to provide explanations for the deformation structures observed in the exposure at 59 Hillcrest Road. Field analyses along with the laboratory characterisation of the Rangitawa Tephra confirm the presence of a fault plane at the exposure.

The thesis concludes the Rangitawa Tephra exhibits plastic deformation characteristics, presenting the potential to exhibit cyclic softening. These findings confirm the presence of ductile displacement, and support the soft sediment deformation structures observed at the base of the Rangitawa Tephra, and in the Hamilton Ash formation, are the direct result of paleoseismic influences within the area. It can then be suggested this fault zone may be active (displacement younger than 100 ky.) (GNS, 2017). The ductile plastic characteristics of the Rangitawa Tephra suggests deformation within and above this unit could be present, masked by the atypical displacement features and reduced by the accommodated deformation by the Rangitawa Tephra, suggesting the inferred ages on other faults found within the basin may be much younger than expected.

Acknowledgements

To my supervisor, Dr Vicki Moon for always believing in me. COVID-19 really proved a hurdle and I am so very thankful you were always understanding and supportive. The best supervisor a girl could want.
Field and laboratory technicians; Kirsty Vincent, Annette Rogers, Dean Sandwell, Chris Morcom, Renat Radosinsky, and academics Dr Adrian Pittari, Dr David Lowe
Francesca Spinardi and Tom Robertson, along with Jordanka Chaneva and Dr Max Kluger for all your academic support and tolerating a fair few stupid questions. Francesca, a special extra shout out to you for saving my butt when I tore the ligament in my thumb; without you my field work would never have been finished. I hope my thesis supports your research when you finally make it back from America when COVID-19 is long behind us.

Thank you to Phoenix Civil – Inniss Anderson and Craig McBean and Co. for allowing me to be on site. Especially to their digger driver Mike for constantly helping me out digging holes and scraping areas, not to mention for holding off topsoiling while I was scrambling around finalising my fieldwork. The banter on poor weather days was much appreciated. You honestly kept my mood up on those cold windy days, and for you I am thankful.

To my fellow MSc students; Ashley, Anya, George, and best mate Thomas Austin. Always easier to study when you know everyone is struggling just the same. Moreover, to my friends; Jacob, Richard, Frankie, and Scott for keeping me entertained, and Lev and Winnie for always ensuring I was safe and sane, and for always letting me study at your house on stressful days. I am eternally grateful and could not have done it without you.
My cat Millie for her unwaivering support (not that she has much choice) and constant purrs. Albeit, a distraction from my work and the main reason I could not focus at home.

Family, in particular my dad who supported me financially, mentally, and emotionally while I studied, and my little sister, Jette, who aggressively reminded me I could do anything I set my mind to. It's been a bumpy ride, through COVID-19, pets passing away, and my recent ADHD diagnosis, but together we made it here.

No doubt I've missed someone, so I apologise but let it be known everyone I know got me here and I am appreciative of all of you.

Table of Contents

List of Figures

List of Tables

Chapter 1

Introduction

1.1 Background of research

New Zealand experiences seismic activity resulting from the proximity to an active subduction zone between the Pacific and Indo-Australian tectonic plates. In fact, New Zealand lies directly above this zone which results in common volcanism, and seismic hazard. The National Seismic Hazard Model holds a relatively low seismic hazard for the Hamilton Basin, resulting from the lack of recorded tectonic activity (Spinardi *et al.* 2019). Recent evidence has suggested the seismic rating may require review as faulting in the Hamilton Basin has been established.

In 2015, the first fault was identified in a residential subdivision near Flagstaff-Rototuna (de Lange *et al.,* 2015). The discovery indicated potential for more unknown/unstudied tectonic features within the basin. LiDAR data and geomorphic signatures, along with sidescan and multibeam data, seismic profiling, and resistivity surveys, and most importantly characterisation of many cuttings exposing tectonic deformation (Campbell, 2016; Spinardi, 2017) have since identified 26 zones of interest expressing tectonic deformation (Moon and de Lange, 2017). As a research group, we are now confident the basin composes a complex network of fault zones running approximately SW-NE, and are presently at the point of understanding the nature and patterns, along with timing of movements on the fault zones. One area identified in the surveys carried out by Spinardi *et al*. (2017) inferred a fault zone running through Hamilton Airport-Mystery Creek area, striking north-east with a branch inferred parallel to the ridgeline along which Hillcrest Road runs.

In the summer of 2018-2019, a subdivision site opened up near the inferred fault zone in the south of Hamilton, and later in the year (2019), earthworks at the site produced a cutting perpendicular to the strike of the inferred fault zone. This cutting provided an opportunity to investigate the area of interest perpendicular to Hillcrest Road. Inniss Anderson and Craig McBean of Phoenix Civil Ltd. granted consent to undertake a non-invasive investigation of the site during their groundwork phase of development.

A key unit for research of the faulting in the Hamilton Basin is the Rangitawa Tephra, an important widespread stratigraphic marker. The Rangitawa Tephra in most faulted areas within the Hamilton Basin is not apparently offset, not with brittle deformation at least. If the Rangitawa Tephra is proven to exhibit plastic or ductile characteristics, it is possible to assume this unit could bend rather than fracture. This would affect how recently active the fault was inferred to be, thereby, suggesting some of the newly discovered faults could have been active more recently than initially suspected.

1.2 Aims and Objectives

The aim of this study is to characterise stratigraphy and materials at the Hillcrest Road site to determine whether or not deformation features indicating seismic activity are present. In particular, I aim to characterise the Rangitawa Tephra unit in terms of mechanical behaviour.

To achieve this aim, the following objectives are defined;

1) to map and describe stratigraphic relations of the main units in the field;
2) to describe material characteristics of key stratigraphic units;
3) to describe any evidence of seismic deformation in the field;
4) to sample the Rangitawa Tephra unit, and undertake laboratory tests to define the key geomechanical properties.

1.3 Thesis Structure and Chapter Layout

Chapter Two consists of a literature review assessing and summarising literature regarding the formation of the Hamilton Basin, the geomorphology within the basin, and introducing the units found within the low-rolling hills on which my study area exists. The chapter also briefly introduces tectonic geomorphology, before covering a portion of soft sediment deformation.

Chapter Three outlines the methodology used in field and laboratory work during this project.

Results are presented in Chapters Four and Five. Chapter Four outlines the results from field analyses, while Chapter Five presents results from laboratory analyses.

Chapter Six provides evaluation and discussion of the results presented in chapter four and five. This chapter will also discuss the validity of the findings and provide comparisons with existing literature.

Chapter Seven will summarise and conclude the project, before identifying gaps and failures, and putting forth recommendations to address this project and potential future related research.

Chapter 2

Literature Review

2.1 Introduction

The chapter reviews published literature regarding the Hamilton Basin and tectonic influences. Section 2.2 introduces and overviews the formation of the Hamilton Basin, and Section 2.3 presents the geology and geomorphology of the Hamilton Basin, detailing the geological units present within the Hamilton Hills, outlining the ignimbrites of the Walton Subgroup, and ash units of the Kauroa Ash Formation, Hamilton Ash Formation, and post-Hamilton Ashes. Section 2.4 discusses tectonic deformation, including the geometry of faults, fault zones and anatomy, and Section 2.5 describes soft sediment deformation such as seismites. Section 2.6 discusses the current knowledge of deformation in the Hamilton Basin, including details of the known faults within the basin. Section 2.7 summarises the literature review.

2.2 Hamilton Basin

2.2.1 Introduction to the Hamilton Basin

The Hamilton Basin is the northern part of a large, oval-shaped depression centred about Hamilton City (Kamp and Lowe, 1981; McCraw, 2011). The entire basin is 80-90 kilometres long and 40 kilometres wide, running along the present path of the Waikato River. The southern margin runs through the Hinuera Gap in the southeast, across west to just south of Otorohanga. The northern boundaries lie from just north of Orini in the northeast, and ends just before the Taupiri Gorge in the north-west (Kamp and Lowe, 1981; McCraw, 2011).

The Hamilton Basin is bounded mostly by semi-continuous ranges about 300 metres high, formed of Mesozoic-aged basement strata in the north and east (Kamp and Lowe, 1981; McCraw, 2011), and on the south-western margin the basin is partially overshadowed by the late Pliocene – early Pleistocene volcano, Mount Pirongia (Kamp and Lowe, 1981). The basin provides a receptacle for terrestrial sediments, from both extrabasinal sources such as the Taupo Volcanic Zone, Coromandel Volcanic Zone, and Mount Taranaki, and interbasinal sources such as erosion of the bounding ranges. The landscape within the Hamilton Basin has evolved over millions of years with episodes of tectonism, deposition, and erosion (Kamp and Lowe, 1981; Kear and Schofield, 1983; Kleyburg, 2015).

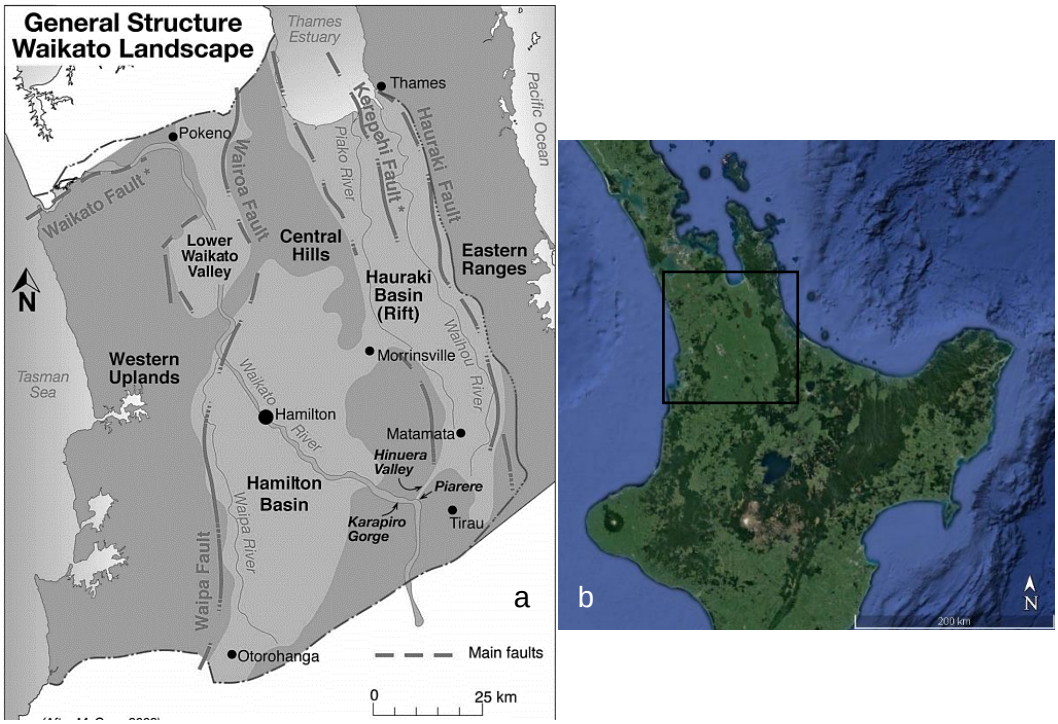

Figure 2.1a: Map of the Hamilton Basin from Lowe (2010). 2.1b: Position of Waikato Basin relative to North Island, New Zealand from Google Earth Pro

Formation of the Hamilton Basin

The bulk of the landscape within the Hamilton Basin is most likely a result of fault movement in the late Miocene period (Kear and Schofield, 1978). Physiographically, the basin is a fault-bounded area of late-Tertiary to Pleistocene age (Kamp and Lowe, 1981; Kleyburg, 2015). The basement is downfaulted 200 – 300 metres at the western margin as observed in displaced Tertiary strata overlapping younger Hokoniu rocks of the Hakarimata Ranges by *en echelon* normal faults trending N-NE. (Kamp and Lowe, 1981; Kear and Schofield, 1978). Elsewhere on the margins, faulting is not apparent due to the absence of Tertiary outliers. Faulting is hidden by a thick cover-bed of Pleistocene age sediments. The exact position of the Waipa fault is unknown but inferred to run through the western flanks of Pirongia volcano trending north-east parallel to the east of the Hakarimata Ranges (Kamp and Lowe, 1981). The Waipa fault and late-Tertiary displacement was inferred by variation in basement elevation across the basin as gravity and drillhole data suggested the Waipapa basement terrane occurs at variable depth, up to c. 2000 metres in addition to the 300 metre offset observed in surface topography (Kamp and Lowe, 1981). Seismic, gravity, and test wells indicate the greywacke basement is steeply dipping north-west, with a thicker sedimentary cover bed in the north-west relative to elsewhere in the basin (de Lange and Moon, 2017). A gravity anomaly map expressing the basin depth variations is illustrated in **Figure 2.2.** The greywacke surface slowly eroded to produce a surface of low relief which peat bogs formed in low-lying wet depressions

within the surface. Approximately 30 Mya, the Waikato area sank and marine deposits accumulated, later becoming sandstones, siltstones, and limestones, and the peat bogs under pressure began to form coal measures. Uplift of the land approximately 5 Mya by earthquake and plate tectonics raised the land and produced north-south running fault blocks which later eroded and weathered to ranges with lowlands between. Volcanic activity broke out ~2 Mya, depositing ignimbrites and ash across the land surface, filling in the lowlands between the ranges. The Walton Subgroup was deposited during this time, beginning with the distal ignimbrites of the Puketoka Formation which then eroded and the valleys filled by the fluvially reworked Karapiro Formation. Further erosion and weathering produced an unconformity on which the Kauroa Ash Formation was sequentially deposited, mantling the landscape, followed by another period of weathering and erosion of approximately 440 ky. The Hamilton Ash Formation, followed by the Post-Hamilton Ashes were then deposited. Volcanic Activity continued and deposited the Hinuera Formation which filled in the hill-and-valley topography with a thick cover of very-low relief volcanigenic alluvial plain, producing the present land surface **(Figure 2.3)**(Lowe, 2010; McCraw, 2011).

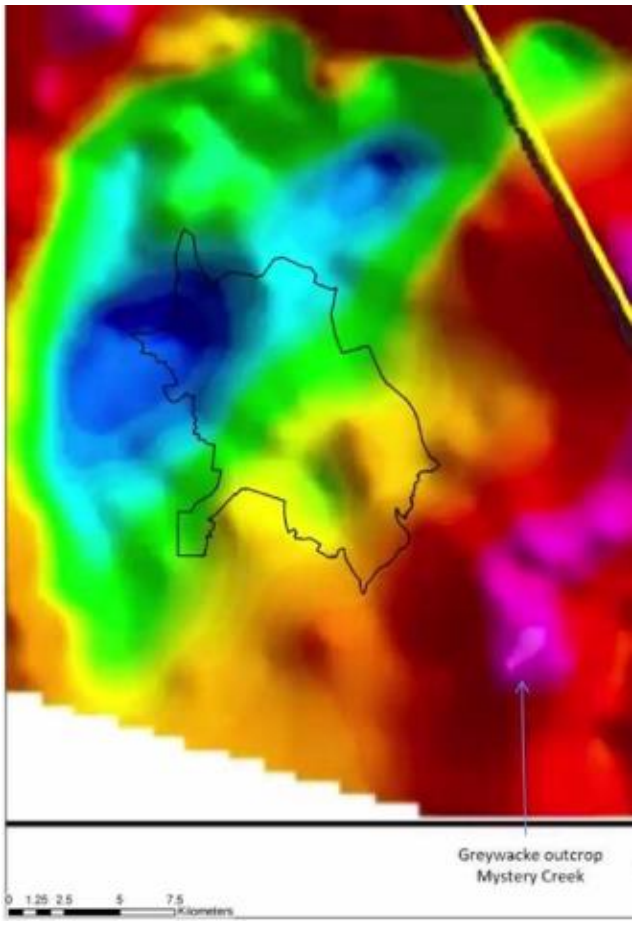

Figure 2.2.2 Gravity anomaly map of the Hamilton Basin from FrogTech in 2001 via Spinardi (2017). Dark blue indicates low, and pink indicates high gravity values. This indicates the northwest of the basin is relatively deep and filled with low density sediments, while the south-eastern portion is the upstanding basement near Mystery Creek.

2.3 Geology and Geomorphology of the Hamilton Basin

The Hamilton Basin is comprised of four main geomorphological units. These four include the low rolling hills, commonly known as the 'Hamilton Hills', low angle flattish alluvial plains containing micro-relief features of low mounds and depressions formed from deposition by the ancestral braided Waikato River, low terraces adjacent to the present Waikato River position, and gullies cut into the plains or terraces draining to the Waikato River **(Figure 2.3)** (Lowe, 2010). As this project is occurring on one of the 'Hamilton Hills', the low rolling hill features and geology will be of greatest focus within this literature review.

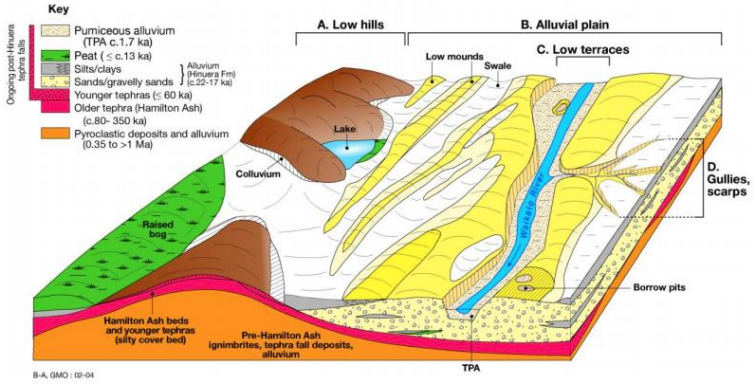

Figure 2.3: Landscape Units and geological materials of the Hamilton Basin (Lowe, 2010).

Hamilton Hills

The basin contains a system of low ridges and isolated hills. In the south near Te Awamutu the hills are semi-continuous ridges 30-60 above the present valley floor. In the north-east the hills are widely spread amongst the Pleistocene volcaniclastic alluvial plains infilling the valleys (Kamp and Lowe, 1981). The hills are remnants of an ancient landscape more than a million years old (Lowe, 2010). These hills are spatially and temporally complex sharing a common sequence of ignimbrites, tephras, and weathered loess, c. 1.0 Ma (Lowe, 2010). The typical stratigraphic sequence through these hills includes the Walton Sub-group consisting of the Puketoka and Karapiro Formations, the Kauroa Ash Formation, followed by the Hamilton Ash Formation with the Rangitawa Tephra at the base, topped off by a sequence of thin ash layers collectively known as the Post-Hamilton Ashes (Kamp and Lowe, 1981). At the base, most hills contain cream-coloured ignimbrite deposits up to 10-20 metres thick. These ignimbrites may comprise of the Ongatiti Ignimbrite (c. 1.2 Ma), Rocky Hill Ignimbrite (c. 1.0 Ma), and the Kidnappers Ignimbrite (c. 1.0 Ma) (Lowe, 2010), and are often referred to as part of the Walton Sub-group (Kamp and Lowe, 1981; Kear and Schofield, 1983; McCraw, 2011).

Walton Sub-group

The Walton Sub-group consists of Pleistocene-aged clays and current-bedded pumiceous sands and massive unsorted soft pumiceous rocks assumed to be non-welded ignimbrites and tephra beds, reworked and redeposited by fluvial and alluvial processes (Kear and Schofield, 1978; Selby and Lowe, 1992; Edbrooke, 2005; McCraw, 2011). The Walton Sub-group has a high content of rhyolite and pumiceous materials distinguishing them from the younger Tauranga Group formations of the Hinuera Formation, Hauraki Clays, and Taupo Pumice Alluvium. The formations within the Walton Sub-group are often difficult to distinguish but are assumed to be separated by intraformational unconformities. Separation of two key units are most convenient for correlation and discussion (McCraw, 2011). The two units present within the Walton Sub-group are the Puketoka Formation, and the Karapiro Formation (Kear and Schofield, 1978; Kamp and Lowe, 1981; McCraw, 2011).

Puketoka Formation

The Puketoka Formation is the oldest of the Walton Sub-group, described to be white to grey coloured, with well-bedded and well-sorted sands and pumice conglomerates with interbedded fine deposits of tephra, which stain the material pinks and yellows. Weathering and stream erosion following deposition of the Puketoka Formation appears to have carved valleys within the formation, leaving behind high hills within the basin.

Karapiro Formation

Above the ignimbrite deposits is a sequence of current-bedded orange, reddish, and cream-coloured gravelly alluvially/fluvially reworked clays of the Karapiro Formation. The Karapiro Formation is believed to have been deposited by the meandering streams of the ancestral Waikato River (Kear and Schofield, 1978; Selby and Lowe, 1992; Lowe *et al.* 2001; Edbrooke, 2005; McCraw, 2011).

Weathering and stream erosion following deposition of the Walton Sub-group appears to have carved valleys within the formation, leaving behind only portions of high hills within the Hamilton Basin (Kamp and Lowe, 1981; Selby and Lowe, 1992; Lowe *et al.,* 2001; Edbrooke, 2005; McCraw, 2011).

Ashes

Kauroa Ash Formation

The silty clays of the Kauroa Ash Formation are present above, below, or interfingering the gravelly alluvial clays and the oldest are aged at 2.24 +/- 0.29 Ma (Lowe *et al.,* 2001). The uppermost bed of the Kauroa Ash Formation is a paleosol of very patchy, dark reddish-brown clayey weathered tephra c. 78 Ma in age. The materials are predominantly rhyolitic in composition and can be traced to late Coromandel Volcanic Zone volcanism, early Taupo Volcanic Zone volcanism, or a mixture of both amongst the units (Lowe *et al.,* 2001; Lowe *et al.,* 2011).

Hamilton Ash Formation

The Hamilton Ash Formation is a 3-6 metre thick sequence of seven units of rhyolitic tephras and loess beds, and associated paleosols. The beds are comprised of silty clays and clayey silts of brown and reddish-yellow colour, aged 340 to 60 Ka (Kamp and Lowe, 1981, Lowe, 2010; McCraw, 2011). The ashes lie unconformably over the Kauroa Ash Formation, with the Rangitawa Tephra, a grey-brown micaceous tephra bed, and associated distinct yellowish, coarse, sandy boundary layer, at the base. The formation is sourced from the Taupo Volcanic Zone/Coromandel Volcanic Zones, and is widespread throughout the North Island, in particular Waikato, Bay of Plenty, and Coromandel regions (Lowe *et al.,* 2011).

2.4 Tectonic deformation

Faulting

Active faults are closely related to earthquakes and other seismic hazards (Fossen, 2010). Faults are complex, compound features that can accommodate large amounts of strain within the upper Earth's crust (Fossen, 2010). Fossen (2010) gives a simple, traditional definition of a fault as "any surface or narrow zone with visible shear displacement along the zone". Fossen acknowledges this definition may vary depending on context. Faults tend to be complex zones, never expressing simple deformation types, especially when considered at a broad-scale. Rather, faults may include slip surfaces, subsidiary fractures, and deformation bands. What may appear to be a single fault at small scale may be multiple when assessed at field (large-scale) observation (Fossen, 2010). Faults may be connected to deformation mechanisms. This includes both brittle discontinuities and ductile shear zones in the plastic regime (Fossen, 2010).

Geometry of faults

Andersonian

Primary Stresses

The orientation of primary stresses controls the geometry of fault formation. Anderson first proposed three main types of fault movement; normal, reverse, and strike-slip, and theorised these were the result of three different primary stress orientations. As illustrated in **Figure 2.3**, the maximum primary stress is σ1, the intermediate is σ2, and the minor as σ3, switching between vertical and horizontal planes. When the vertical stress σv is oriented equal to σ1, the fault that develops is 'normal', whereas if σv is equal to σ2, a strike-slip fault forms, and when σv equals σ3, a reverse fault forms (Figure 2.3). Anderson's theories were tested and proven, and are now an accepted theory known as Andersonian Fault Mechanics (Fossen, 2010; Burbank and Anderson, 2011; Spinardi, 2017).

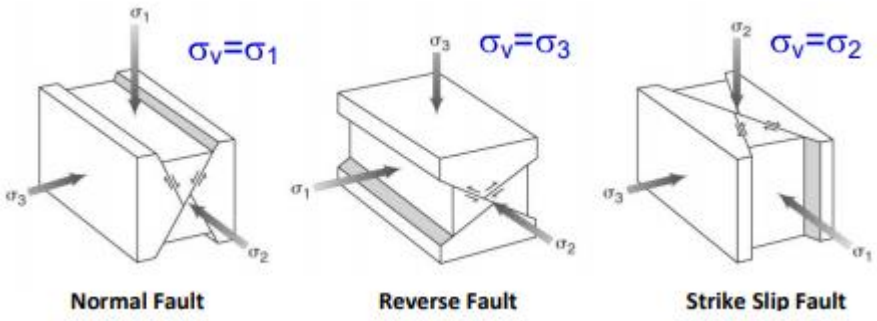

Figure 2.4: Andersonian Fault Mechanics. Illustrating the orientations of primary stresses relative to the fault that forms under those stresses.

Normal faults

Normal faults (aka. dip-slip) are an expression of extensional stress in the crust, forming in settings where the maximum compressive stress is vertical (gravity), and a deviatoric tensile stress exists in a horizontal orientation (Fossen, 2010; Burbank and Anderson, 2011; Campbell, 2017). The geometry of a normal fault is that the hanging wall is downthrown or lower than the footwall which may appear upthrown (Fossen, 2010; Burbank and Anderson, 2011; Campbell, 2017). The typical angle on these faults is between ~50 – 70º, at approximately 60 degrees (Burbank and Anderson, 2011; Campbell, 2017; Spinardi, 2017).

Listric faults

Listric faults appear like normal faults, except a curve develops – typically steep at the surface, shallowing off and flattening with increasing depth. Anti-listric faults are the reverse, steepening with depth (Fossen, 2010). Listric faults are an expression of geometric constraints, weaker geology, or changes in rock rheology with depth (Fossen, 2010; Campbell, 2017; Spinardi, 2017).

Reverse faults

Reverse faults are those that develop in compressional regimes. They appear the opposite to normal faults where the hanging wall is upthrown relative to the footwall. Offsets in reverse faults are often much lower angle than normal faults, at approximately 30 degrees (Fossen, 2010; Burbank and Anderson, 2011; Campbell, 2017; Spinardi, 2017). Faults less than 45 degrees are considered low angle thrust faults, and any above 60 degrees is considered steep faults (Fossen, 2010; Campbell, 2017).

Strike-Slip faults

Strike-slip faults are near vertical (~90 degrees) fractures with horizontal movement, 'slipping' past one another in opposing directions (Fossen, 2010; Campbell, 2017; Spinardi, 2017). The primary stresses σ1 and σ3 occur along the horizontal plane with σ2 equal to σv. These may be sinistral (left lateral), or dextral (right lateral). Strike-slip faults often serve as a link between collisional and extensional systems by transferring the displacement along the horizontal plane (Fossen, 2010; Spinardi, 2017).

Oblique-Slip faults

Oblique-slip faults are those with measurable components of both normal and strike-slip faulting. These faults are most commonly associated with trans-tensional or transgressional regimes whereby movement is caused by extension shortening or changing (Fossen, 2010; Campbell, 2017).

Fault zones

Fault zones are areas that have a series of subparallel fault or slip surfaces close together. The idea of a fault zone needs better defining to reduce common confusion as to the exact meaning of the term (Fossen, 2010). The term may now also be used to define the central-most part of the fault where most or all of the original structure has been lost or obliterated. It may also define the area about the core and central surrounding deformation/damage zone associated with the fault (Fossen, 2010). For this thesis, “fault zone” will be used to define a collection of potentially related faults within an area. The large faults within fault zones are often named ‘master faults’ and have smaller, minor faults associated with them. These smaller faults are given the names of antithetic or synthetic faults; antithetic referring to those which dip toward the master fault, whereas synthetic faults follow the same trend as the master fault and dip in the same direction (Fossen, 2010).

Syn-depositional faults

Faults that breach the surface to create relief that affects the depositional pattern of later sediments are known as syn-depositional faults. Sediments deposited over the fault structure will usually have a thicker deposit atop the downthrown block than the upthrown block. Variations in thickness over the two sides reflects fault activity variations over time (Fossen, 2010).

2.5 Soft Sediment Deformation

Soft sediment deformation structures (SSDS) develop when primary stratification is strained by a system of driving forces such as gravitational instability, overloading, wave-induced stress, reverse-density gradients, and cyclic stresses resulting from tectonic stress. The classification of SSDS is based on their morphological features such as load casts, drop and flame structures, clastic dykes and sills, disturbed laminates, convolute laminations, slumps, recumbent folds, and syn-sedimentary faults (Owen and Moretti, 2011; Moretti and Van Loon, 2014). Among the features, those induced by earthquakes can be directly related to the seismic stresses, thus are termed seismites. The evidence regarding seismites is often variable and inconclusive (Owen and Moretti, 2011).

As soil is subjected to both tensile and cyclic stresses during an earthquake, the grains will typically re-orient as a result of compaction and expulsion following cyclic pressures. If enough pressure is exerted, fluidisation processes occur leading to the formation of seismites (Owen and Moretti, 2011). Under sufficient stress, soils with

these properties will temporarily experience increased pore water pressure and consequential loss of shear strength. This is most commonly known as liquefaction or fluidisation. Conditions for liquefaction include recent sediments of Holocene-Pleistocene age, cohesionless soils of loosely-packed coarse silt to fine-to-medium sand in areas of shallow water table depths, restricted drainage/permeability, and low overburden pressure (Selby, 1993; Owen and Moretti, 2011). Upon stress the grains reorient and become supported by the pore water fluids when drainage is restricted, becoming suspended and moving with the fluid as it attempts to escape and dissipate the pore water pressure. With enough pressure, seismites form by fluid expulsion (Selby, 1993; Obermeier, 2009; Owen and Moretti, 2011).

The process can be broadly categorised into two categories, with the first, flow (static) liquefaction occurs in strain softening soils where the initial void ratio is higher than its steady or critical state, and the second type of liquefaction, cyclic loading, occurs when an oscillating force is applied and material is subject to both tension and compression. Typically, flow liquefaction is induced by either monotonic or cyclic loading where a material is subject to increased tension or compression.

According to Owen et al. (2011) three conditions must be present in order to for soft sediment deformation structures to form: 1) Driving force for primary sediment deformation, 2) Deformation mechanism, and 3) A trigger. These are also key to identifying soft sediment deformation structures, particularly for separating seismic vs aseismic causes. Triggers include non-seismic causes such as ground-water intrusion, ocean waves, an excessive loading, and tensile or cyclic seismic triggers (Owen and Moretti, 2011), It is difficult to identify the exact type of trigger (seismic/non-seismic) as many triggers produce very similar morphologies (Obermeier, 2009; Owen and Moretti, 2011).

When attempting to identify seismically-induced SSDS, a criterion may be used to separate them from other triggers. Criterion for indicating seismic triggers include: 1) large areal extent, 2) lateral continuity, 3) vertical repetition, 4) appropriate morphologies, and 5) proximity to faults. Each alone are not enough to classify a seismic trigger, rather, zonation of complexity and/or frequency with distance from fault together provide a suitable criterion. Features must be widespread with a regional distribution centred around an area of greater observed deformation (Obermeier, 1996; Owen and Moretti, 2011).

The topic must be approached with context, assessing all aspects and relative sedimentary successions. Context-based approaches are typically implemented to rule out non-seismic triggers before considering seismic influences (Owen and Moretti, 2011). The aforementioned criteria and context-based analyses together provide reliable assessments of the trigger mechanism. Steps in assessment of

triggers include: 1) Describe facies, 2) Describe sedimentary structures focussing on depositional and erosional features (to rule out non-seismic), 3) Reconstruct the prior stratigraphy pre-deformation to determine probable mechanisms.

Seismites (Paleo liquefaction features)

A common seismite feature is injection of sand through areas of weakness in the strata in the form of clastic dikes and sills (Owen and Moretti, 2011). Dikes are the most abundant, resulting from vertical intrusion of sediment-rich pore water, with sills often occurring alongside dikes in vertical outcrops. Dikes and sills often pinch out in response to semi-permeable areas which reduce flow. The soil strength and permeability controls this – wherever permeable and/ or weak materials exist, pore water may travel to reduce the imbalance. Ejection of pore water and suspended sediments to the surface often leads to the development of conical features termed sediment blows/boils and volcanoes (Obermeier, 2009). Seismites have been referred to as chaotic in literature resulting from the high diversity in features. Features may also include ball and pillow structures, flame structures, pseudo-nodules, dish and pillar features, and more (Owen and Moretti, 2011) with examples of soft sediment deformation structures illustrated in **Figures 2.4 and 2.5.**

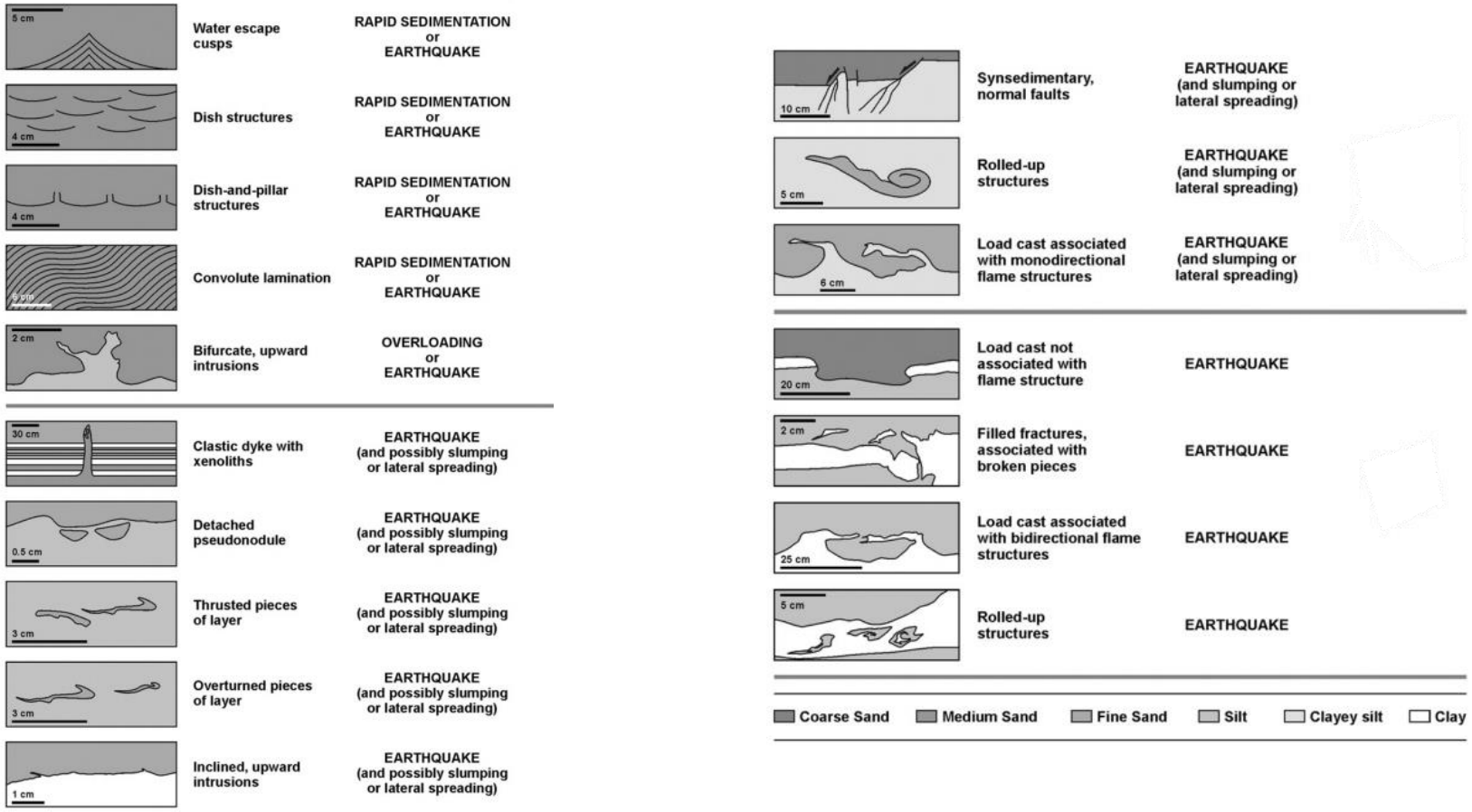

Figure 2.4: Typical soft sediment deformation morphologies typical of earthquake triggers. Image sourced from Suter et al. (2010).

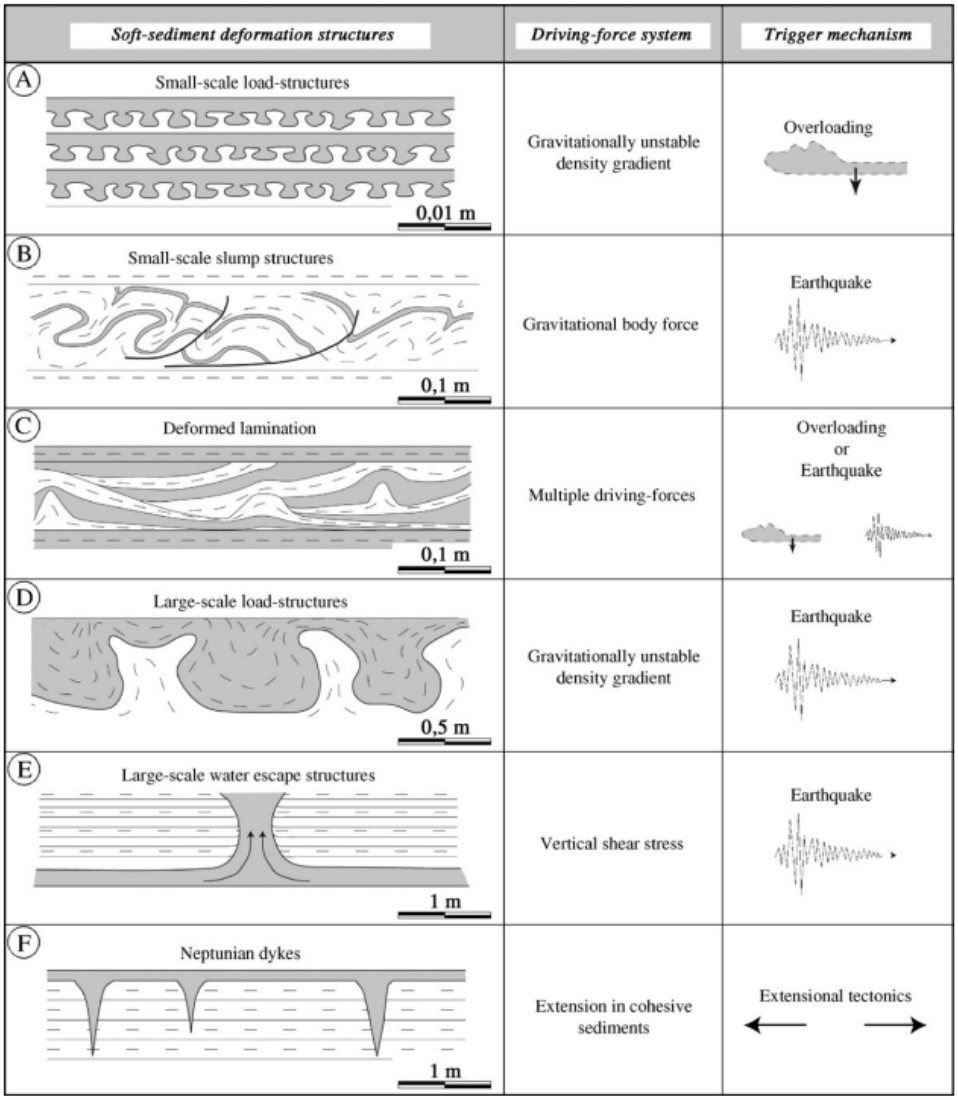

Figure 2.5: Sketches of soft-sediment deformation structures with their driving force and trigger mechanisms. Sourced from Moretti and Sabato (2007).

2.6 Current knowledge of Hamilton Basin deformation

Known Faults

Before 2015, there were no known faults within the Hamilton Basin other than old inferred faults within the underlying basement strata (Edbrooke, 2005). An outlier of basement strata and inconsistent river terraces at the surface near Mystery Creek between Hamilton and Cambridge lead to suspicions of intra-basin faulting in addition to the bounding faults (Kamp and Lowe, 1981). Since the original discovery, other faults with a throw of about one metre, trending N-NE offsetting Pleistocene strata have been observed (Kamp and Lowe, 1981). Deep faults parallel to depth contours were inferred in the seismic, gravity, and test wells (de Lange and Moon, 2017).

These faults appear to cut across the river at approximately right angle bends. These inferred faults include those at Horotiu, Templeview-Rototuna, Hamilton CBD, Ruakuhia-University, all of which run NE to SW with some curvature, as shown in **Figures 2.6 and 2.7** (Moon, de Lange, and Cummins, 2017).

Other tectonic deformation of the geology and geomorphology indicating faulting and seismic potential include paleoliquefaction structures, gully systems, and alignment of low rolling hills with outcrops of the Puketoka Formation in Flagstaff and at Osborne and Kay Roads. Other lakes within the basin exhibit seismite soft sediment deformation, with three disrupted tephras indicating three separate seismic events over the past ~12 thousand years. Two of these disruption events are believed to be caused by distal earthquakes, however one is limited to a small area, suggesting a local earthquake was likely.

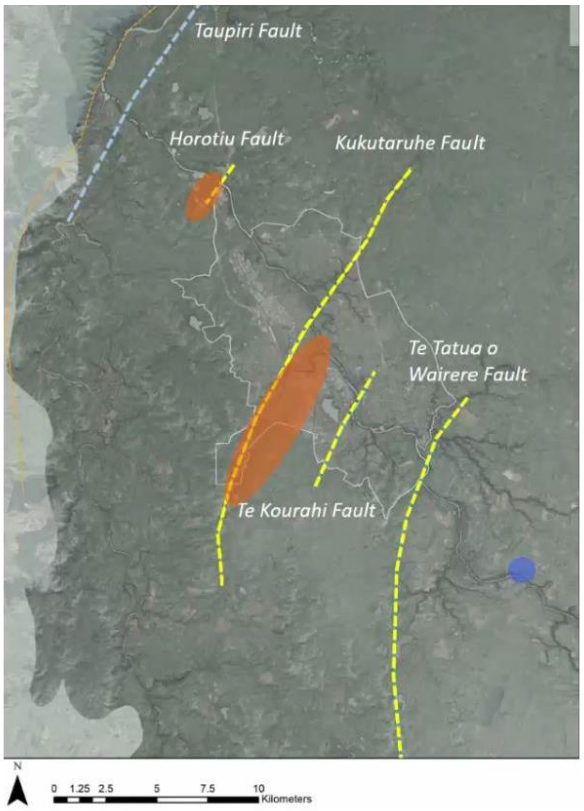

Figure 2.6: Summary of fault zones across the Hamilton Basin. Observed trending NE-SW with some curvature. Sourced from Moon et al. (2017).

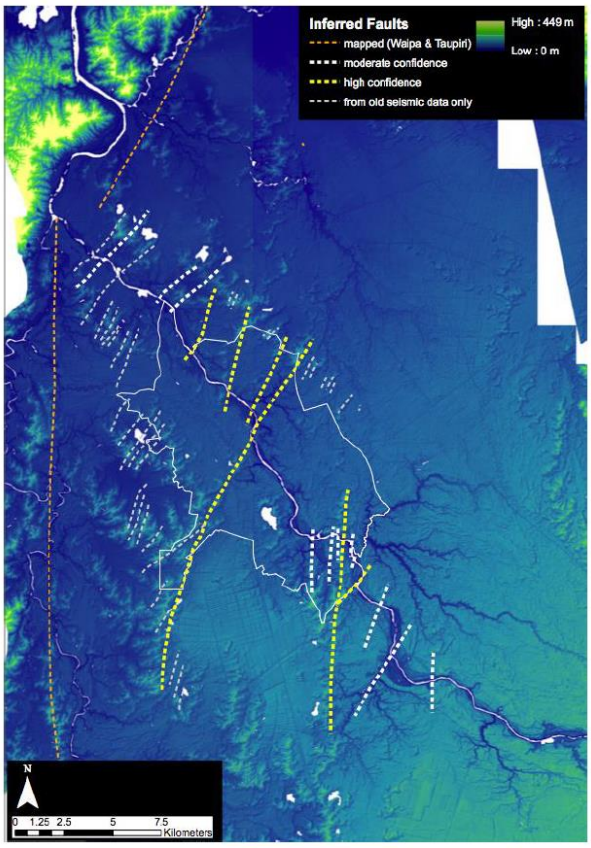

Figure 2.7: Mapped and inferred fault zones across the Hamilton Basin with varying confidence ranges. Orange indicates mapped faults, yellow indicates high confidence, and white suggests moderate confidence (Moon et al. 2017).

2.7 Summary

Literature regarding the Hamilton Basin was relatively old and contained significant gaps in knowledge regarding the effect of tectonic processes within the Hamilton Basin. The majority of literature regarding the Hamilton Basin suggested there was a general consensus that the Hamilton Basin has not been affected by tectonic deformation other than on the faults surrounding the basin. Since 2015 and the identification of the first fault in Rototuna-Flagstaff area, this initial hypothesis has been rejected and a new hypothesis of significant deformation and faulting within the basin supported with each new piece of information received. Kleyburg (2015), McKay (2017), Moon and de Lange (2017), Campbell (2017) and Spinardi (2017) provided valuable insight into the tectonic influences and expressions across the Hamilton Basin.

Chapter 3

Methodology

3.1 Introduction

This chapter outlines the field and laboratory methods undertaken to complete this research project. Testing followed referenced standards, with any deviations specifically noted and described in detail. After field methods and sampling were completed, laboratory testing was carried out to characterise the physical properties of the soils. This chapter is divided into field methods and field data processing, followed by laboratory methods.

3.2 Field Methods

Site Walkover

The study site is located at 59 Hillcrest Road, Hamilton (37°47'33.89"S, 175°18'59.02"E), an active residential subdivision development site managed by Phoenix Civil Ltd at the time of investigation. At the time, the site contained a cutting through a slope that was freshly exposed by the crew during their groundworks. The cutting contained a sequence of natural deposit materials covered by disturbed material brought in as fill from previous developments in the area.

The field investigations began with a general walkover of the site to familiarise myself with the geomorphology of the slope and to determine where soil profiles and other field methods should be carried out. During this process, at least three soil profiles 10-15 metres apart were determined necessary. Photographs of the face were taken before the material weathered and weathering and earthworks processes obscured the colours.

Field Sketches

During the initial walkover of the site, field sketches were produced to provide a better understanding of the geology and their stratigraphic positions. Field sketches were modified at varying times during the fieldwork as the geology was better understood or where the team on site uncovered anything.

Profile Descriptions

Following the site walkover and initial field sketches, six profile descriptions were undertaken along specified portions of the slope. A 30-metre tape measure was laid from the top of the slope to the base. Along the tape, boundaries between layers were identified. Each identified layer was described according to the Soil Description Handbook by Milne *et al.* (1994), and a template from the New Zealand Geotechnical Society (NZGS, 2005). These unit descriptions included the dominant and minor grain sizes, texture, colour, in situ moisture state, consistency (plasticity, stickiness, sensitivity (via shear vane), structure), strength, grading, bedding, shape of grains, additional materials/mineralogy, any grading and bedding, geological origin and unit name. (NZGS, 2005). Following some research these units were given names based on their geological units. During the profile description process, any anomalies were identified, recorded, and photographed. In total, three complete full soil profiles were described (Profiles 2, 3, and 4), whilst the other three profiles (Profiles 1, 5, 6) had portions obscured by fill/disturbed materials from outside of the field site. Profile 6 was later unveiled by the team on site during digging of a deep pit approximately 8 metres deep, 11 metres long, and 8 metres wide, and renamed Pit 1/Profile 6. Full unit descriptions are presented in **Appendix I.**

Shear Vanes

Along the soil profiles 2 – 4, shear vanes were carried out to identify in-situ field strength and material sensitivity in the cutting. Shear vanes were completed according to the New Zealand Geotechnical Society standard testing procedure (STP) (NZGS, 2005) with one exception; rather than turning the blade the standard 5 times, the blade was turned 10 times to calculate remoulded soil strength as per Cunningham (2012). Raw data from this process is attached in **Appendix II.** The processed data are included in the profile descriptions and resulting stratigraphic logs as unit sensitivity.

GPS

Leica Captivate GNSS Viva GS16 Antenna unit, together with a Leica CS20 controller RTKplus device was used to precisely determine the top and bottom of the soil profiles (2 – 6), and to map out the top and base contacts of key stratigraphic units exposed within the slope. Later the GPS unit was also used to

map the shape of the soil pit dug out beneath profile 6, and to mark the contact between the top bed of the *in situ* materials with the disturbed materials above, and the contacts within the lower sequence of beds. These co-ordinates were used to illustrate the placement of the soil profiles and key geological units on Google Earth.

Sampling

Sampling of key stratigraphic units was undertaken based on profile descriptions and observations.

Bulk

Bulk samples were collected for Atterberg limits and grain-size, XRD, XRF and SEM analyses. As the sampling was done under hot, dry conditions, samples were collected by removing the outer 10 cm of material and collecting a sample from this depth to ensure clay minerals had not been dehydrated following exposure

Cores

Eighteen stainless steel tubes 50 mm x 150 mm were collected obtain undisturbed samples for static triaxial testing, Atterberg limits, and grain size, XRD, XRF and SEM analyses. The failed triaxial cores were used for thin section and petrographic analyses. Samples were named HCRX (Hillcrest Cores Rangitawa) based on the order they were removed, i.e. HCR1, HCR2, HCR3.

To retrieve these samples, a flat bench was cut one metre into the slope along the bedding plane of the Rangitawa Tephra, and another along the bedding plane contact of the Rangitawa Tephra and the Kauroa Ash formation. The push tubes were carefully hammered in before being extracted gently and wrapped in plastic wrap for storage before use (figure). The material was incredibly dry, so to facilitate hammering and prevent cracking, water was poured onto the cut shelf, and lanolin sprayed onto the exterior of the steel tubes as a lubricant.

Eight 50 mm – 40 mm size steel tubes were used to collect bulk density samples of the overburden above the Rangitawa Tephra. The positions for these overburden samples were collected based on stratigraphic observations of variations in colour and texture. The samples were named HBX (Hillcrest Bulk) based on the order they were removed, i.e. HB1, HC2, HB3. These were collected by scraping crusted material off the face of the cutting, then hammering the tubes into the face before carefully removing and wrapping in plastic wrap to maintain natural moisture content.

Structural Data

Attempts were made to identify any bedding planes, fault traces etc. Any bedding planes, faults, or other anomalies that could be identified were measured with dip and dip direction and a relative GPS co-ordinate point for later reference recorded. These data were uploaded into RocScience Dips Software to produce a stereonet of the accumulated dip/dip direction data.

3.3 Field Data Processing

The open source software, Inkscape, was used to annotate and illustrate photographs and sketches taken in the field. Key figures produced included cross-sections detailing stratigraphy and any structural anomalies in the field, and stratigraphic logs of the soil profiles 2-4 and 6. The software was used additionally to indicate where structural data and samples were retrieved.

3.4 Laboratory Methods

Grain-size

Using Standard Operating Procedure at the University of Waikato, the Malvern Master-sizer 3000 was used for grain size analysis on samples from the key layer (Rangitawa Tephra). This included some of the core samples and proportion of each of the three pastes used for Atterberg limits analysis. About one teaspoon of each sample was mixed with a few drops of Calgon and distilled water until a slurry was produced. This was done to break any bonds between the clay particles and prevent clay aggregates from being sized as silts/sands. Three runs of each of HCR1, HCR3, HCR5 top and base, HCR6 top and base, HCR7, HCR18, and Atterberg pastes 1-3. The three runs were cumulated to give an average for that sample (and potentially check for inaccuracies?). The raw data from this is presented in **Appendix III(a).**

Thin Section preparation

The three failed triaxial core samples (HCR1, HCR3, HCR7), and one untested (HCR18) were dry trimmed into blocks to fit glass petrographic microscope slides. Each face of the sample was impregnated with EpoFix resin and hardener at a ratio of 2 to 1 and left overnight on a 60^{o}C hotplate to set. The selected face on each was ground smooth using a silicon carbide powder until the surface had an even matte appearance and placed back on a 60^{o}C hotplate to dry thoroughly. The

prepared surface was mounted onto the frosted side of the glass petrographic microscope slide using Hillquist thin section resin at a ratio of 2.3:1 and left overnight to set. The mounted blocks were dry cut to a thickness of ~1 mm, then further ground to a satisfactory thickness for petrographic analyses using Struers Discoplan-TS in the Faculty of Science at Waikato.

The prepared thin sections were examined using a petrographic microscope in both plane and cross-polarised light to identify and describe the different mineral components.

X-Ray Powder Diffraction (XRD)

X-ray powder diffraction (XRD) was used to indicate mineralogy of the Rangitawa Tephra samples to support thin section petrography. The XRD analysis was carried out on whole material samples, which were dried at 105ºC for 48 hours then crushed into a fine powder using an agate mortar and pestle. Approximately 10 grams of each sample was then put through the Panalytical Empyrean Series 2 XRD in the Faculty of Science and Engineering, University of Waikato. The prepared samples were run for 5-80°2Θ, at 50 seconds per step. Highscore Plus was used to identify the potential mineralogy.

Clay samples were prepared following the methods of Cunningham (2012, after Whitton and Churchman (1987) and Lowe and Nelson (1983)). Clay fractions were separated from the rest of the Rangitawa Tephra. The excess liquid was pipetted off, and more distilled water added and the same repeated the next day. The clay samples left in the beakers were pipetted onto four tiles each, and left in a moist desiccator to dry without dehydrating. Each tile was applied a treatment. Tile one was left untreated, tile two had ethylene glycol applied, tile three was heated at 110° for an hour, and tile three heated at 550° for an hour. Samples run from 2-45 °2θ at 120 seconds per step and the resulting diffraction patterns for the various treatments analysed to identify clay mineralogy.

X-Ray Fluorescence Spectrometry (XRF)

Major element geochemical analyses were conducted at the University of Waikato using the Bruker S8 Tiger XRF instrument. The raw results for these geochemical analyses are presented in **Appendix V(a)**. For major element analysis, glass fusion beads were formed by combining approximately 0.8 g of powdered sample

with 8 g flux (12:22 Lithium Tetraborate 35.3% / Lithium Metaborate 64.7%) and ~ 1 g of NH_4 and heating in a furnace (Claisse LeNeo Fluxer by Malvern Panalytical) at 1050°C for 20 minutes. The sample was then poured onto a mould and fan cooled before running through the XRF instrument. Loss on ignition was also determined. ~2 g of sample was left in the furnace at 1100°C for an hour. The LOI was calculated from the percent mass lost during this process.

Scanning Electron Microscope (SEM)

SEM was undertaken to identify the clay mineralogy within the Rangitawa Tephra. For this, a (very small) amount of air-dried ample was used to observe the clays in a somewhat natural state, and small sample of oven-dried material to observe what the sample would look like in a dehydrated state. The geological formation was well described to contain halloysite; therefore, the material was treated as containing at least some of this clay mineralogy and kept moist wherever possible.

Atterberg Limits

Wet-preparation method of the paste was used for the Atterberg limits testing. The sand-sized grains were left in the material to give a better representation of the natural state of the material. Ten tests were carried out. The first five were produced with the first Atterberg paste, and this was carried out with 5 moisture contents, 5 penetrations per moisture content. The second paste prepared was used from samples 6 to 8, and the third for samples 9 and 10. The second and third pastes (samples 6 to 10) were subject to 8 moisture contents, 10 penetrations each. Results from these tests are presented in **Appendices VI.**

Bulk density

The eight 50 mm by 40 mm cores taken from the cutting were used to calculate the bulk density of the beds and subsequently the overburden stress on the Rangitawa Tephra. This was vital to triaxial testing of the Rangitawa Core samples. The samples were removed from the metal sheaths and placed into metal tins. The samples were weighed, placed into an oven at 105^{o}C for 48 hours, then weighed again to determine the moisture contents. The bulk density of the samples (when dry) were also calculated. Calculations presented in **Appendix VII(a).**

Static Triaxial

Cores 50 mm by 150 mm taken in the field were used for triaxial testing. HCR1, HCR3, and HCR7 were used for static triaxial testing (HCR2, 4, 5, and 6 all broke as they were being extracted).

Triaxial shear tested was carried out using methodologies according to British Standard 1377 (1990). The samples were unwrapped from their plastic wrap and extruded within the laboratory. The samples were moved using a split mould, placed on a glass plate and trimmed gently by shaving pieces of the core off until the sample was trimmed flush with the split mould. The sample was weighed, and the dimensions measured with a calliper and written down. The sample was then transferred and placed into the triaxial apparatus upon a porous plate and filter paper. A membrane was placed into a sample holder and vacuum sealed to the edges before being placed over the sample and the vacuum released. Black rubber O-rings were placed on the top and bottom of the sample, and the membrane rolled over to seal the sample from the rest of the apparatus. The cell was gently lowered onto the sample, ensuring the white tube within the apparatus was not crushed. The triaxial cell was then sealed using the bolts, tightening two bolts opposite at a time until watertight. The sample dimensions and weight, along with the testing conditions were input into the triaxial software. The cell was flooded, ensuring no air bubbles were left within the cell, then testing started. Testing began with a pore water pressure ramp until saturation. The sample was then consolidated according to the applied conditions. The loading and shear testing then began. Following testing, the sample was removed from the apparatus, weighed, and photographed before being stored in an air-tight container to maintain moisture until the samples were used for other methodologies. The post-testing samples were sketched, and any failure planes identified. The data collected during the stages of testing were collected and transferred into excel spreadsheets for triaxial shear test calculations and analyses.

HCR1 was tested with a cell pressure of 740 kPa, back pressure of 640 kPa, and an effective stress therefore 100 kPa. HCR3 cell pressure was 740 kPa, back pressure 590 kPa, and effective stress 150 kPa. The cell pressure for HCR7 was 600, back pressure 550 kPa, therefore, an effective stress of 100 kPa.
Data and results from these analyses are presented in **Appendices VII (b-i).**

Chapter 4

Results – Field

4.1 Introduction

This chapter details the observations of the field area, alongside cutting face and unit descriptions, shear vane (material sensitivity) results, structural data, and identification and description of deformation structures observed during field investigations.

In soft, loose, or unconsolidated materials such as soils, brittle fracture is often masked by ductile deformation (Burbank and Anderson, 2011). Describing and quantifying the features exposed in the cutting will hypothetically prove this is the case in this inferred fault.

4.2 Field area

Figure 4.1 is a satellite image from Google Earth providing an aerial view of the field area and expressing the scale of earthworks for this project. **Figure 4.2** provides a drone photo facing northeast toward the cutting exposing a birds-eye view of the cutting and stratigraphy of the hill beneath Hillcrest Road and the university.

The cutting at 59 Hillcrest Road (37°47’33.17’S 175°18’57.20’E) dissects the hill perpendicular to the strike of the ridgeline running along Hillcrest Road. The cutting has an aspect toward the south-west and is approximately 10 metres tall by 100 metres long at an angle of 18 – 20°.

The cutting exposed the full sequence of expected geological units as published by Kamp and Lowe (1981), Kear and Schofield (1986), Lowe et al. (2001) and McCraw (2011).

Figure 4.1 Aerial view of the cutting and expresses the extent of earthworks at 59 Hillcrest Road, Hamilton. White lines indicate soil profiles 2 to 6.

Figure 4.2 Still from drone footage of the site at 59 Hillcrest Road, Hamilton. Viewing toward east-northeast.

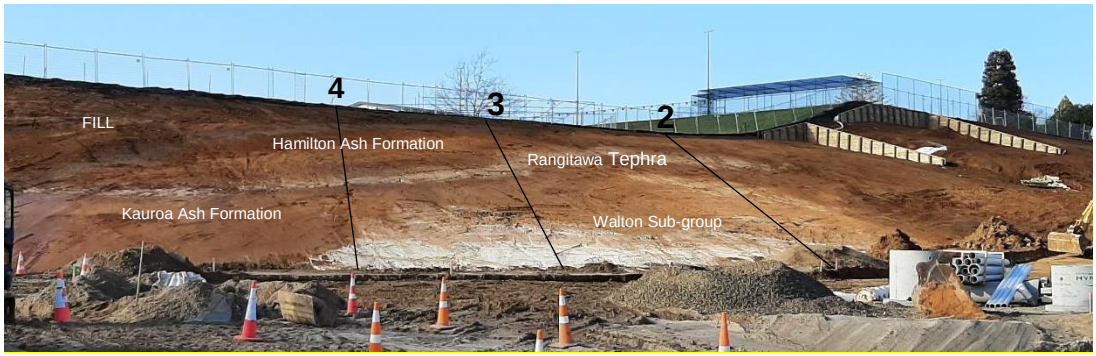

Figure 4.3 Photograph of the cutting from ground level, facing toward the northeast. Illustrates the stratigraphic relationships through the ridgeline under Hillcrest Road, Hamilton. White lines indicate profiles 2 to 4.

4.3 Face Descriptions

Figure 4.3 provides a view toward east-northeast from the base of the slope, looking up - expressing a splendid view of the site and providing a cross-section of the ridge beneath Hillcrest Road. The cutting exposed a wavy white layer with interbedded reds and yellows at the base, overlain by a light brown unit with the same reddish coloured interbedded layers. Above this is a bright brown layer which grades into a dark reddish brown above. A sharp contact occurs before a distinct light grey layer, which grades into a sequence of yellowy-brown, brown, bright brown, and dark brown layers. Overtopping this sequence are layers of very-dark brown disturbed 'fill' materials.

Using the law of stratigraphic succession along with Kear and Schofield (1986), Lowe *et al.* (2001) and McCraw (2011) the units in the cutting were assigned geologic units. The white layer at the base was identified as the fluvially reworked ignimbrite deposits of the Walton Subgroup (c. 3.0 Ma) (Kamp and Lowe, 1981). The Kauroa Ash Formation (c. 2.3-0.78 Ma) (Briggs *et al.,* 1989; Horrocks, 2000; Lowe *et al.,* 2001) occurs above, and interfingers the units below as the bright brown and dark-reddish brown units. The light grey layer was identified as the Rangitawa Tephra (c. 0.34 Ma), the base layer of the sequence of the warm browns of the Hamilton Ash Formation (c. 340-68 ka) (Pillans *et al.,* 1996; Lowe *et al.,* 2001; McCraw, 2011).

Figure 4.4 provides the key for the following **Figures 4.5 and 4.6. Figures 4.5 and 4.6** show the stratigraphic sequence at the Hillcrest cutting with digitized unit boundaries according to the key.

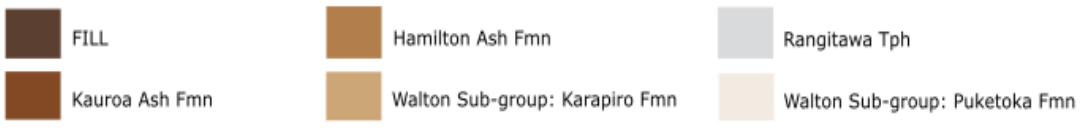

Figure 4.4 Key for figures in this section

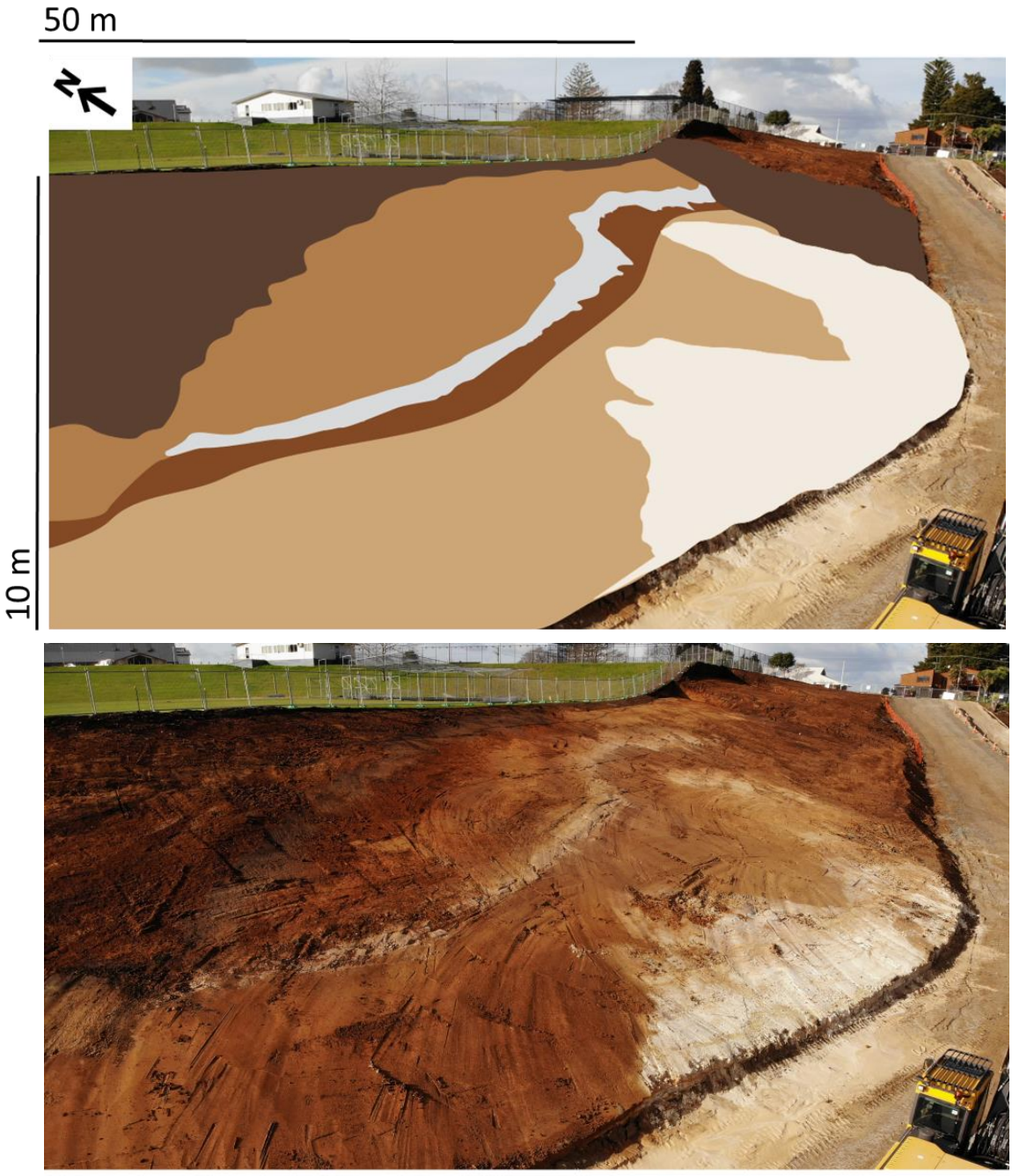

Figure 4.5 Inkscape annotation of cutting presenting stratigraphic relationships at 59 Hillcrest Road, Hamilton. Facing east-northeast.

Figure 4.6 Inkscape annotation of cutting at 59 Hillcrest Road, Hamilton showing stratigraphic relationships. Facing northeast.

4.4 Unit Descriptions

The study area is comprised of a mixture of silty clays, clayey silts, silty sands, and some gravelly portions. The majority was of volcanic origin, deposited and reworked by tephra-fall, alluvial, or fluvial means. The section below presents soil profile descriptions and stratigraphic columns for each profile (2-4) along with material sensitivity measurements. **Tables 4.1 to 4.3** provide shortened descriptions of soil profiles 2, 3, and 4 at the site. Full unit descriptions are presented in **Appendix I.** Profile positions relative to the site are shown in **Figures 4.1 and 4.2**. **Figures 4.7 (a-d)** provide stratigraphic logs of the soil profiles (2, 3, 4, and 6) expressing the stratigraphic relationships of the site. Geological names and units used in this thesis were provided by comparisons to published literature.

Table 4.1 Soil Profile Description of cutting at 59 Hillcrest Road. Profile 2.

Geological name	**Depth (cm)**	**Layer description**
Fill	0-15	FILL
Hamilton Ash Formation (H7)	15-26	Clayey SILT; dark-brown (10YR 3/4); apedal earthy; weak, friable; diffuse, irregular lower boundary.
Hamilton Ash Formation (H6)	26-32	Silty CLAY; yellowish brown (10YR 5/6), few fine dark brown mottles (10YR 3/4); low pedality, few fine polyhedral peds; slightly firm, brittle; light grey silty infilled cracks ~ 1cm aperture; diffuse, irregular boundary.
Hamilton Ash Formation (H5)	32-89	Silty CLAY; bright brown (7.5YR 5/6); moderate pedality, few fine nutty peds; firm, brittle; diffuse, irregular lower boundary.
Hamilton Ash Formation (H4)	89-117	Silty CLAY; brown (10YR 4/6); moderate pedality, common fine to very-fine nutty peds; slightly firm, brittle; diffuse, irregular lower boundary.
Hamilton Ash Formation (H2/3)	117-226	Silty CLAY; variable colours/profuse mottles. Dull yellow-orange (10YR 7/3), dull orange (7.5YR 7/3), yellow-orange (7.5 YR 7/8), orange (7/5YR 4/6); apedal earthy; slightly firm, brittle; brown (7.5YR 7/8) in cracks ~1 mm aperture, light grey (7.5YR 8/1) infilling ~ 1 cm diameter at 190 cm; diffuse, irregular lower boundary.
Rangitawa Tephra (H1)	226-263	Clayey SILT, fine sand (mica) at top; light brownish grey (7.5YR 7/2); brownish black (7.5YR 3/2) and bright brown-orange (7.5YR 5/8 – 6/8) in cracks, light grey (10YR 8/1) along veins; apedal earthy; platy breakage; hard, brittle; sharp, irregular lower boundary.
Rangitawa Tephra (base layer)	263-266	Silty SAND (fine to medium), some clay; light orangey-yellow (10YR 8/3); apedal, single grained; abrupt, irregular lower boundary.
Kauroa Ash Formation	266-294	Silty CLAY, some fine sand; dark reddish brown (5YR 3/6); apedal earthy, blocky breakage; slightly firm, semi-deformable; gradational lower boundary.
Kauroa Ash Formation	294-380	Clayey SILT; bright brown (7.5YR 5/8); apedal earthy; slightly firm, semi-deformable; diffuse, irregular lower boundary.
Walton Subgroup Karapiro Formation	380-834	Gravelly CLAY/SILTS; variable colours; white, pale-yellow (5YR 8/4), yellow (5YR 8/6), light yellow-orange (7.5YR 8/3), orange (7.5YR 7/6), orange (7.5YR 6/8 and 10YR 7/8); apedal; slightly firm-to-firm, deformable; poorly sorted, poorly graded; abrupt, wavy boundary.
Walton Subgroup Puketoka Formation	834-914	Silty CLAY; white with interbedded layers (of pinks/reds etc); wet; apedal earthy; weak, deformable; poorly sorted, poorly graded; boundary not observed (End of profile)

Table 4.2 Soil Profile Description of cutting at 59 Hillcrest Road. Profile 3.

Geological name	Depth (cm)	Layer description
Fill	0-83	FILL
Hamilton Ash Formation (H7)	83-119	Clayey SILT; dark-brown (10YR 3/4); moderate pedality, few fine polyhedral peds; weak, friable; irregular, diffuse lower boundary.
Hamilton Ash Formation (H6)	119-161	Silty CLAY; dull yellowish-brown (10YR 5/4); few fine dark-brown mottles (10YR 3/4); strong pedality, abundant fine polyhedral peds; weak, friable; irregular diffuse lower boundary.
Hamilton Ash Formation (H5)	161-235	Silty CLAY; bright brown (7.5YR 5/8); red streaking; weak pedality, common fine to very-fine nutty peds; slightly firm, brittle; irregular, diffuse lower boundary.
Hamilton Ash Formation (H4)	235-256	Clayey SILT; brown (10YR 4/6); brown (7.5YR 4/6) in cracks ~1mm aperture, light grey (7.5YR 8/1) in veins ~1 cm diameter; moderate pedality, few fine polyhedral peds; slightly firm, brittle; infilling at 230 cm, some fine mica and micro-fine sub-rounded quartz present; diffuse, irregular lower boundary.
Hamilton Ash Formation (H3)	256-349	Clayey SILT, some fine sand (mica); yellowish brown (10YR 5/8); some orange staining; moderate pedality; few fine nutty peds; slightly firm, friable; increased concentration of mica; diffuse, irregular lower boundary.
Hamilton Ash Formation (H2)	349-448	Silty CLAY; yellowish brown (10YR 5/6); weathered colours; apedal earthy, slightly firm, brittle; diffuse, irregular boundary.
Hamilton Ash Formation (H1)	448-490	Sandy SILT, some clay; light brownish grey (7.5YR 7/3); Brownish black (7.5 3/2) and bright brown-orange (7.5YR 5/8 and 6/8) in cracks, light grey (10YR 8/1) in veins; apedal earthy, platy breakage; hard, brittle; black inclusions (?) increasing concentration at 1520cm (length); diffuse, irregular lower boundary.
Rangitawa Tephra (H1)	490-498	Sandy SILT; light grey (7.5YR 8/1); apedal earthy; hard, brittle; common fine mica and quartz (top- low mica, then high mica, then low mica and more clay, manganese at base); sharp, irregular lower boundary.
Rangitawa Tephra (base layer)	498-501	Silty (medium) SAND; light yellow-orange (10YR 8/3) and yellowish orange (10YR 8/8); apedal, single grained; fine mica, quartz, and dark inclusions, some fine, sub-rounded pumice; abrupt, irregular boundary.
Kauroa Ash Formation	501-566	Silty CLAY; dark reddish brown (5YR 3/6); light grey (10YR 8/1) silty infill along discontinuities at top; apedal earthy, blocky breakage; semi-deformable, firm manganese nodules; irregular, gradational lower boundary.
Kauroa Ash Formation	556-630	Clayey SILT; bright brown (7.5YR 5/8); apedal earthy; semi-deformable, firm; diffuse, irregular lower boundary.
Walton Subgroup Karapiro Formation	630-763	Silty (fine to coarse) SAND, some clay and fine gravel; variable colours; white, pale-yellow (5YR 8/4), yellow (5YR 8/6), light yellow-orange (7.5YR 8/3), orange (7.5YR 7/6), orange (7.5YR 6/8 and 10YR 7/8); apedal earthy; slightly firm, brittle; poorly sorted, poorly graded; sharp, wavy lower boundary.
Walton Subgroup Puketoka Formation	763-949	Silty CLAY; white with interbedded layers; apedal earthy, platy breakage; weak, semi-deformable at top, firm, deformable at base (of profile); interbedded, poorly sorted, poorly graded; lower boundary not observed. (End of profile).

Table 4.3 Soil Profile Description of cutting at 59 Hillcrest Road. Profile 4.

Geological name	Depth (cm)	Layer description
Fill	0-263	FILL
Hamilton Ash Formation (H7)	263-283	Clayey SILT; dark-brown (10YR 3/4); common very-fine red (10R 4/8) mottles; apedal, earthy; slightly firm, friable; irregular, diffuse lower boundary.
Hamilton Ash Formation (H6)	283-318	Silty CLAY; dull-yellowish brown (10YR 5/3); some fine dark-brown mottles (10YR 3/3) and microfine red-orange veins; strong pedality, abundant fine polyhedral peds; slightly firm, friable; slightly sticky; slightly plastic; no roots; irregular, diffuse lower boundary.
Hamilton Ash Formation (H5)	318-386	Silty CLAY; bright brown (7.5YR 5/8); abundant fine red mottles; moist; weak pedality, common fine to very-fine nutty peds; slightly firm, friable; irregular, diffuse lower boundary.
Hamilton Ash Formation (H3)	386-467	Clayey SILT; yellowish brown (10YR 5/8); common fine red mottles; weak pedality, few fine nutty peds; firm, brittle; diffuse, irregular lower boundary.
Hamilton Ash Formation (H2)	467-553	Silty CLAY; yellowish brown (10YR 5/6); weathered colours; weak pedality, some fine nutty peds, firm, brittle; diffuse, irregular boundary.
Rangitawa Tephra (H1)	553-596	Fine sandy SILT; light brownish-grey (7.5YR 7/3); very dark brown and reds in cracks, light grey silty veins; apedal earthy; hard, brittle; common fine mica and quartz (top- low mica, then high mica, then low mica and more clay, manganese at base); distinct, irregular lower boundary.
Rangitawa Tephra (base layer)	596-599	Silty (fine to medium) SAND; light yellow-orange (10YR 8/2); apedal, single grained; fine mica, quartz, and dark inclusions (manganese), some fine, sub-rounded pumice; abrupt, irregular boundary.
Kauroa Ash Formation	599-667	Silty CLAY; dark reddish brown (5YR 3/6); light grey (7.5YR 8/2) silty infill along discontinuities at top; blocky breakage; semi-deformable, firm; irregular, gradational lower boundary.
Kauroa Ash Formation	667-729	Clayey SILT; bright brown (7.5YR 5/8); apedal earthy; semi-deformable, slightly firm; very fine black inclusions; diffuse, irregular lower boundary.
Walton Sub-Group Karapiro Formation	729-791	Silty (fine to coarse) SAND, some clay and fine gravel; variable colours; white, pale-yellow (5YR 8/4), yellow (5YR 8/6), light yellow-orange (7.5YR 8/3), orange (7.5YR 7/6), orange (7.5YR 6/8 and 10YR 7/8); apedal earthy; flaky breakage; slightly firm, brittle; poorly sorted, poorly graded; sharp, wavy lower boundary.
Walton Sub-group Puketoka Formation	791-927	Silty CLAY; white with interbedded layers; apedal earthy; flaky breakage along beds; weak, deformable at top, semi-firm, semi-deformable at base (of profile); interbedded, poorly sorted, poorly graded; lower boundary not observed (End of profile).

4.5 Stratigraphic Logs

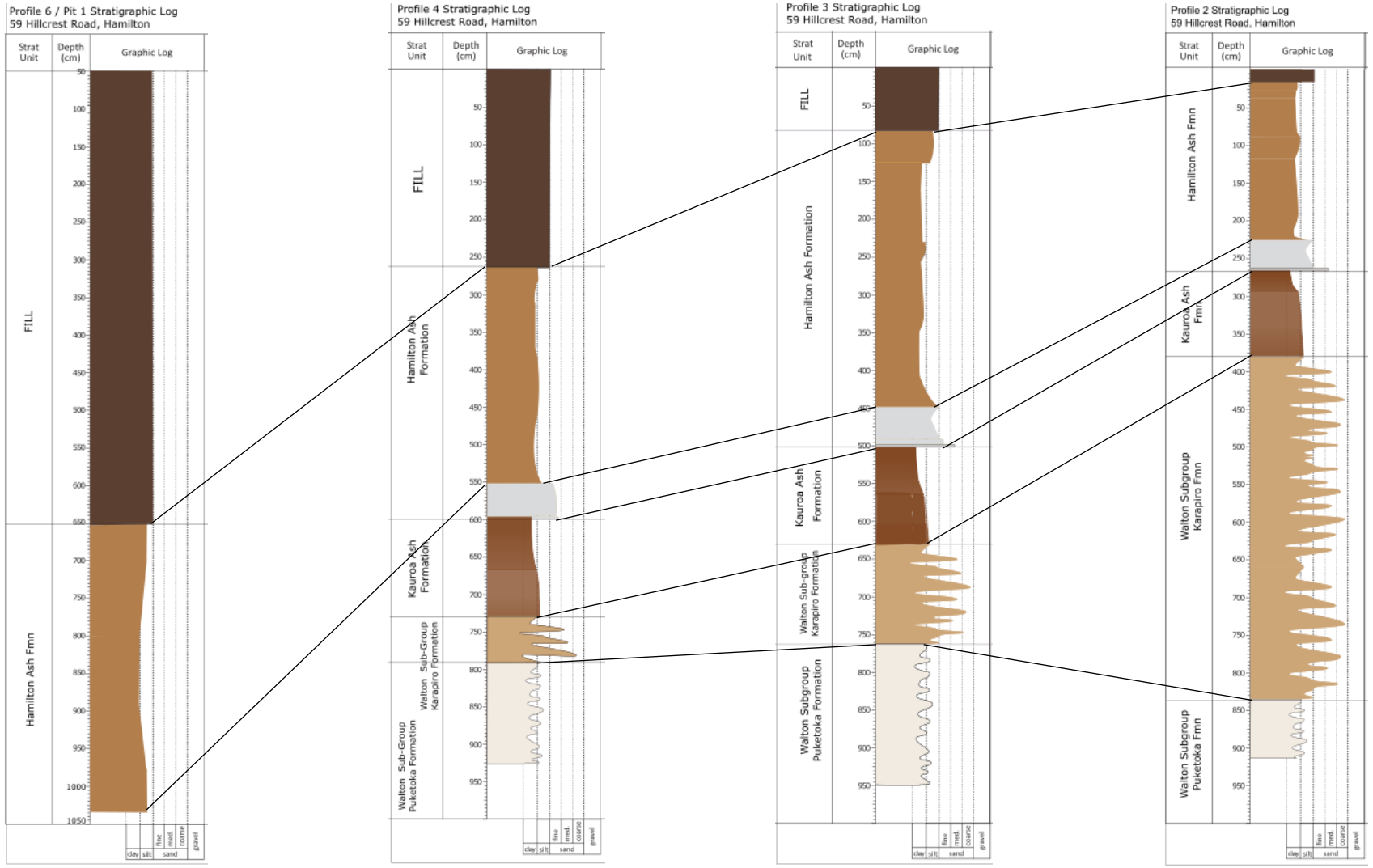

Figure 4.7 (a-d): Hillcrest Road Stratigraphic Profiles. Profiles 2, 3, 4, and 6 (Pit 1).

4.6 Material Sensitivity

Using field shear vanes, the sensitivity of geological units in the field for each soil profile (Profile 2, 3, 4) were calculated and are summarised below in **Tables 4.4 to 4.6.** Raw shear vane measurements and calculations appear in **Appendix II.**
Using NZGS (2005), the units are be classified by the ratio of peak, undrained shear strength to remoulded, undrained shear strength to define the loss of strength upon remoulding. Ratios of 1-2 indicate insensitive or normal materials, 2-4 moderately sensitive, 4-8 sensitive, 8-16 extra-sensitive and over 16 'quick'.

Table 4.4 Unit Sensitivity for Profile 2 at Hillcrest Road cutting (4/10/2019).

Depth (cm)	Geological Unit	Sensitivity
0-15	FILL	Not tested
15-26	Hamilton Ash Formation H7	3: moderately sensitive
26-32	Hamilton Ash Formation H6	6: sensitive
32-89	Hamilton Ash Formation H5	4: moderately sensitive to sensitive
89-117	Hamilton Ash Formation H4	7: sensitive
117-226	Hamilton Ash Formation H2/3	4: moderately sensitive to sensitive
226-263	Hamilton Ash Formation H1	3: moderately sensitive
263-266	Hamilton Ash Formation H1 (base)	Could not penetrate (CNP)
266-294	Kauroa Ash Formation	2: insensitive to moderately sensitive
294-380	Kauroa Ash Formation	5: sensitive
380-834	Walton Subgroup Karapiro Formation	10 to 4: moderately sensitive to very sensitive
834-914	Walton Subgroup Puketoka Formation	4: moderately sensitive to sensitive

Table 4.5 Unit Sensitivity for Profile 3 at Hillcrest Road cutting (22/10/2019).

Depth (cm)	Geological Unit	Sensitivity
0-83	FILL	FILL
83-119	Hamilton Ash Formation H7	5: sensitive
119-161	Hamilton Ash Formation H6	9: very sensitive
161-235	Hamilton Ash Formation H5	7: sensitive
235-256	Hamilton Ash Formation H4	2: insensitive to moderately sensitive
256-349	Hamilton Ash Formation H3	4: moderately sensitive
349-448	Hamilton Ash Formation H2	2: insensitive to moderately sensitive
448-490	Hamilton Ash Formation H1	2: insensitive to moderately sensitive
490-498	Hamilton Ash Formation H1	4: moderately sensitive to sensitive
498-501	Hamilton Ash Formation H1 (base)	CNP
501-566	Kauroa Ash Formation	2: insensitive to moderately sensitive
556-630	Kauroa Ash Formation	3: moderately sensitive
630-763	Walton Subgroup Karapiro Formation	6: sensitive
763-949	Walton Subgroup Puketoka Formation	5 to 13: sensitive to very sensitive

Table 4.6 Unit Sensitivity for Profile 4 at Hillcrest Road cutting (30/10/2019).

Depth (cm)	Geological Unit	Sensitivity
0-263	FILL	FILL
263-283	Hamilton Ash Formation H7	5: sensitive
283-318	Hamilton Ash Formation H6	9: very sensitive
318-386	Hamilton Ash Formation H5	7: sensitive
386-467	Hamilton Ash Formation H3	3: moderately sensitive
467-553	Hamilton Ash Formation H2	2: insensitive to moderately sensitive
553-596	Hamilton Ash Formation H1	3: moderately sensitive
596-599	Hamilton Ash Formation H1 (base)	CNP
599-667	Kauroa Ash Formation	4: moderately sensitive to sensitive
667-729	Kauroa Ash Formation	2: insensitive to moderately sensitive
729-791	Walton Subgroup Karapiro Formation	3 to 6: moderately sensitive to sensitive
791-927	Walton Subgroup Puketoka Formation	4 to 20: sensitive to quick

4.7 Structural Information

As the site investigation was non-invasive, it was complicated to assign the units a dip/dip direction and other structural information. To calculate the dip-dip direction for the Rangitawa Tephra unit without damaging the cutting face, small outcrops of the base unit of the Rangitawa Tephra contact with the Kauroa Ash Formation were used to gather structural data. The data collected and calculated mean and standard deviation are presented below in **Table 4.7.**

Table 4.7 Dip/Dip direction measurements for the lower Rangitawa Tephra – Upper Kauroa Ash boundary at Hillcrest Road. Standard deviation presented as error calculation. Values presented as whole numbers.

Measurement number	Dip (°)	Dip direction (°T)
1	6	213
2	4	228
3	5	220
4	11	193
5	20	152
6	17	168
7	4	194
8	7	149
9	3	261
10	7	209
11	14	168
Continued…		
12	9	266
13	27	169
14	15	161
15	26	245
16	10	245
17	6	217
18	18	223
19	9	157
25	5	231
Mean	**11.15 ± 7.24**	**203.45 ± 37.33**

The mean dip/dip direction is 11.15 / 203.45°, with a standard deviation of ± 7.24° / 37.33°. This suggests the Rangitawa Tephra is dipping at an average angle of 11° toward compass direction SSW (203°).

The stereonet below (**Figure 4.8**) provides a visual representation of the data in table 4.7. The stereonet calculated the global mean dip/dip direction on the Rangitawa Tephra as 5°/197° thereby suggesting the unit is dipping at an angle of 5° toward the south-southwest. This lies within the standard deviation calculated in **Table 4.7** (11 ± 7.24° and 203 ± 37.33° respectively).

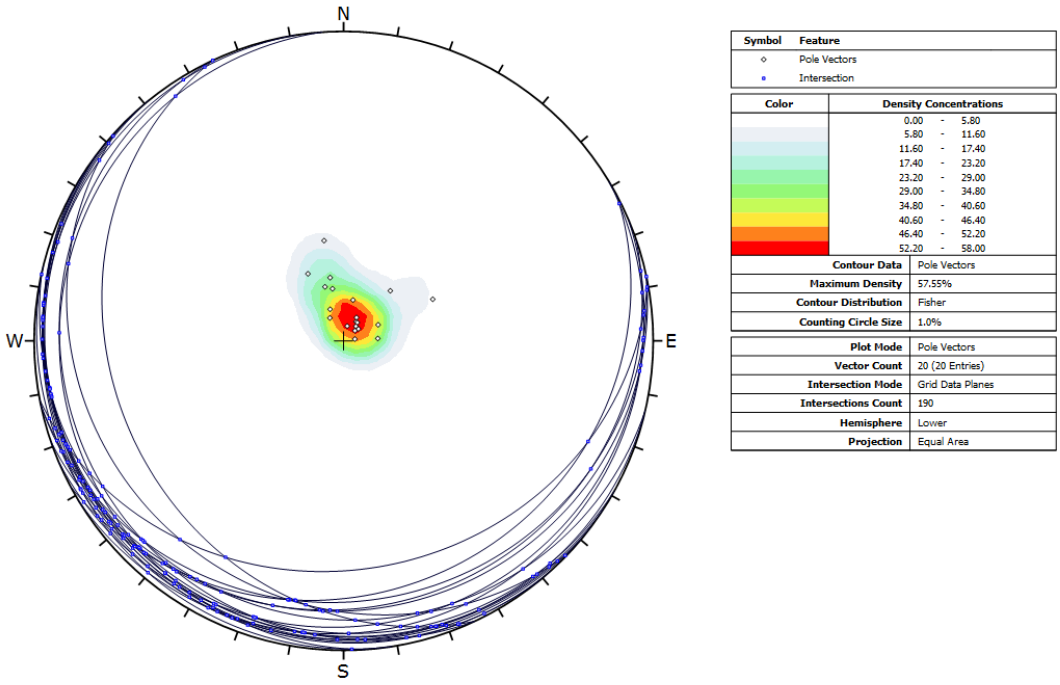

Figure 4.8 Stereonet illustrating dip/dip direction data collected from the lower Rangitawa Tephra- Upper Kauroa Ash boundary at 59 Hillcrest Road.

4.8 Deformation Structures

Tectonic activity is often present, and may be preserved in material by distinct geomorphic and geologic signatures. The Hillcrest Road cutting presented some structures of interest, which may be interpreted as tectonic deformation, but will require case study and elimination of other triggers before the hypothesis can be confirmed.

4.8.1 Deformed Bedding

Deformed bedding commonly provides an indication of tectonic deformation, however, may be a result of other triggers and deformation mechanisms. The Rangitawa Tephra unit in the field presented obvious contortion from a distance **Figures 4.9 and 4.10** provide photographs of the deformation. Along the base of the Rangitawa Tephra, in contact with the upper paleosol of the Kauroa Ash Formation, very wavy, almost bulbous-shaped, contortion structures are present extending downwards into the Kauroa Ash Formation. **Table 4.8** along with **Figure 4.11** illustrate and quantify the extent of deformation along the base contact of the Rangitawa Tephra unit. The mean deformation is 1.50 +- 0.46 metres long (excluding the 5.98-metre outlier). The largest deformation is 5.98 metres near profile 3.

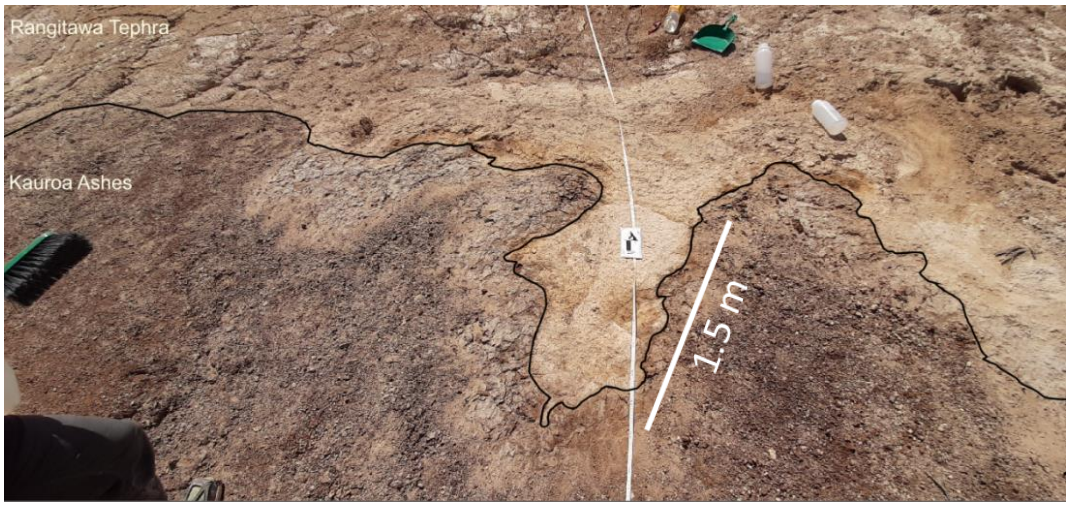

Figure 4.9 Expression of contorted lobes at the base of the Rangitawa Tephra contact with the upper Kauroa Ash Formation (position e-f).

Figure 4.10 Centimetre-scale deformation at the Rangitawa Tephra unit base contact with Kauroa Ash Formation.

Table 4.8 Measurements of deformed sections at base of the Rangitawa Tephra.

Position	Length (m)
a	2.50
b	1.32
c	1.13
d	1.16
e	1.40
f	1.50
g	5.98
Mean	2.14 +- 1.63
Mean exc. (g)	1.5 +- 0.46

Figure 4.11 Deformation at the base of the Rangitawa Tephra unit. Table 4.8 for measurements of each section (a-g).

4.8.2 Intrusion Structures

Deformation of units at Hillcrest road also included the presence of intrusion structures. These structures were noted in profile descriptions along profiles 2 and 3 at depths of 190 cm (H3/4) and 230 cm (H4/5) respectively within the Hamilton Ash Formation. The intrusions are distinct from the surrounding material in colour and texture. Infill of the structures appeared to be of light-grey silty material, surrounded by a more weathered yellowy-grey silty material. The intrusions occurred most commonly as vertical dikes, but in some places pooling and sills were identified, all of which pinching out as at the tops of the dikes and ends of the sills. **Figure 4.12** presents a light-grey brown coloured, silt-textured intrusion

structure at 190 cm depth along profile 2 within the Hamilton Ash Formation (H3 bed). The intrusion appeared to run both vertically into an orb of silty material and horizontally from this orb. **Figure 4.13** the same material is observed penetrating two centimetres into the upper Kauroa Ash Formation. A similar structure up close is presented in **Figure 4.14**. This picture was taken at 230 cm depth along profile 3 in the Hamilton Ash Formation (H4). The source of this material was not identified but is theorised to be caused by weathering processes along discontinuities, or injection of material from within the site.

Figure 4.12 Infilling of light grey silty material into clayey soil. Source could not be determined. Niwashi for scale. Running directly upwards at profile 2. (H3/4 Profile 2).

Figure 4.13 Infill of light grey and weathered silty textured material, and dark reddish-brown clayey material penetrating 2 centimetres downwards into the top of the Kauroa Ash Formation.

Figure 4.14 Light grey-brown silt-textured intrusion into the Hamilton Ash Formation (H4/5 profile 3). Composite figure of multiple photographs. Niwashi and tape measure for scale.

4.9 Summary

Earthworks at 59 Hillcrest Road during residential development provided opportunity to study and understand the deformation of hillslope units of the Hamilton Basin, particularly providing details into the tectonic impact along the southern Te Tatua o Wairere fault zone. The cutting exposed typical hillslope units Walton Subgroup units, followed by the Kauroa Ash Formation, overtopped by the full sequence of Hamilton Ash Formation (H1-H7) including the key research stratigraphic unit, the Rangitawa Tephra (H1). Structural data at the site indicated the Rangitawa Tephra unit is dipping gently at an angle of 11° toward the SSW. Following field analyses, evidence of deformation was exposed within the site, including deformed bedding, offset bedding, and intrusion-like structures. The Rangitawa Tephra had the most obvious deformation within the field, with significant contorted bedding around profiles 2 and 3, and a 5.98 metre displacement present near profile 3. Intrusion structures identified were present as light grey silty dike and sill infill structures within the Hamilton Ash Formation around the H3-H4 and H4-H5 units near profiles 2 and 3.

Tables 4.9 and 4.10 provide a summary of the laboratory results from these analyses.

Chapter 5

Results – Laboratory

5.1 Introduction

This chapter presents results from the various laboratory tests and analyses; static triaxial testing, Atterberg limits, particle-size analyses, thin section petrographic observations, X-Ray Diffraction (XRD) on bulk and clay separates, X-Ray Fluorescence (XRF), and scanning electron microscopy (SEM).

Texture, particle-size proportions, mineralogy, and fabric control the physical properties of soils. Physical properties are also controlled by moisture content and void spaces, varying depending on pressures and applied stresses. The below tests were used to classify and characterise the Rangitawa Tephra at Hillcrest Road to understand the behaviour and predict the response to applied stresses in the field, especially how the material may demonstrate deformation.

5.2 Particle-Size

Samples from Hillcrest Road (HCR1, HCR3, HCR5 Bot, HCR6 Bot, HCR5 Top, HCR6 Top, HCR7, Att. Paste 1, Att. Paste 2, and Att. Paste 3) were tested using the laser-sizer to identify the relative proportions of each particle-size fraction and the average particle size within each sample to provide an overall particle-size for the Rangitawa Tephra. Particle-size fractions include clay (< 0.39 μm), silt (0.39-63 μm), and sand (63-2000 μm) according to the Udden-Wentworth particle-size chart. The particle-size distribution graphs **(Appendix III (b)** were used, along with data collected from the particle-size analyses to produce a summary of median particle sizes and size class for each sample, and an average of all samples **(Table 5.1).** Raw data used in this section are presented in **Appendix III (a).**

The median proportion of each particle size suggests the fractions of clay, silt, and sand are relatively even. Clay has the highest median proportion at 39.59 % (± 10.67), next silt at 33.73 % (± 4.74); followed by the lowest proportion, sand 26.48 % (± 15.11) of which the majority was present as very fine (10.67 ± 2.42) to fine sand (14.04 ± 5.94). Outliers of extra sand in HCR3, HCR5 Top, and HCR6 Top may have skewed the median value of the sand fraction. The standard deviation for the Rangitawa Tephra sample particle-sizes is quite high. Clay fraction has a standard deviation of

±10.67, a third of the average, silt fraction ±4.74, a seventh of the average, and sand fraction ±15.11, approximately half the average.

Table 5.1: Clay, silt, and sand fraction proportions as volume percentage for each sample tested. Error assessment provided as standard deviation of median values.

Sample name	Clay %	Silt %	Sand %
HCR1	43.72	32.95	23.33
HCR3	18.99	26.66	54.35
HCR5 Bot	33.08	32.89	34.03
HC56 Bot	44.13	35.31	20.56
HC5 Top	17.77	26.12	56.11
HCR6 Top	24.83	23.58	51.59
HCR7	35.87	34.5	29.63
Att. Paste 1	47.64	36.94	15.42
Att. Paste 2	43.31	36.29	20.4
Att. Paste 3	44.54	37.45	18.01
Median	39.59 ± 10.67	33.73 ± 4.74	26.48 ± 15.11

Table 5.2: Proportions of each size fraction within sand fraction; very fine (63 – 125 µm), fine (125 – 250 µm), medium (250 - 500 µm), and coarse (500 - 1000 µm) fractions.

Sample name	Very-fine Sand %	Fine sand %	Medium sand %	Coarse sand %
HCR1	10.32	10.33	2.37	0.31
HCR3	13.33	22.79	17.28	0.95
HCR5 Bot	11.08	13.70	8.85	0.40
HC56 Bot	9.70	7.31	3.20	0.35
HC5 Top	13.92	23.78	17.47	0.94
HCR6 Top	12.36	21.33	16.58	1.32
HCR7	12.21	16.14	1.21	0.07
Att. Paste 1	4.56	9.58	1.28	0.00
Att. Paste 2	10.10	8.44	1.46	0.40
Att. Paste 3	9.10	7.04	1.77	0.10
Mean	10.67 ± 2.42	14.04 ± 5.94	7.15 ± 6.54	0.48 ± 0.40

Table 5.3: Median particle sizes (and standard deviations) of the Rangitawa Tephra samples from 59 Hillcrest Road, Hamilton.

Sample name	Median particle-size (µm)	Median size class
HCR1	5.55 ± 4.98	Very-fine silt
HCR3	82.8 ± 36.37	Very-fine sand
HCR5 Bot	15.2 ± 1.96	Fine silt
HCR6 Bot	5.18 ± 0.23	Very-fine silt
HCR5 Top	89.3 ± 4.01	Very-fine sand
HCR6 Top	70.7 ± 7.55	Very-fine sand
HCR7	10.6 ± 0.68	Fine silt
Att. Paste 1	4.34 ± 0.27	Very-fine silt
Att. Paste 2	5.41 ± 0.18	Very-fine silt
Att. Paste 3	5.01 ± 0.10	Very-fine silt
Average of all	29.41 ± 34.14	Medium silt

The average particle-size for samples is 29.41 µm; medium silt with a very large standard deviation (± 34.14). Particle-sizes ranged from clay to coarse sand as illustrated in the grain-size distribution graphs **(Figure 5.1 and Appendix III(b)).** Two distinct average particle-size fractions are present within this unit, which lead to the

average of medium silt. 1) Very fine to fine silts as present in HCR1, HCR5 Bot, HCR6 bot, HCR7, and Atterberg Pastes 1, 2, and 3. 2) Very-fine sand as present in HCR3, HCR5 Top, and HCR6 top.

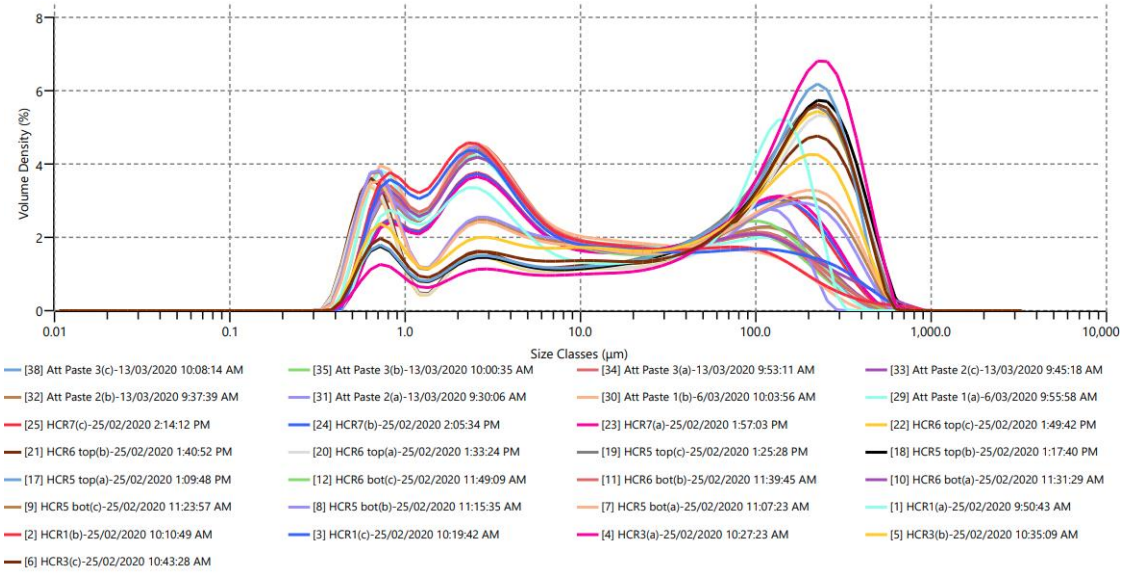

Figure 5.1: Particle-size distribution graph for all Hillcrest Rangitawa Tephra samples. Shows bimodal distribution of extra-fine silt, and extra-fine sand fractions.

5.3 Thin Section Petrography

This section describes the petrographic slides made from failed triaxial cores HCR1, HCR3, and HCR7, and an untested core sample HCR18 used as standard (Thin section chip illustrated in **Figure 5.2**). Thin sections were intended to identify the any failure planes/ deformation present after triaxial compression testing, thus, samples were used to identify the mineralogy present within the Rangitawa Tephra unit. The failed core samples did not exhibit clear failure planes. When viewed under the microscope, no microstructural failure planes could be identified, either. The high clay content within the samples made preparation of thin sections to the standard required for fracture assessment too difficult. The material is highly weathered, with a high proportion of clay which support the few grains of identifiable minerals in a matrix of very fine minerals. The matrix of clay mineralogy must be examined using XRD, XRF, and SEM. The microscope petrographic analyses indicated a high proportion of clay relative to primary minerals, supporting particle-size analyses, as all samples have over one-third clay-sized fraction **(Chapter 5.2).** The identified mineralogy in HCR1, HRC3, HCR7, and HCR18 was quartz, feldspar, mica, and a matrix of clay minerals **(Figure 5.3).**

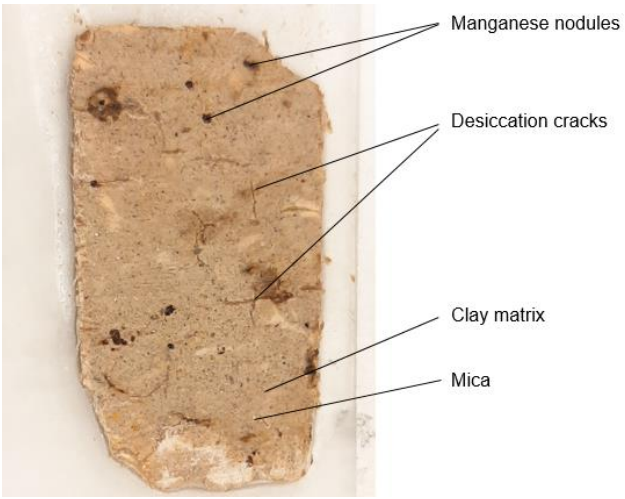

Figure 5.2: Example of Rangitawa Tephra thin section chip (HCR18)

HCR1 PPL and XPL. 50 x magnification.

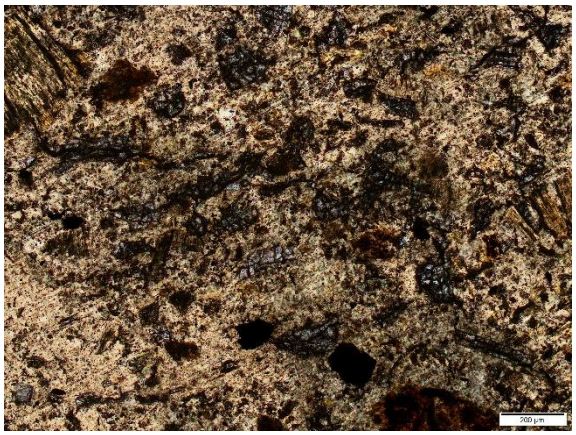

50 x magnification. PPL

400 um

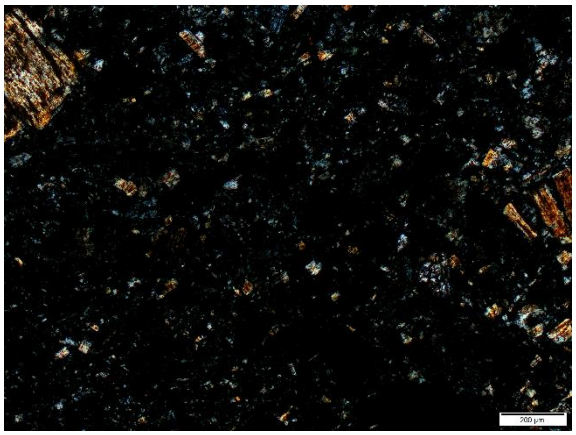

50 x magnification. XPL

400 um

HCR3 XPL and PPL 50x magnification.

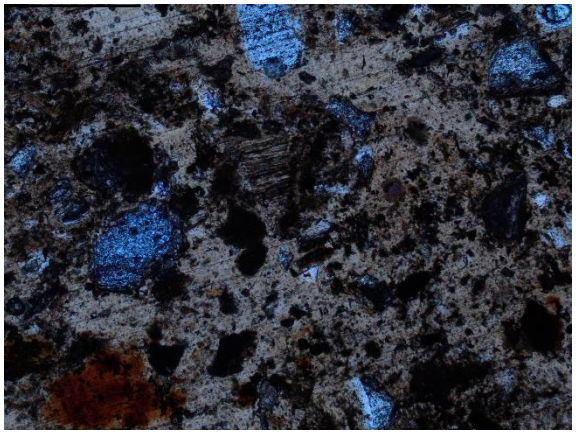

50 x mag. HCR3 PPL

400 um

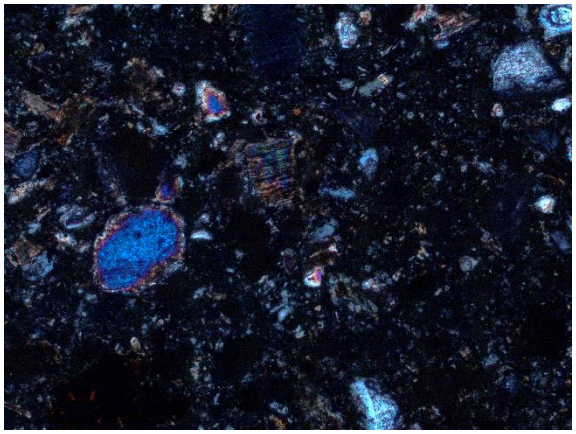

50 x mag. HCR3 XPL

400 um

HCR7 XPL and PPL 50x magnification.

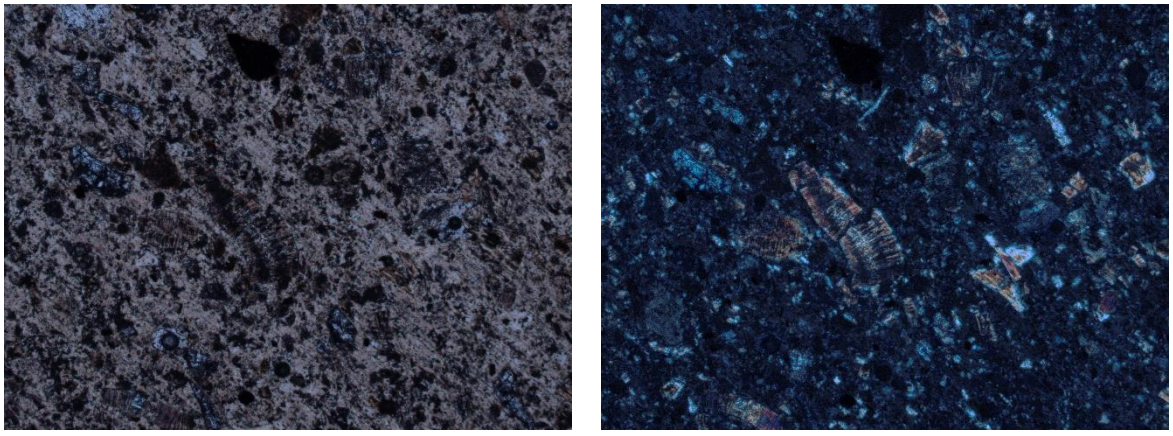

50 x mag. HCR7 PPL

50 x mag. HCR7 XPL

HCR18 PPL and XPL 50 x magnification.

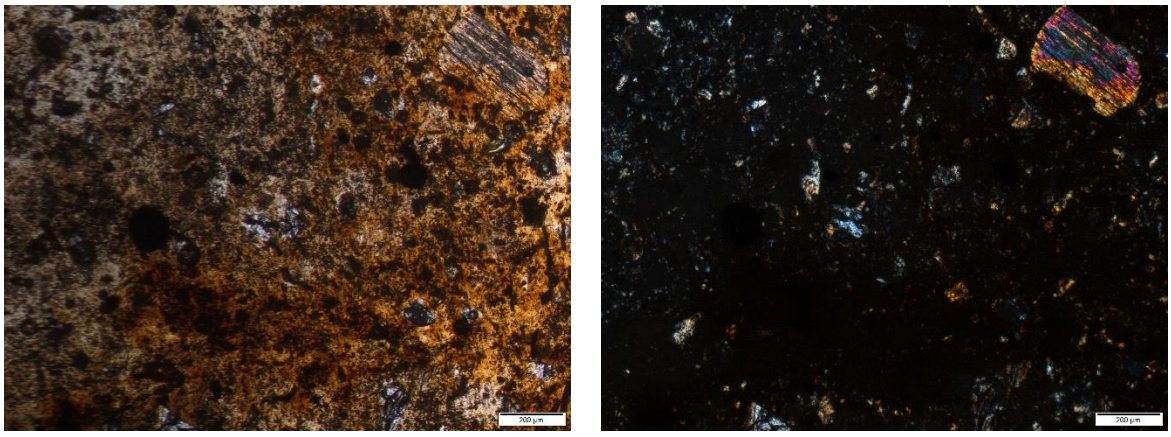

50 x mag. HCR18 PPL

50 x mag. HCR18 XPL

Figure 5.3: HCR1, HCR3, HCR7, and HCR18 photomicrographs illustrating thin section petrography.

5.4 X-Ray Diffraction (XRD)

5.4.1 Bulk samples

XRD analyses were completed on six bulk samples (HCR1, HCR3, HCR5 Bot, HCR5 Top, HCR6 Bot, and HCR6 Top) to identify the mineral assemblage of the Rangitawa Tephra at Hillcrest, Hamilton, supporting thin section petrographic analyses. The resulting diffraction patterns from the bulk geochemical analyses are provided in **Figures 5.4 (a-f)** below.

All samples display strong peaks at 7.21/7.22 Å indicating a large presence of kaolinite within each sample. Additional peaks signify presence of quartz, muscovite mica, and various feldspars such as sanidine present in HCR1, HCR3, HCR5 Top, HCR6 Bot, and HCR6 Top (all except HCR5 Bot), albite in HCR3, HCR5 Top, and andesine and microcline HCR5 Bot. HCR1 also indicates the presence of halloysite, and dickite inferred in HCR6 Bot.

Table 5.4 provides a summary of the mineralogy identified in the bulk XRD analyses. Dehydrated halloysite has a d-spacing of approximately 7 Å, suggesting the kaolinite and halloysite peaks may overlap/interchange, hence, halloysite may be present within the samples. Bulk XRD is inappropriate for heterogeneous samples as the amount of noise in the peaks makes it difficult to identify specific minerals. Rather, homogenous samples, such as clay separates are much more successful in identifying exact minerals. The section following below provides these analyses.

Table 5.4 Summary of minerals identified in 'bulk' XRD analyses.

Sample name	Quartz	Feldspars	Mica	Clay minerals
HCR1	quartz	sanidine	muscovite	kaolinite
HCR3	quartz	sanidine, albite	muscovite	kaolinite
HCR5 Bot	quartz	andesine, microcline	-	kaolinite
HCR5 Top	quartz	sanidine, albite	muscovite	kaolinite
HCR6 Bot	quartz	sanidine	muscovite	kaolinite, halloysite, dickite
HCR6 Top	quartz	sanidine	muscovite	Kaolinite

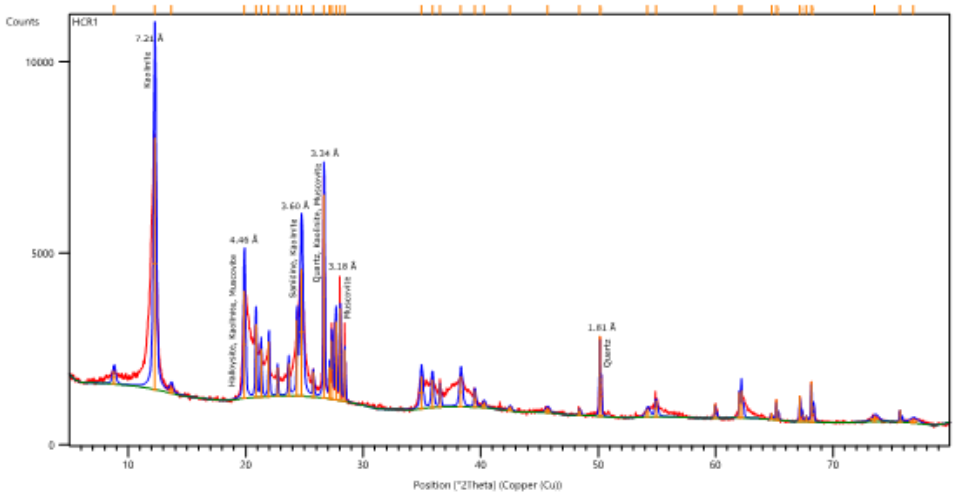
Counts
HCR1
7.24 Å
Kaolinite
4.46 Å
Halloysite, Kaolinite, Muscovite
3.60 Å
Sanidine, Kaolinite
3.34 Å
Quartz, Kaolinite, Muscovite
3.18 Å
Muscovite
1.81 Å
Quartz
Position [°2Theta] (Copper (Cu))

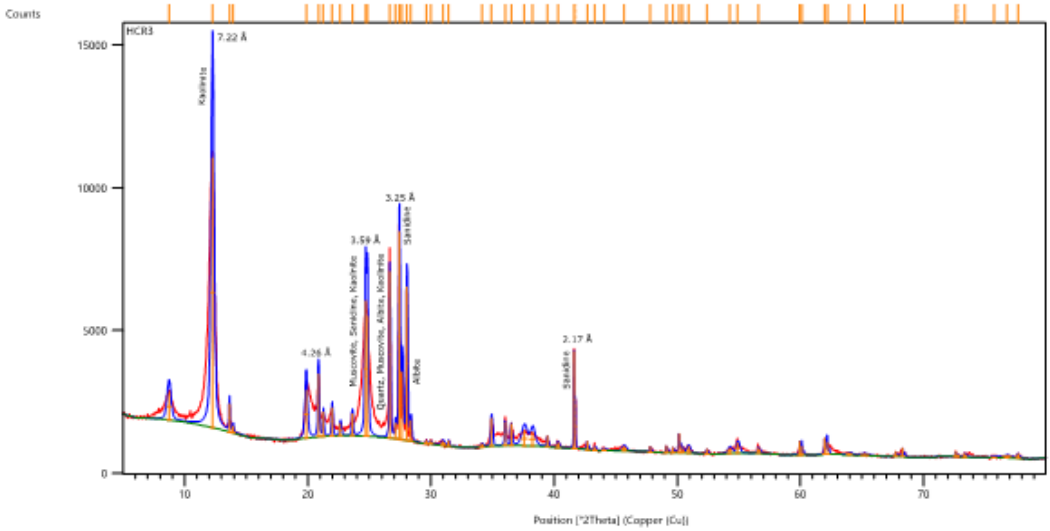
Counts
HCR3
7.22 Å
Kaolinite
4.26 Å
3.59 Å
Muscovite, Sanidine, Kaolinite
3.25 Å
Quartz, Muscovite, Albite, Kaolinite
Sanidine
Albite
2.17 Å
Sanidine
Position [°2Theta] (Copper (Cu))

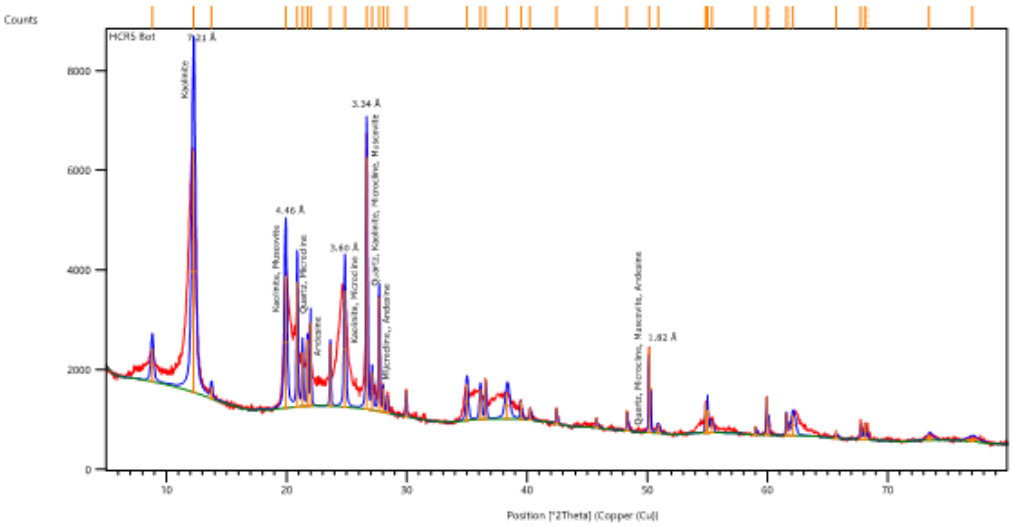
Counts
HCR5 Bot
7.21 Å
Kaolinite
4.46 Å
Kaolinite, Muscovite
Quartz, Microcline
Andesine
3.60 Å
Kaolinite, Microcline
3.34 Å
Quartz, Kaolinite, Microcline, Muscovite
Microcline, Andesine
1.82 Å
Quartz, Microcline, Muscovite, Andesine
Position [°2Theta] (Copper (Cu))

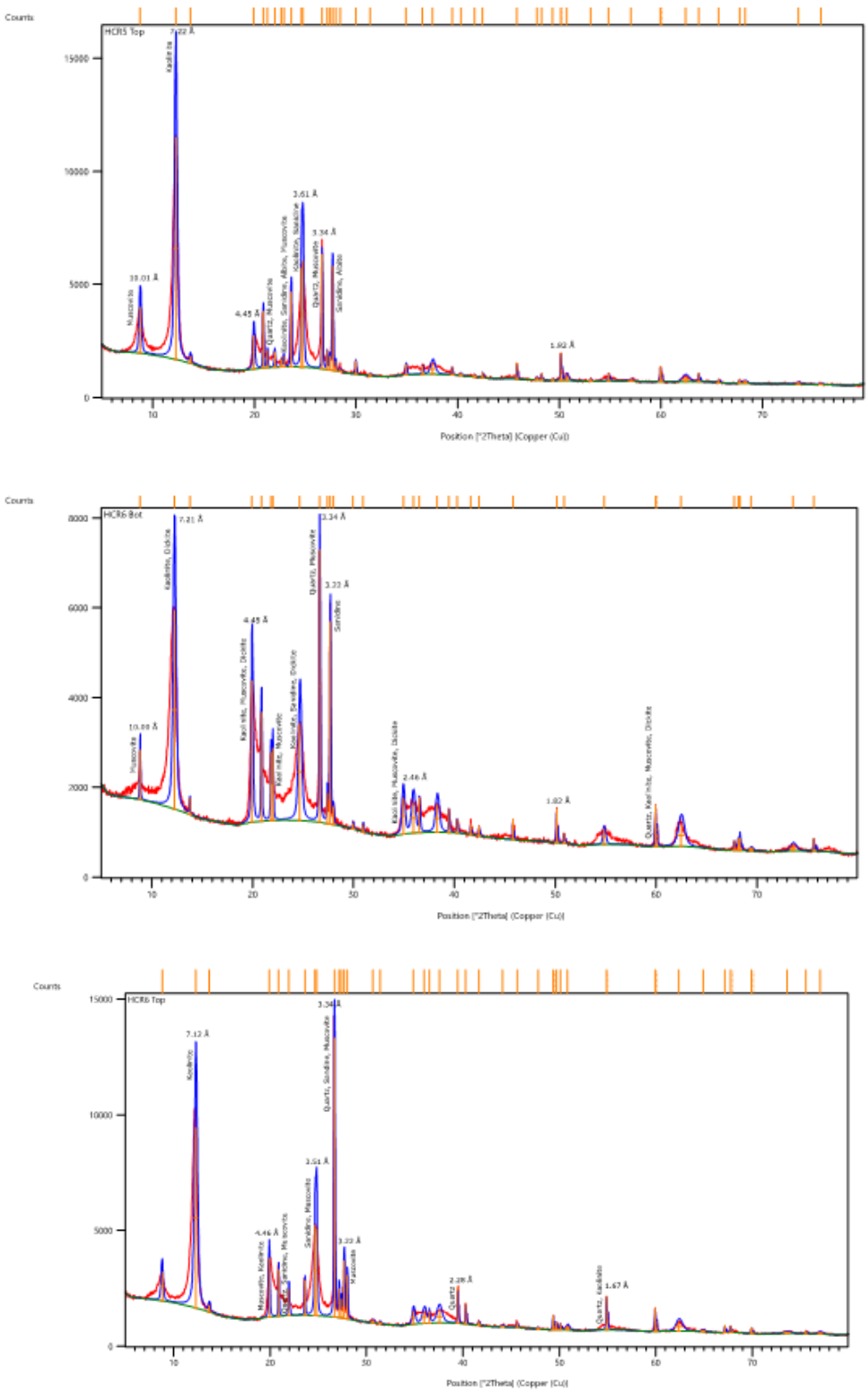

Figure 5.4(a-f) XRD patterns for samples HCR1, HCR3, HCR5 Bot, HCR5 Top, HCR6 Bot, and HCR6 Top.

5.4.2 X-Ray Diffraction: Clay Separates

Clay separates were analysed under the XRD to identify the clay mineralogy, thereby supporting bulk XRD analyses completed in **Chapter 5.4.1**. **Figures 5.6.2 (a-e)** illustrate the results from these analyses. The untreated (blue) clay tiles resulted in d-spacing of ~10 Å in all samples. Treating with ethylene glycol (green) in most cases lead to expansion to 11 Å with the exception of HCR6 Top, which remained at 10 Å. Heating at 110°C (red) for an hour caused an increase to 12 Å. Heating at 550°C for an hour (pink) lead to complete destruction of the clay mineralogy. Using the USGS Clay Mineral Identification Flow Diagram (US Geological Survey, n.d.) it was determined all samples tested are 10 Å halloysite (aka. endellite). All samples increased to 12 Å rather than collapsing to 7Å, which is quite strange. Despite this,

hydrated halloysite is the best fit of all clay minerals in the flow diagram from USGS (US Geological Survey, n.d.).

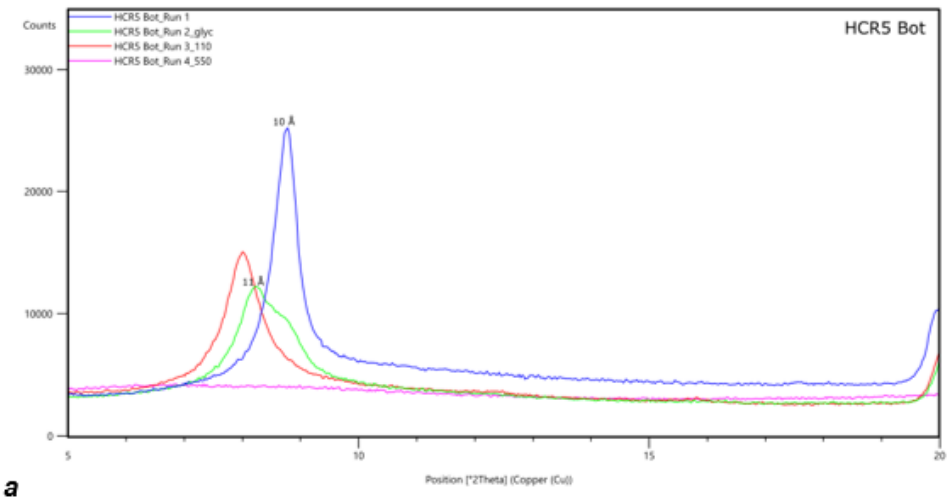

a

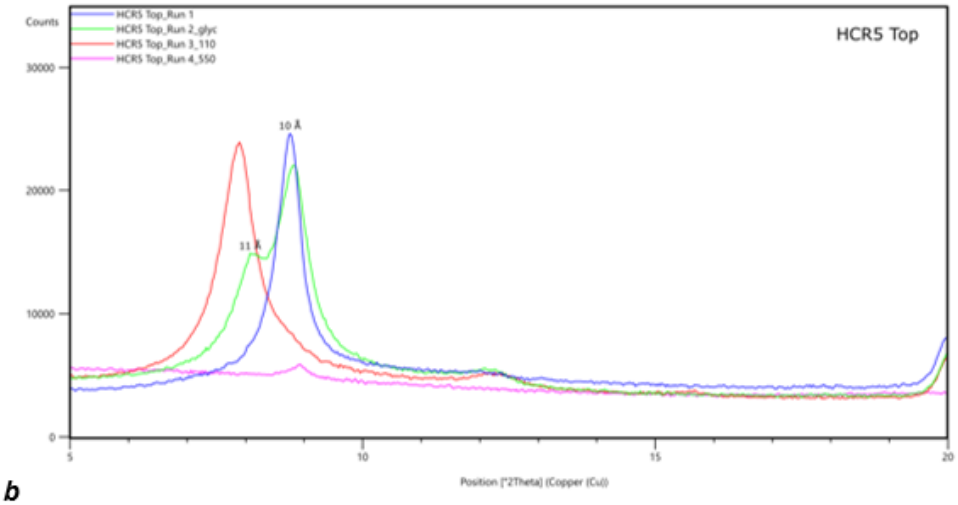

b

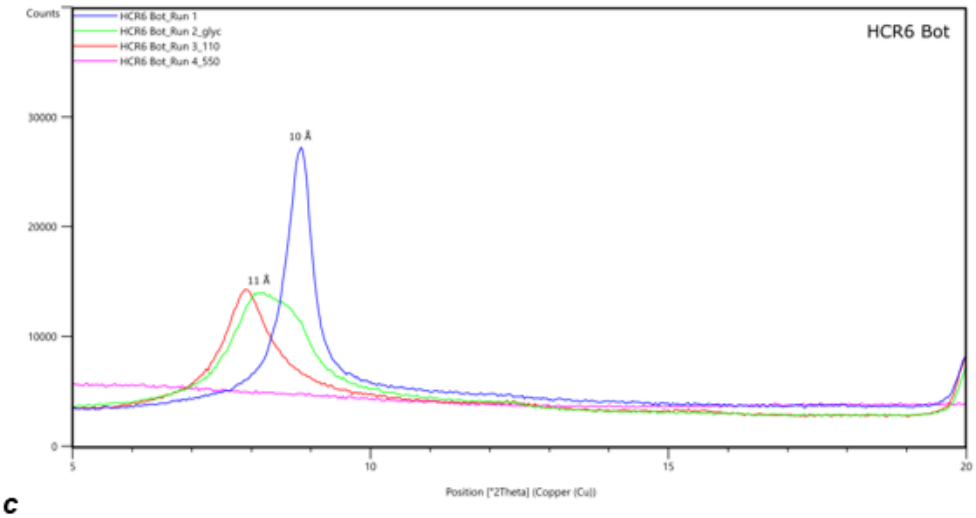

c

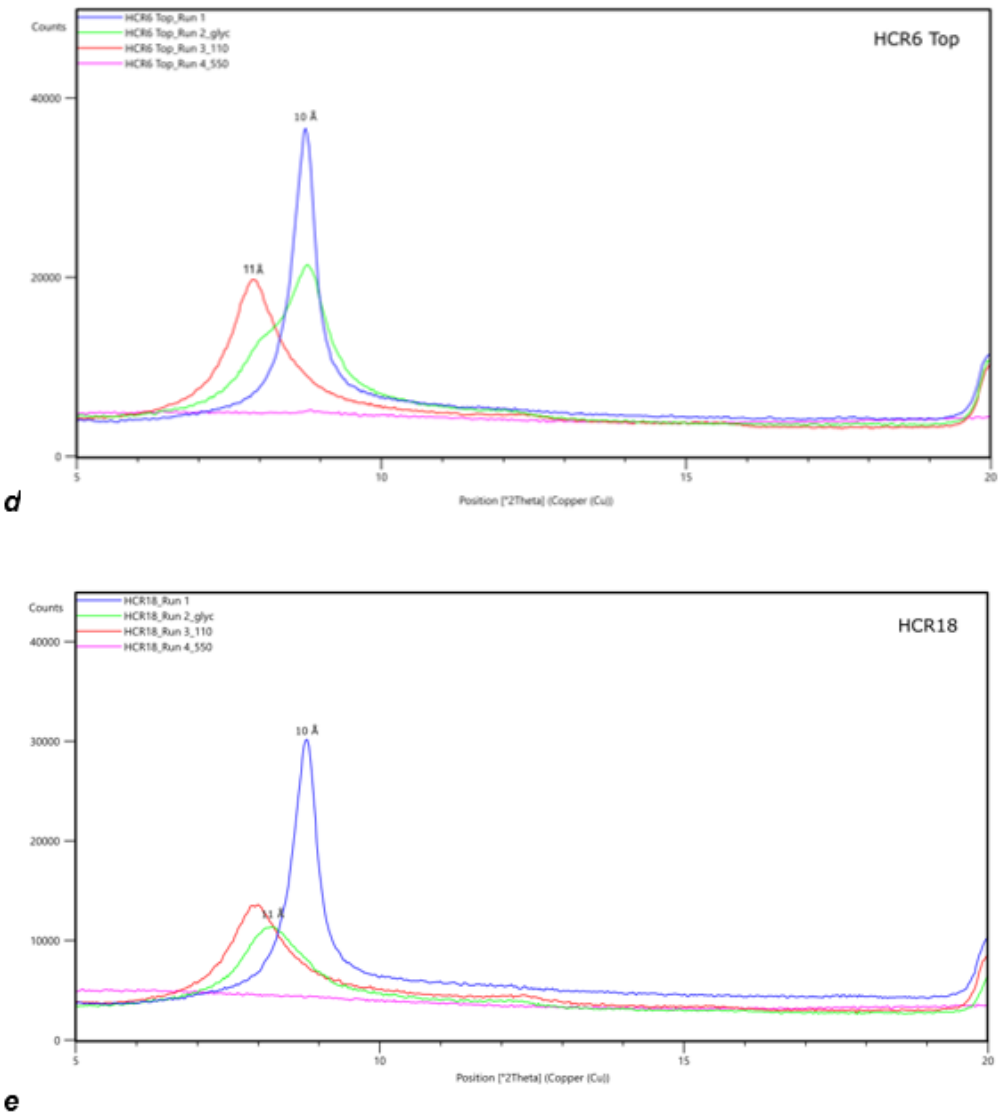

Figure 5.5 (a-e). X-ray diffraction patterns for fines samples (HCR5 Bot, HCR5 Top, HCR6 Bot, HCR6 Top, and HCR18) from the Rangitawa Tephra at Hillcrest, Hamilton.

5.5 X-Ray Fluorescence (XRF)

The samples tested in XRF analyses were 'bulk' samples, as the material was oven-dried and ground to a fine powder. These samples were analysed for major elements and two trace elements (Sr and Ba). Normalised chemical compositions for SiO2, Al_2O_3, TiO_2, MnO, Fe_2O_3, MgO, Na_2O, K_2O, P_2O_5, SO_3, CO_2, SrO, and BaO are listed in **Table 5.5** with Harker variation plots of the results vs. SiO2 content are presented in **Appendices V.**

SiO_2 abundances range from 50.63 to 55.37 % with a mean abundance of 52.23 ± 2.34 %. Another key compound for this research is the Al_2O_3 content as it identifies transformation of material to clay minerals. Al_2O_3 content ranges from 25.94 to 30.22 % with an average of 28.35 ± 1.63 % (**Table 5.7**).

Intra-unit variation (expressed by standard deviations) is low (i.e. ± 2.34 SiO_2, ± 1.63 Al_2O_3, ± 0.06 TiO_2) suggesting the Rangitawa Tephra at Hillcrest Road is largely homogenous. The highest variation exists in the CaO (± 0.12), Na_2O (± 0.34), and K_2O (± 0.53) values. These are small values generally so the variation means little overall.

The total for each sample falls just short of 100%; this is likely due to chemistry within the samples not accounted for in this round of XRF analyses and/or error in weighing/other measurements.

Table 5.5: Normalised XRF values of bulk Hillcrest Rangitawa Tephra samples. All samples measured in wt. % to 2 d.p. except Sr and Ba measured in PPM presented as a whole number. LOI % expressed as CO_2 %.

Sample	HCR1	HCR3	HCR5 Top	HCR5 Bot	HCR6 Top	HCR6 Bot	HCR7	HCR18	Mean
SiO_2	50.63	55.37	54.64	53.12	53.67	48.45	50.90	51.08	52.23 ± 2.34
Al_2O_3	30.22	26.35	25.94	27.64	27.90	29.19	29.92	29.59	28.35 ± 1.63
TiO_2	0.47	0.49	0.57	0.46	0.40	0.41	0.42	0.40	0.45 ± 0.06
MnO	0.07	0.04	0.03	0.04	0.03	0.03	0.07	0.04	0.04 ± 0.01
Fe_2O_3	4.26	4.06	4.44	4.04	3.60	3.64	3.82	3.76	3.95 ± 0.30
MgO	0.22	0.43	0.49	0.32	0.36	0.26	0.26	0.25	0.33 ± 0.10
CaO	0.28	0.37	0.40	0.20	0.34	0.09	0.13	0.13	0.24 ± 0.12
Na_2O	0.54	1.04	1.12	0.62	0.95	0.29	0.35	0.35	0.66 ± 0.34
K_2O	0.56	1.58	1.78	0.96	1.40	0.50	0.55	0.56	0.98 ± 0.53
P_2O_5	0.019	0.018	0.020	0.020	0.017	0.019	0.020	0.018	0.019 ± 0.001
SO_3	0.020	0.030	0.050	0.031	0.030	0.020	0.050	0.030	0.030 ± 0.01
CO_2	12.64	10.08	10.36	12.43	11.18	16.99	13.41	13.73	12.60 ± 2.22
Sr – PPM	30	55	60	37	55	19	29	26	39 ± 16
Ba – PPM	519	1198	1298	917	1093	750	833	445	882 ± 307
Sum (%)	99.93	99.86	99.85	99.89	99.88	99.89	99.90	99.94	n = 8
LOI (%)	12.64	10.08	10.36	12.43	11.18	16.99	13.41	13.73	12.60 ± 2.22

The LOI % is calculated as the weight lost from the samples after heating in a furnace overnight. This is presented as CO_2 in Table 5.5. The mean LOI is 12.60 with a standard deviation of 2.22 %. The LOI % is very high, thus indicating a significant amount of weathering of the Rangitawa Tephra unit has taken place (ref).

Appendix V(b) provides Harker variation plots used to illustrate relationships between SiO_2 and the other tested compounds. With an increase of SiO_2 wt. percentage there is an increase of TiO_2 (weak relationship $R^2 = 0.34$), MgO (moderate relationship $R^2 = 0.75$), CaO (moderate relationship $R^2 = 0.72$), Na_2O (strong relationship $R^2 = 0.84$), K_2O (strong relationship $R^2 = 0.84$), BaO (moderate

relationship R^2 = 0.62), and SrO (strong relationship R^2 = 0.88). With the increase of SiO_2 there is a decrease of Al_2O_3 (moderate relationship R^2 = 0.74) and CO_2 (strong relationship R^2 = 0.90). Little to no trend for MnO, Fe_2O_3, P_2O_5, and SO_3 (R^2 < 0.3).

5.6 Scanning Electron Microscopy (SEM)

The scanning electron microscope (SEM) supplements XRD findings by providing a morphological image of minerals observed. This ability is especially important for clay when a single mineral can occur as a number of morphologies (Selby, 1993). Under the SEM, remoulded Rangitawa Tephra samples from Hillcrest Road were analysed to identify morphologies of the clay fraction to aid identification. **Figures 5.6 a-f** illustrate the clay-mineral morphologies identified in SEM analyses. The samples analysed under the SEM exposed two primary morphologies present, spheroid and tubular forms (Shepherd, 1984; Selby, 1993). The spheroid morphologies were measured to have an average diameter of 200 nanometres, aggregating together to form clusters 500 nanometres to two micrometres in size. The tubular forms were measured relative to the scale bar and identified to have an average length of 500 nanometres, diameter of 50 nanometres, and walls are approximately 5-10 nanometres thick.

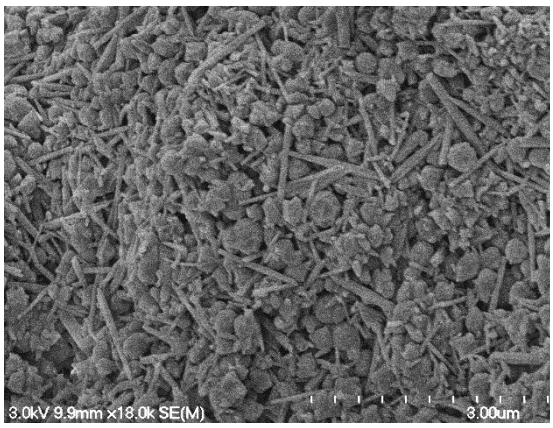

a: Air-dried. 6 um field of view.

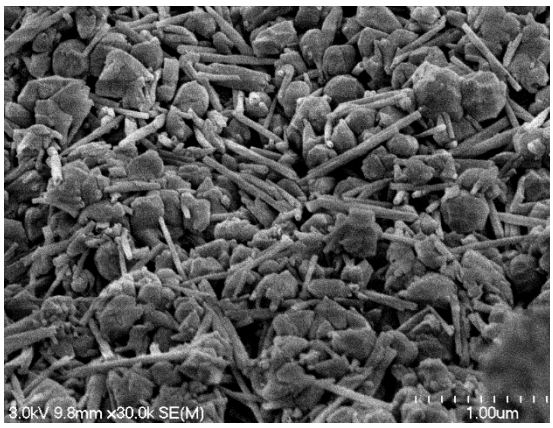

b: Air-dried. 5 um FOV.

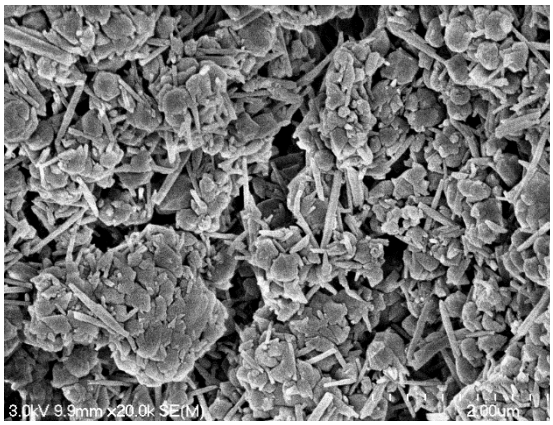

c: Air-dried. 6 um FOV

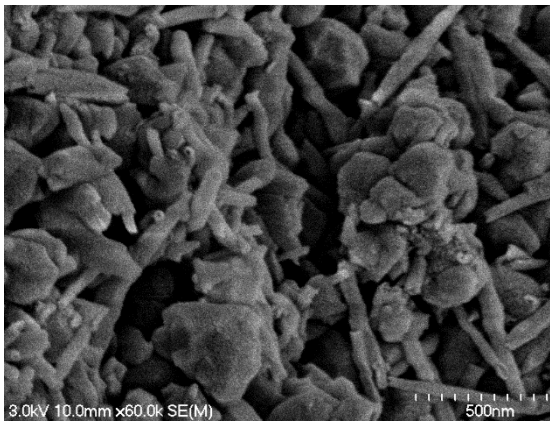

d: Air-dried. 2 um FOV.

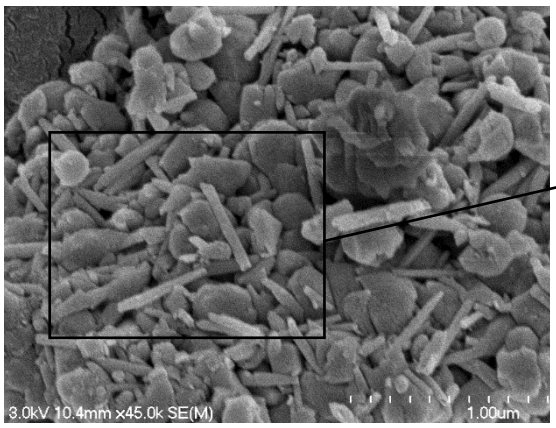

e: Oven-dried. 3 um FOV

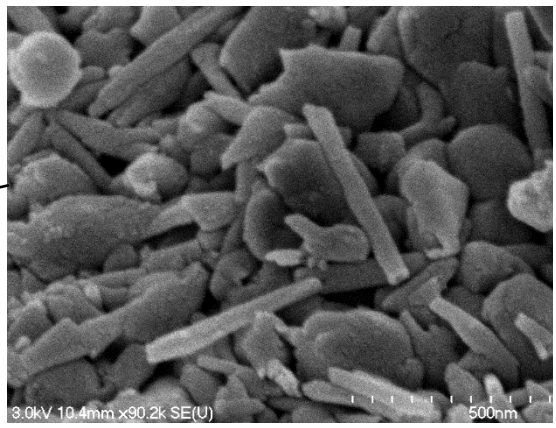

f: Oven-dried. 1.5 um FOV

Figures 5.6 a-f: Remoulded Hillcrest Rangitawa Tephra samples, either air-dried or oven-dried (Air-dried at room temperature for 24 hrs. Oven-dried at 110 C for 24hr). Illustrates long hollow tubular forms, and large spheroidal morphologies of halloysite.

5.7 Atterberg Limits

Fine-grained soils (clay, silts, and organic matter of similar sizes) exist in a range of states. The water content at transitions between these states is a widely used mechanical test for soils. A general relationship exists between the particles and the capacity to attract and hold water at their surfaces and the limits calculated in Atterberg Limits testing. Despite this, there is no definite relationship between these limits and the volume of adsorbed water. The index limits are best used to classify a soil based on their activity and soil fraction (expressed in the Plasticity **Figure 5.8**) (Selby, 1993). The Atterberg limits analyses were carried out using the drop-cone penetrometer method (Campbell, 1975) to quantify the moisture content at which changes from a liquid state to a plastic state (liquid limit), from a plastic state to a semisolid state (plastic limit) occur. **Table 5.6** and **Figure 5.8** present Atterberg Limit results for Rangitawa Tephra samples. Raw data presented in **Appendices VI.**

Table 5.6 Summary of Atterberg Limit results from the Hillcrest Rangitawa Tephra samples including mean and standard deviations. Inferred mineralogy from Selby (1993). The R_2 value provides the strength of the relationship between penetration depth and moisture content as a form of statistical error analyses.

Test	NMC (% water)	PL %	LL %	PI	LI	Activity	A-line class-ification	Mineralogy	R^2
3	35.72	32	46	14	0.26	0.29	ML	Dehydrated halloysite or Kaolinite	1.00
4	35.72	32	46	14	0.25	0.29	ML		1.00
6	36.08	30	46	16	0.38	0.36	ML		0.99
9	32.26	30	44	14	0.14	0.31	ML		0.99
10	32.26	30	45	18	0.1	0.40	ML		0.99
Mean	**34.41 ± 1.76**	**31 ± 0.98**	**45 ± 0.80**	**15 ± 1.60**	**0.23 ± 0.10**	**0.33 ± 0.04**	**ML**	**Dehydrated halloysite or Kaolinite**	**-**

The Plastic Limit (%) indicates the moisture content at which the material transitions from plastic to solid state. The mean PL calculated was 31%, with a range from 30 to 32 % sitting in the range of medium to high PL (Selby, 1993; Briaud, 2016). The Rangitawa Tephra from Hillcrest Road has a calculated natural moisture content of 34.41% water, ranging from 32.26 to 36.08%. This value lies above the plastic limit, inferring the natural state of the Rangitawa Tephra is plastic. Mean LL is 45 %, with a range of 44 to 46 %. PI ranges from 14 to 18 %, at a mean of 15 %. This indicates the tested Rangitawa Tephra is of low to medium plasticity (Selby, 1993; Briaud, 2013). Liquidity Index ranges from 0.1 to 0.38, with a mean of 0.23. The relationship between PI and LL are plotted onto a Plasticity chart **(Figure 5.7)** and used to classify the tested samples based on dominant particle-size fraction and compressibility. The

plotted values for tests 3, 4, 6, 9, and 10 all plot below the A-line under the classification ML. This suggests the Rangitawa Tephra samples were silts of low compressibility. Activity for the Atterberg Limits tests was calculated by dividing the plasticity index by the percentage clay in the samples **(Appendix VI (b)).** Activity ranged from 0.29 to 0.40, and a mean of 0.33. Activity values less than 0.75 are considered inactive, indicating the presence of non-swelling clays (Selby, 1993).

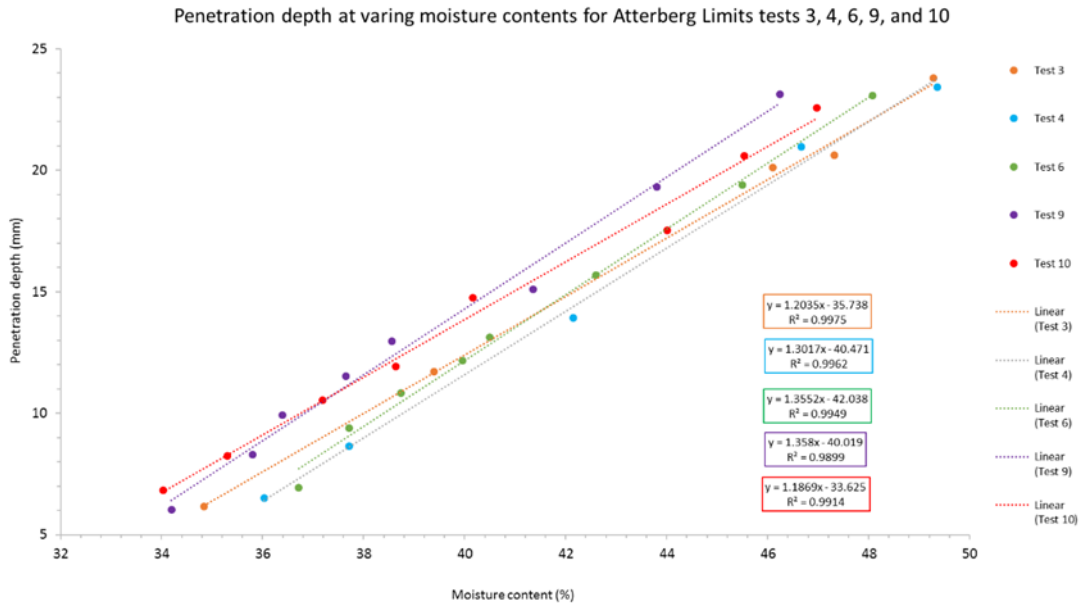

Figure 5.7: Penetration depths at varying moisture contents of the samples from Hillcrest Road for tests 3, 4, 6, 9, and 10.

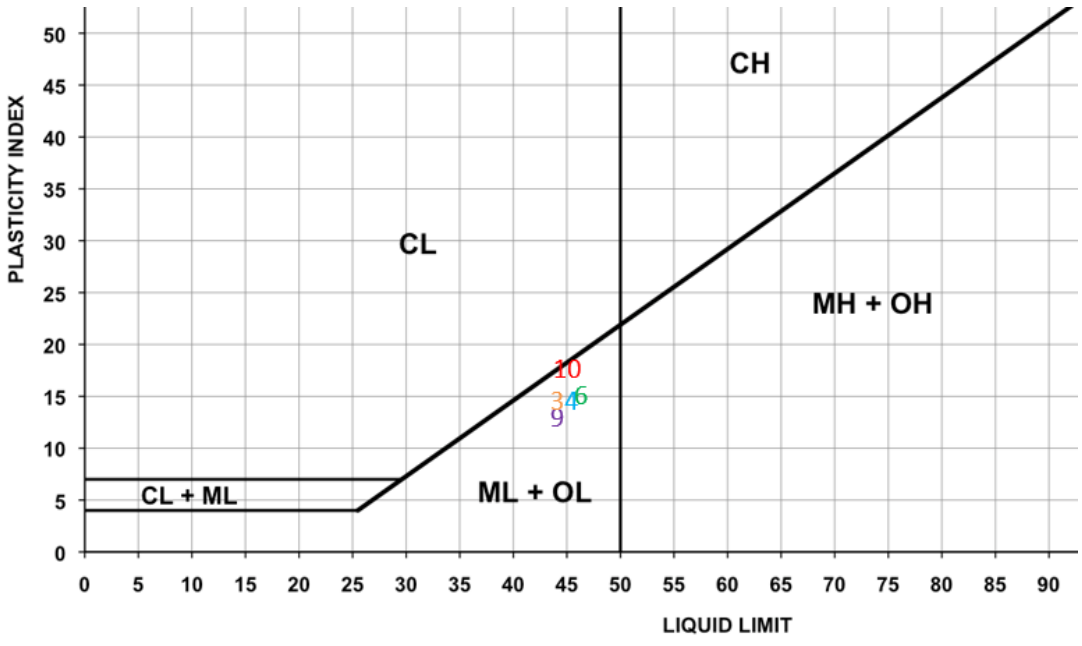

Figure 5.8 A-line Plasticity chart for the Hillcrest Rangitawa Tephra Atterberg Limits tests 3, 4, 6, 9, and 10. A-Line chart modified from Briaud (2013).

5.7.1 Errors in Atterberg limits

Tests 1 and 2 did not turn out as expected; the moisture content did not increase as water was added to the paste despite the penetration depth increasing. It is suspected the subsamples at each stage were left out in the hot, dry air for too long before weighing an placing in the oven therefore allowing them to dry out slightly before moisture contents could be undertaken and leading to errors in the results. Tests 1, 2, 5, 7, and 8 were omitted from the main data as a result but have been presented in **Appendices VI.**

The Rangitawa Tephra samples apparently dried and dehydrated slightly during testing, storage, and laboratory testing thereby leading to lower water contents than naturally expressed *in situ,* leading to small-unquantified errors in calculated Atterberg limits.

5.8 Static Triaxial

Bulk densities of the units overlying (HB samples), the depth of the unit, along with the depth of the water table were used to calculate the estimated pressure of the overlying soil column (kPa). (**Appendix VII (a))** indicated 78.5 kPa overburden stress on the Rangitawa Tephra unit at Profile 4 Hillcrest Road. Testing at 50, 100, and 150 kPa axial stress were chosen to represent the geomechanical properties of the Rangitawa Tephra under stress. Consolidated, undrained static triaxial compression tests were carried out on samples HCR1 (100 kPa), HCR3 (150 kPa), and HCR7 (50 kPa) with the applied stress conditions defined in **Table 5.7 (Appendices VII for raw data and calculations)**. The following section will present results of Mohr Coulomb analyses for both total and effective stresses, effective stress paths (p'-q plot), and stress-strain plots with pwp-strain.

Table 5.7 Testing parameters for triaxial analyses of the Rangitawa Tephra samples (HCR1, HCR3, and HCR7) from 59 Hillcrest Road.

Test number	Sample name	Cell Pressure (kPa)	Back Pressure (kPa)	Effective confining pressure (kPa)
1	HCR1	740	640	100
2	HCR3	740	490	150
3	HCR7	600	550	50

Figure 5.9 illustrates the relationship between axial strain (%) and axial stress (kPa) for the tested samples. As the stress increased, the strain also increased. All samples follow very similar trends. This figure was utilised to identify the ultimate and/or yield strength for each sample during testing. No (brittle) failure point is apparent in this

graph, rather the stress continues to increase until the test ended. Ultimate strain for HCR1 is 19.25 % at 985.65 kPa. HCR3 19.32 % strain at 1098.96 kPa. HCR7 19.62 % at 762.98 kPa, all of which are when the test was ended. Rather than failing in a brittle way, the material appears to be deforming in a ductile-plastic manner.

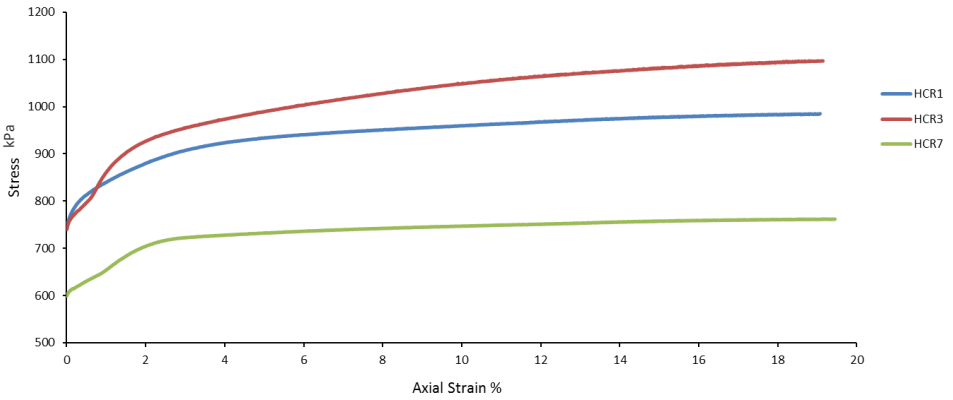

Figure 5.9 Axial Strain (%) versus Axial Stress (kPa) relationship for samples HCR1, HCR3, and HCR7 from Hillcrest Road.

Figure 5.10 illustrates the relationship between axial strain (%) and pore water pressure (kPa) during the compression test. Following failure at peak deviator stress, the material expands in volume (dilation) causing the pore water pressure to become negative thus increasing the effective stress (Briaud, 2013). Samples HCR1, HCR3, and HCR7 peaked at pwp of 63, 83 and 14 kPa before trailing off to -7, -48, and -28 kPa, respectively.

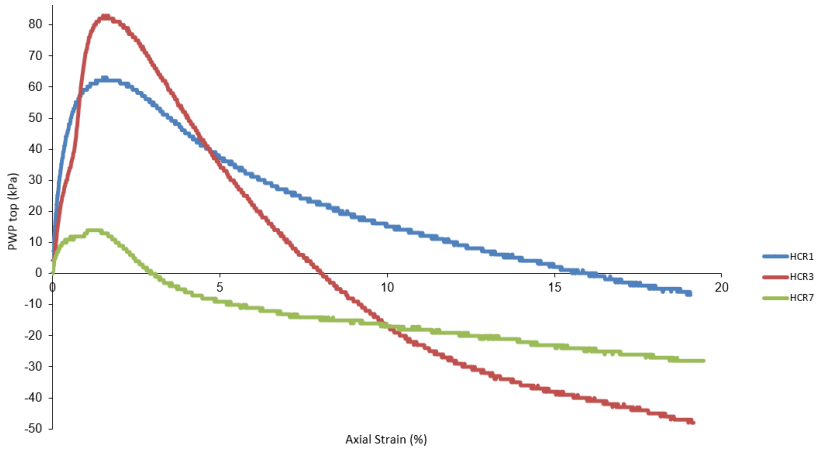

Figure 5.10 PWP (kPa) vs Axial Strain (%) relationship for samples HCR1, HCR3, and HCR7.

Figure 5.11 provides the Mohr circles for total normal stress, and **Figure 5.12** for effective normal stress. The diagrams were utilised to determine the normal and effective cohesion and friction angles for the Rangitawa Tephra at Hillcrest Road. The cohesion values calculated were c= 17.2 kPa and c'= 11.2 kPa and effective friction angles 29.7° and 40.5° respectively.

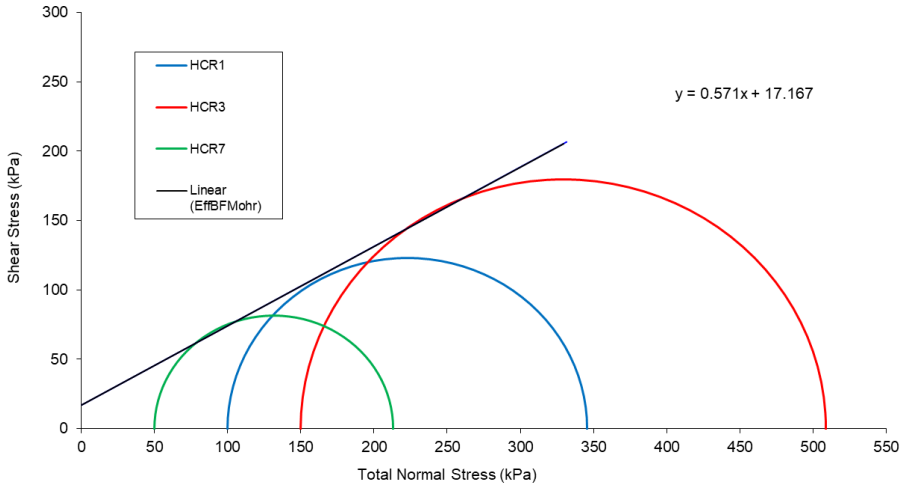

Figure 5.11: Mohr circles of total normal stress vs shear stress for consolidated, undrained triaxial test samples HCR1, HCR3, and HCR7.

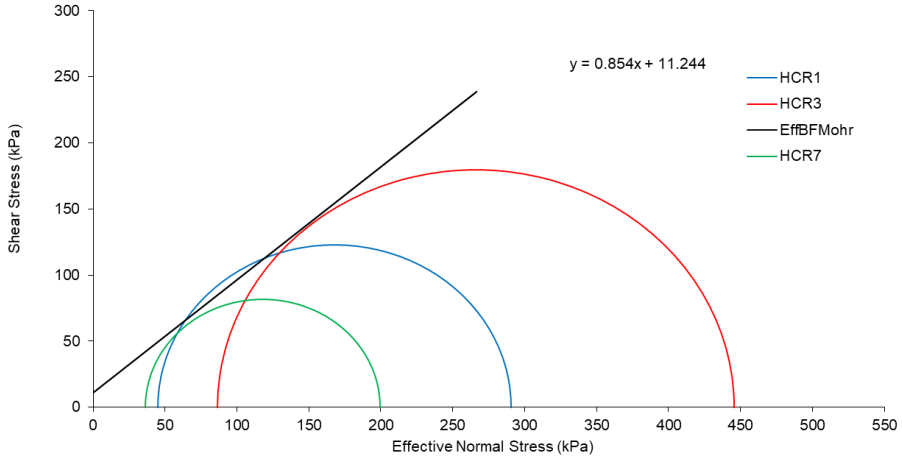

Figure 5.12 Mohr circles of effective normal stress vs shear stress for consolidated, undrained triaxial test samples HCR1, HCR3, and HCR7.

Figure 5.13 illustrates the evolving relationship between p' [(σ1 + σ3)/2] and q [(σ1 – σ3)/2] (kPa) for the three tested samples. The gradient of the critical state line for HCR1, HCR3, and HCR7 are 0.56, 0.55, and 0.57 respectively, expressing the stress paths follow very similar trends. Stress paths for all samples trend gently toward the right of the critical state line. This expresses dilation within the samples, often associated with the presence of over-consolidated sands (Briaud, 2013). The samples did not have significant enough sand fractions for this result to be appropriate.

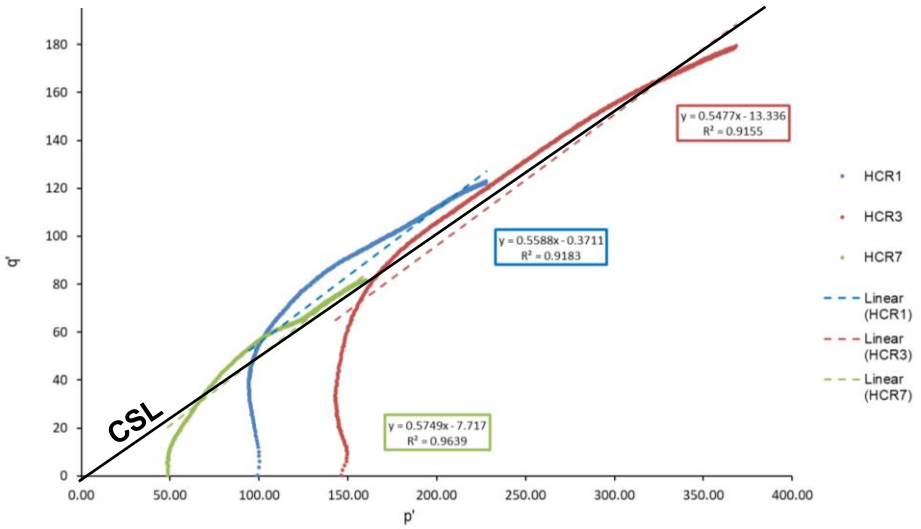

Figure 5.13 p'-q' graph of failure envelopes for triaxial test samples HCR1, HCR3, and HCR7.

Table 5.8 provides a summary of the results collected during the undrained, consolidated triaxial tests and figures above.

Table 5.8 Summary of undrained, consolidated triaxial test results.

Sample name	c (kPa)	c' (kPa)	Ø (°)	Ø' (°)	$p'_{Failure}$ (kPa)	q' (kPa)	Peak PWP (kPa)	Final PWP (kPa)	Peak axial strain (%)	Peak axial stress (kPa)
HCR1					228	122.8	63	- 7	19.25	985.65
HCR3	17.2	11.2	29.7	40.5	368.5	179.5	83	- 48	19.32	1098.96
HCR7					160.1	81.5	14	- 28	19.62	762.98

Post-triaxial test sample condition

Photographs of the failed samples (HCR1, HCR3, and HCR7) presented in **Figures 5.14- 5.16** indicating the failure modes contributing to deformation. Selby (1993) provides four failure modes for triaxial specimens – a) brittle - shear failure, b) brittle to ductile - wedge failure, c) ductile - intermediate failure, d) ductile-plastic - barrel failure. **Figure 5.14** presents the various modes. The samples tested are assigned a failure mode based on Selby (1993) **(Figure 5.14).**

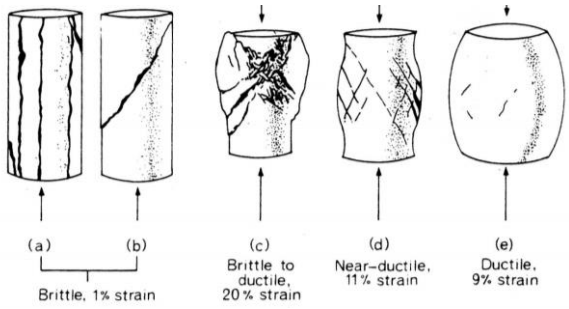

Figure 5.14: Failure modes of static triaixal cores. Figure source Selby (1993).

Figure 5.15 demonstrates the failure mode of HCR1 where the red lines indicate points of deformation. The figure shows near ductile deformation (Selby, 1993). The sample did not rupture following the yield point- as can be seen in figure 5.8; the strain continues to rise to 19.25 % until the test ends indicating the sample exhibits ductile-plastic behaviour.

Figure 5.15 HCR1 Failed Triaxial core annotated figures. Tested at <u>100 kPa</u> under undrained, consolidated conditions.

Figure 5.16 demonstrates the failure mode of HCR3. Like HCR1, the sample barrelled (bulged) and cracked slightly. This expresses a near ductile failure mode (11 % strain – Selby, 1993). Like HCR1, the sample did not appear to rupture post- yield (**Figure 5.8),** rather, the strain rises to 19.32 %– indicating the sample is of plastic material.

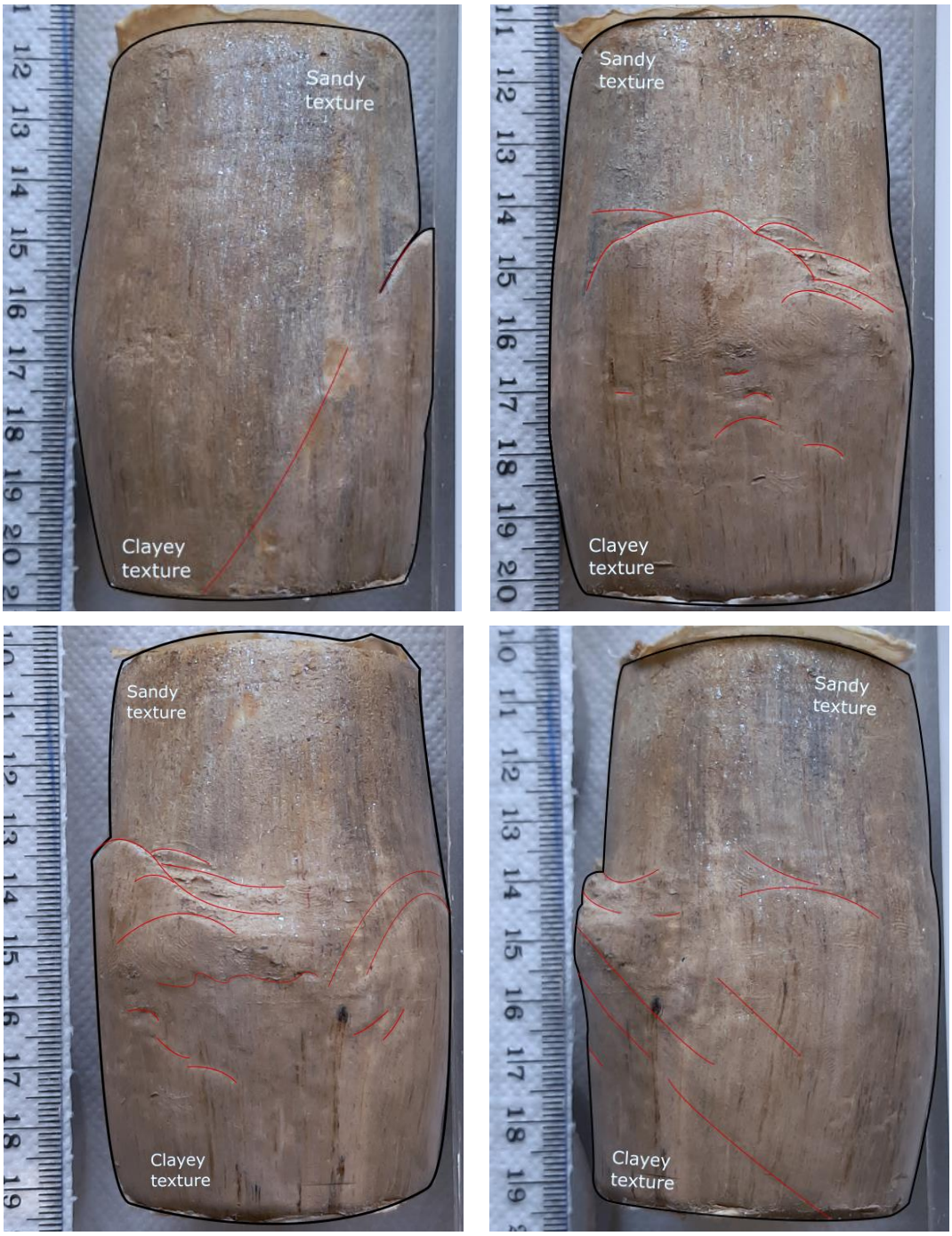

Figure 5.16 HCR3 Failed Triaxial core annotated figures. Tested at 150kPa under undrained, consolidated conditions.

Figure 5.17 expresses the failure mode of HCR7. As with the previous two samples, the sample barrelled (bulged) during testing. The failure mode identified is near ductile to ductile deformation (Selby, 1993). Same as the above two (HCR1, HCR3), the sample did not yield (**Figure 5.7**) the strain rising to 19.62 % before the test ended – however a crack (blue line) formed during the test. Opposite to this crack is silty material, which appears to have utilised the crack to dissipate pressure within the core.

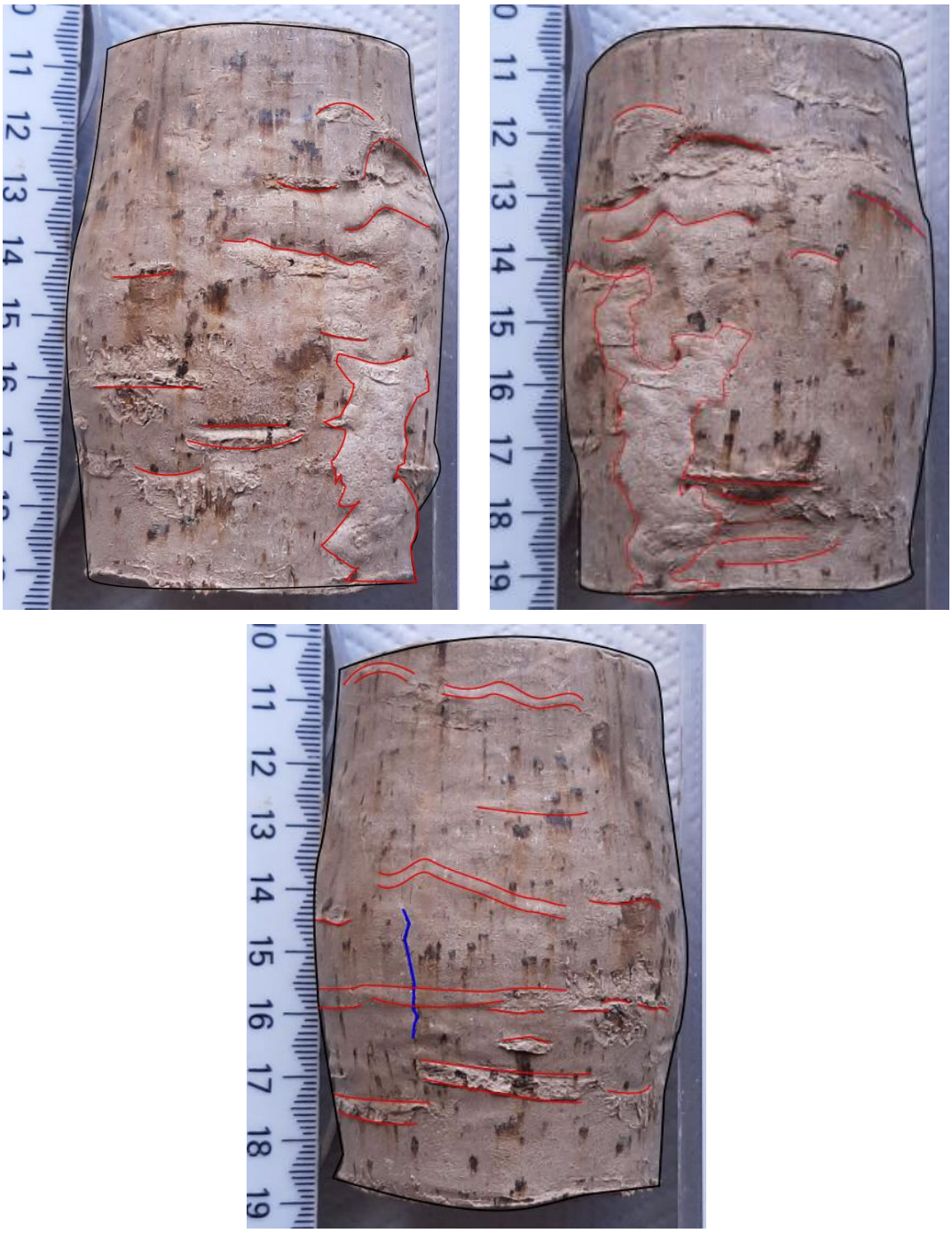

Figure 5.17 HCR7 Annotated failed triaxial core figures. Tested at 50 kPa under undrained, consolidated conditions.

5.8.1 Errors in Triaxial Testing

During collection, the push tubes were gently hammered into the soil. This resulted in compaction of the sample, consequently increasing soil strength slightly. On the other hand, the sampling process may have led to fractures within the sample, reducing soil strength. All samples were collected the same way so any increase in soil strength will occur for all samples ensuring the results will be as uniform as possible. To overcome the second point, samples were checked for any fractures or zones for weakness to propagate. Some of the samples presented fractures or other irregularities such as sand lenses or roots in the centre of the core, not observable until the cores were cut open and used. These substandard samples were used for other tests, or were discarded

5.9 Summary

Samples from the Rangitawa Tephra at the Hillcrest Road site are comprised of clay (39.59 ± 10.67 %), fine silt (silt: 33.73 ± 4.74 %), and very-fine sand total sand: 26.48 ± 15.11 %, very-fine sand: 10.67 ± 2.42 %, fine sand: 14.04 ± 5.94 %) fractions. Mineralogy identified in thin section petrography and bulk XRD included quartz, feldspars, biotite/muscovite mica, and clay minerals identified by XRD clay separates and SEM analyses were tubular and spheroidal forms of hydrated halloysite (10 Å), and in Atterberg limits analyses as dehydrated halloysite. The natural moisture content of the Rangitawa Tephra at Hillcrest Road is 34.41 %, above the PL (31 %) for the material inferring the material in the field would exhibit plastic properties. Static triaxial testing identified the material expresses ductile-plastic behaviour (Selby, 1993), fitting with the particle-size distributions of clay and silt, along with the identification of hydrated halloysite.

Table 5.9: Summary of all laboratory results

	Grain size fraction			Median grain-size		Atterberg Limits								XRD		XRF		SEM
Sample name	**Clay (%)**	**Silt (%)**	**Sand (%)**	**(μm)**	**Classification**	**NMC**	**PL (%)**	**LL (%)**	**PI**	**LI**	**Activity**	**Clay Mineralogy**	**Classification**	**Bulk**	**Fines**	**SiO_2 (%)**	**Al_2O_3 (%)**	
HCR1	43.72	32.95	23.33	5.55 ± 4.98	Very-fine silt									Quartz, sanidine, muscovite mica, kaolinite		50.63	30.22	
HCR3	18.99	26.66	54.35	82.8 ± 36.37	Very-fine sand									Quartz, sanidine, albite, muscovite mica, kaolinite		55.37	26.35	
HCR5 Bot	33.08	32.89	34.03	15.2 ± 1.96	Fine silt									Quartz, andesine, microcline, kaolinite		54.64	25.94	
HCR5 Top	17.77	35.31	20.56	5.18 ± 0.23	Very-fine silt	-	-	-	-	-	-	Dehydrated halloysite and/or kaolinite	ML: low compressibility silt	Quartz, sanidine, albite, muscovite mica, kaolinite	10 A Halloysite	53.12	27.64	Tubular and spheroidal halloysite
HCR6 Bot	44.13	26.12	56.11	89.3 ± 4.01	Very-fine sand									Quartz, sanidine, muscovite mica, kaolinite, halloysite, dickite		53.67	27.90	
HCR6 Top	24.83	23.58	51.59	70.7 ± 7.55	Very-fine sand									Quartz, sanidine, muscovite, kaolinite		48.45	29.19	
HCR7	35.87	34.5	29.63	10.6 ± 0.68	Fine silt									-		50.90	29.92	
HCR18	-	-	-	-	-									-		51.08	29.59	
Att. Paste 1	47.64	36.94	15.42	4.34 ± 0.27	Very-fine silt	35.72 35.72	32 32	46 46	14 14	0.26 0.25	0.29 0.29			-		-		
Att. Paste 2	43.31	36.29	20.4	5.41 ± 0.18	Very-fine silt	36.08	30	46	16	0.38	0.36			-		-		
Att. Paste 3	44.54	37.45	18.01	5.01 ± 0.10	Very-fine silt	32.26 32.26	30 30	44 45	14 18	0.14 0.1	0.31 0.40			-		-		
Average	39.59 ± 10.67	33.73 ± 4.74	26.48 ± 15.11	29.41 ± 34.14	Medium silt	34.41 ± 1.76	31 ± 0.98	45 ± 0.80	15 ± 1.60	0.23 ± 0.10	0.33 ± 0.04	Dehydrated halloysite and/or kaolinite	ML : low compressibility silt	-	10 A Halloysite	52.23 ± 2.34	28.35 ± 1.63	Tubular and spheroidal halloysite

Table 5.10 Summary of all laboratory results (continued).

	Triaxial shear										Petrography
Sample name	**Ultimate strain (%)**	**Ultimate Axial stress (kPa)**	**Pwp peak (kPa)**	**PWP end (kPa)**	**C (kPa)**	**c' (kPa)**	**Ø (°)**	**Ø' (°)**	**p' failure**	**q failure**	**Primary mineralogy**
HCR1	19.25	985.65	63	-7					228	122.8	
HCR3	19.32	1098.96	83	-48	17.2	11.2	29.7	40.5	368.5	179.5	Quartz, feldspar, mica, unidentified clay
HCR7	19.62	762.98	14	-28					160.1	81.5	
HCR18	-	-	-	-	-	-	-	-	-	-	
Average	-	-	-	-	17.2	11.2	29.7	40.5	-	-	Quartz, feldspar, mica, unidentified clay

Chapter 6
Discussion

6.1 Introduction

Literature relating to faulting and tectonic deformation in the Hamilton Basin is confined to a relatively short time period (since 2015), and to relatively few authors (de Lange *et al.*, 2015; Kleyburg, 2015; McKay, 2016; Campbell, 2017; Spinardi, 2017; Cave, 2020), all of whom belong to the University of Waikato. Thus, significant knowledge gaps exist. Initially it was assumed the only faults affecting the basin were those bounding and surrounding, with inactive ones deep beneath the basin fill in the greywacke basement rock (Spinardi *et al.*, 2017). The Hamilton Basin is filled with loose, soft sediments and soils, which makes observing and identifying faults difficult as deformation and offsets on any fault planes are not always the typical brittle fractures often expected of faults (Spinardi, 2017). As a result of this, more research into the way the materials may deform, such as their geomechanical properties, is required to indicate if inferred fault planes are indeed fault planes, and any deformation observed relative to these faults can be described by published mechanisms.This chapter presents the interpretations and discussions of the field observations from the cutting at 59 Hillcrest Road, and the laboratory analyses of the Rangitawa Tephra unit. This chapter will compare the findings with relevant published literature. These comparisons will attempt to add depth to results and draw field and laboratory results together to explain the processes and characteristics of tectonic deformation at the Hillcrest Road site, and provide inferences on the activity of the Rangitawa Tephra elsewhere.

6.2 Field Area

This site is believed to lie within close proximity of Te Tatua o Wairere fault zone which runs NE-SW through Rukuhia (Mystery Creek), Cobham Drive, Hillcrest, and out through Ruakura (shown in **Figure 2.6**)(de Lange and Moon, 2015) with various splinters identified along the trace. It is presumed fault splinters may be present along the ridgeline under Hillcrest Road, contained within the cutting. Hillcrest Road and other ridgelines aligned SW-NE are inferred uplifted fault blocks. (de Lange and Moon, 2015; Campbell, 2017; Spinardi, 2017; Spinardi *et al*., 2017; Moon *et al.,* 2019).

6.2.1 Stratigraphic correlations

Using relative dating such as stratigraphic correlations between absolute dated units e.g. The Rangitawa Tephra. Positions relative to each other and using colour/texture etc. (Burbank and Anderson, 2011; Kamp and Lowe, 1981; Lowe *et al.*, 2001; McCraw, 2011).

Typical simplified stratigraphic succession of the 'Hamilton Hills' throughout the Waikato Region as presented in Kamp and Lowe (1981).

Hamilton Ash Formation
Kauroa Ash Formation
Walton Subgroup — Karapiro Formation
Puketoka Formation

Referring to the descriptions of the materials expected within the Hamilton Hills as published by Kear and Schofield (1978), Kamp and Lowe (1981), Shepherd (1984), Lowe *et al.* (2001), Lowe (2010), and McCraw (2011). The unit and profile descriptions appear to fit perfectly.

6.2.2 Material Sensitivity

The Rangitawa Tephra at Hillcrest Road was insensitive based on shear vane measurements. Triaxial testing supports non-sensitive soils for the Rangitawa Tephra, as strain softening which is typical of sensitive soils was not observed (Kluger *et al.,* 2018). I could not find any literature presenting the sensitivity for the Rangitawa Tephra in the Hamilton Basin, therefore will assume the Rangitawa Tephra is not sensitive, as per my sensitivity measurements in the field.

6.3 Structural Information

The Hamilton Basin has not presented singular faults, rather complex zones. The presence of a fault trace indubitably indicates other fault strands in the same area.

Based on the Laws of Stratigraphy (Superposition and Original Horizontality) and according to Lowe (2019), the Rangitawa Tephra should be horizontal to sub-horizontal, following the slightly sloping erosional surface of the older Kauroa Ash

Formation. The orientation of the Rangitawa Tephra bed will vary considerably between outcrops, and within a site. This could suggest the bedding plane of the Rangitawa Tephra is the same as it would have been at deposition, thereby indicating little to no overturning of the unit at Hillcrest Road.

6.4 Deformation Structures

6.4.1 Offset Bedding

Any fault offset was not immediately obvious as thetypically expression of a faultas a brittle fracturing of materials and production of damage zones (Fossen, 2010) were not observed at the Hillcrest Road site. Rather than brittle-style fracturing, I hypothesise the material may exhibit ductile-style folding and will use the laboratory findings to consider this hypothesis.

The contact between the upper Kauroa Ash formation and lower Rangitawa Tephra is very uneven toward the northeast portion of the cutting. Contorted lobe structures of the lower Rangitawa Tephra were observed draping downward into the upper-Kauroa Ash Formation. These structures do not fit with the expected patterns of erosional structures, and rather may be formed by structural influences. The forms look similar to those illustrated in **Figures 2.4 and 2.5**, load casts, and/or large-scale loading structures resulting from gravity unstable density gradients triggered by earthquakes. Similar forms were identified in Tonkin (1970). Tonkin (1970) discusses the potential causes of these lobes, finally indicating the most likely cause is tectonic stresses. These contorted lobe structures were also present at the Kimbrae site near the Kukutaruhe Fault Zone in the northeastern Hamilton Basin (Spinardi, pers. comm, 2018). The majority of deformation observed in the cutting at Hillcrest Road appears to be within the Rangitawa Tephra, some of which is in the Hamilton Ash Formation above, and an apparent deformation of the white clay (Puketoka Formation) at the base. Deformation intensity and complexity (size and density) increases toward profile 3 in the northeast. It is hypothesised that the large offset in the Rangitawa Tephra (grey unit) near profile 3 **(Table 4.8 and Figure 4.11)** could potentially be a normal fault plane steeply dipping (60 - 70°) toward the northwest with 5.98 metre down-throw of the western side of the cutting, trending northeast-southwest **(Figures 6.2 and 6.3).** This deformation zone correlates with the deformed portion of the Walton Sub-group materials as the western portion of the Walton Subgroup – Puketoka Formation (white unit) appears to have been downthrown relative to the eastern side by approximately 6 metres **(Figure 6.3)**. The Walton Sub-group materials elsewhere (Kimbrae, Kay Road) appear to express brittle deformation in the form of fractures. There is little to no evidence for such deformation in the Walton

Sub-group units at the Hillcrest Road cutting. The discontinuity of a fault plane may provide a zone of weakness for weathering and erosional processes to exploit, thus masking the evidence of brittle fracture (Burbank and Anderson, 2011).
Over-thickening of the Hamilton Ash Formation units on the down-thrown side of the inferred fault plane further support the theory of a fault plane at this position. Tephra typically uniformly blankets an area, but the thicker units in the west, suggests the possibility the downthrown side could accumulate more tephra than the relatively upthrown side (Fossen, 2010).

All units also dip sharply and disappear into the base of the field area between profiles 4 and 5 (**Figure 4.2**) which could be inferred as another splinter off the fault zone resulting in further deformation and offset in the field area. This cannot be determined for certain, however, as the material exposed after the units disappear is fill from previous earthworks at the site so any other evidence of a fault in that particular area is masked and must be left under 'potential fault plane. Other normal faults are present across the Hamilton Basin. One example is the 8.4 metre and 3.04 metre displacements at Kay Road (Campbell, 2017). The deformation at Kay Road was believed to stop before the Rangitawa Tephra was deposited, constraining the activity on the fault to be older than 0.34 ka (Campbell, 2017). At Rototuna (in 2015), faults found dipped over a range 51 – 84°, with an average dip direction of 89°. At Kay Road steeply dipping faults were also identified, with an average dip of 57.3°, and an average dip of 73° and dip direction of 55° (northeast), aligned southwest-northeast (Moon *et al.*, 2019). Within the Hamilton Basin, reverse and strike-slip faults have also been suggested (Campbell, 2017; Spinardi, 2017) but there is no evidence in this site to suggest these forms of faulting are present.

The Rangitawa Tephra would need to exhibit plastic behaviour to suggest ductile-plastic deformation present as folding, to further support the presence of a fault plane in the cutting at Hillcrest Road. I will use the laboratory results of mineralogy and geomechanical behaviour to indicate this.

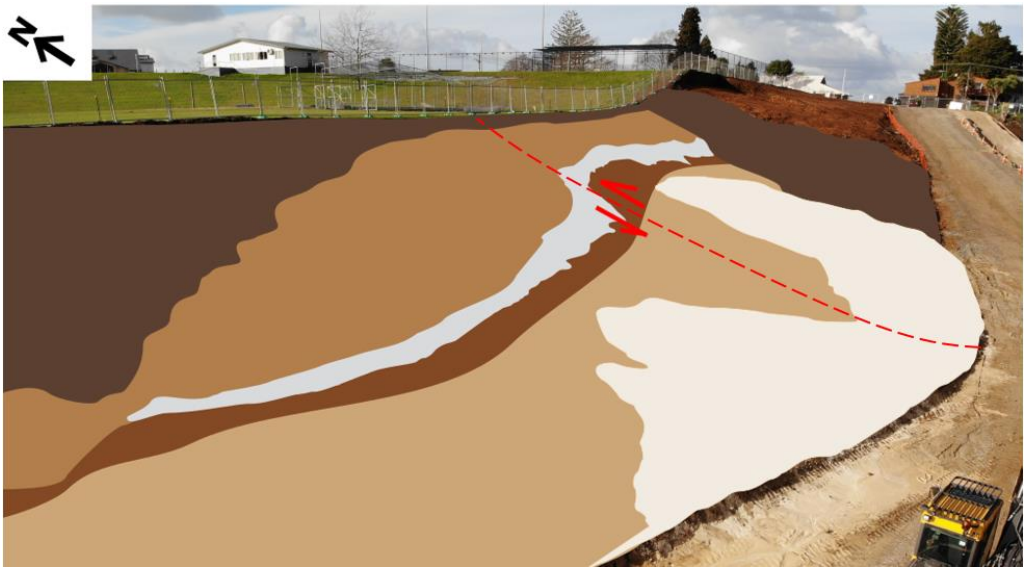

Figure 6.1: ***From Figure 4.5*** *Inkscape annotation of cutting presenting stratigraphic relationships at 59 Hillcrest Road, Hamilton with inferred fault (red) superimposed. Facing east-northeast.*

Figure 6.2 ***From Figure 4.11*** *Deformation at the base of the Rangitawa Tephra unit with inferred normal fault (red) superimposed.*

6.4.2 Intrusion Structures

The intrusion-like structures illustrated in **Figures 4.12 – 4.14** contain light grey silty-textured material, and/or dark-brown clayey-textured material. The source of the material was not identified in the field surveys, but I theorise the material could be a result of weathering processes or injection of material from within the site. Based on texture and colour characteristics I infer this material is injection of the Rangitawa Tephra into the lower Hamilton Ash Formation resulting from cyclic earthquake stressors. The dykes and sills must be younger than the material they are observed

within due to the stratigraphic law of cross-cutting relationships, suggesting the intrusions occurred shortly after deposition of the units they are present within, but before the next unit was deposited. The intrusion structures appear very similar to the clastic dykes illustrated in **Figure 2.4.** These formations are typically products of earthquakes or slumping or lateral spreading. There was no evidence for lateral spreading or slumping in the area, so by process of elimination I can safely assume these are the result of earthquake stressors. I will use the laboratory analyses to identify a valid explanation of the intrusion structures observed at Hillcrest Road.

6.5 Rangitawa Tephra

6.5.1 Mineralogy

The mineral assemblage identified in thin section petrography and XRD analyses were quartz, mica (biotite/muscovite), feldspars, and alumino-silicate clay mineral halloysite. In the bulk XRD analyses, halloysite was incorrectly identified as kaolinite. As kaolinite and halloysite are both 1:1 phyllo-silicate minerals of the same chemistry, this misidentification is easily explained. Kaolinite exists as a 1:1 alumino-silicate mineral with one sheet of each tetrahedral silica and octahedral alumina in a single mineral, providing a thickness of 0.7 nm (7 Å). Halloysite is also present as a 1:1 alumino-silicate mineral made up of tetrahedral silica and octahedral alumina layers; however, halloysite naturally exists with hydrogen-bonded interlayer water, which provides a natural thickness of 1.0 nm (10 Å). This structure is rigid yet halloysite readily dehydrates which leads to loss of the inter-layer water and collapse to 0.7 nm (7 Å), a very similar size to kaolinite. The exact clay mineralogy was determined by during the XRD clay separates analyses, which resulted in the identification of (10 Å) halloysite. SEM analyses also indicates spheroid and tubular forms of halloysite, where kaolinite typically exists as platy forms (Shepherd, 1984; Selby, 1993).

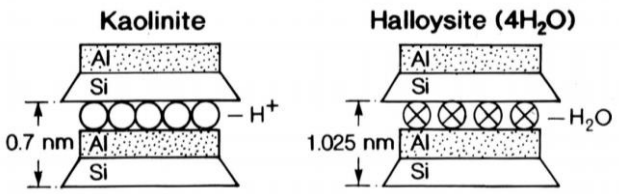

Figure 6.3: Kaolinite compared to halloysite. Figure source: Selby (1993).

6.5.2 Chemistry

The values derived from XRF testing on the Hillcrest Road Rangitawa Tephra samples and comparisons are presented in **Table 6.2**. Abundances of SiO_2 are lower than expected when compared with published literature while abundances of Al_2O_3 are higher than expected. Despite the Rangitawa Tephra being of rhyolite chemistry (Lowe *et al.,* 2001), the average SiO_2 content (52.23 ± 2.34 %) is significantly lower and the Al_2O_3 higher than typical chemistry of the fresh rhyolite rock (74.2 %). The high LOI values (12.60 ± 2.22 %) (fresh rock = LOI < 2.5%) suggest weathering and alteration of the raw tephra deposits, which could provide the reason for the lower than expected abundances of SiO_2, and high Al_2O_3. This is consistent with petrography, XRD, and SEM indications of abundant presence of the clay-mineral halloysite. The high Al_2O_3 content may have also reduced the relative contents of other minerals, such as the SiO_2 abundance, thereby providing another reason for the low expected abundances.

Table 6.1: Comparison of major element compositions from published literature on the Rangitawa Tephra, with an example of typical rhyolite chemistry, and Hillcrest Road samples. Comparison data from (Reference 1) Froggatt et al. (1986), Alloway et al. (1992), and Pillans, (1996) In: Horrocks (2000) and (Reference 2) Shepherd (1984). The symbol (-) indicates the chemistry was not measured.

Content (%)	Mt Curl Tephra[1]	Rangitawa Stream[1]	Omahina Road[1]	Welches Road - H1[2]	Rhyolite[2]	Rangitawa Tephra (Hillcrest Road)
SiO_2	78.09 ± 0.30	77.34 ± 0.28	78.03 ± 0.39	45.6	74.2	52.23 ± 2.34
Al_2O_3	12.33 ± 0.21	12.21 + 0.09	12.13 ± 0.14	32.4	13.3	28.35 ±1.63
TiO_2	0.14 ± 0.03	0.14 ± 0.04	0.15 ± 0.04	1.0	0.3	0.45 ± 0.06
MnO	-	-	-	0.1	0.05	0.04 ± 0.01
FeO (Fe_2O_3)	1.01 ± 0.08	1.04 ± 0.05	1.03 ± 0.06	9.3	1.8	3.95 ± 0.30
MgO	0.12 ± 0.02	0.12 ± 0.02	0.12 ± 0.02	5.4	0.3	0.33 ± 0.10
CaO	0.79 ± 0.04	0.82 ± 0.03	0.87 ± 0.06	3.1	1.6	0.24 ± 0.12
Na_2O	3.30 ± 0.16	3.59 ± 0.17	3.35 ± 0.22	-	-	0.66 ± 0.34
K_2O	4.33 ± 0.15	4.52 ± 0.16	4.22 ± 0.15	0.3	3.2	0.98 ± 0.53
P_2O_5	-	-	-	0.1	0.1	0.019 ± 0.001
SO_3	-	-	-	-	-	0.030 ± 0.01
CO_2	-	-	-	-	-	12.60 ± 2.22
SrO	-	-	-	-	-	39 ± 16
BaO	-	-	-	-	-	882 ± 307
Cl	-	0.22 ± 0.02	0.19 ± 0.04	-	-	-
H_2O	4.55 ± 1.25	5.92 ± 0.61	5.86 ± 1.14	-	-	-
n	132	10	32	1	25	8

In comparative references, the analyses were completed on glass shards (Reference 1), therefore the effect of clay mineralogy on the XRF results would be near nil, resulting in differing chemical proportions. Reference 2 (Shepherd, 1984) was completed on 'whole rock' samples providing a more reliable comparison to the chemistry published in this thesis.

6.5.3 Microstructure

The tubes and spheroids observed in SEM analyses **(Figures 5.6 a-f)** represent typical morphologies of halloysite (Shepherd, 1984; Selby, 1993; Joussein e*t al*., 2005). The tubes observed in the samples were ~ 500 nm with walls thicknesses of 5 – 10 nm. Tube lengths can range from 0.2 µm to >30 µm (Joussein *et al*., 2005) with an average wall thickness of approximately 3 nm (Selby, 1993). Small uneven-shaped spheroids ~200 nm were also present in the clay fraction, aggregating together to form clusters approximately 2 µm in size. Shepherd (1984) analysed the Rangitawa Tephra (H1) at Welches Road, indicating abundant long (0.4 – 0.9 µm) tubular and common large spheroid (~ 0.4 µm) forms of halloysite, which supports the findings from the SEM analyses in this project.

6.5.4 Particle-Size

Particle size analysis showed that the highest proportion of the material was in the clay fraction, followed by silt, and then sand (see **Tables 5.9** and **5.10** for values) with a bimodal average of very-fine silt and very-fine sand at a total average of medium silt. The Rangitawa Tephra in the field was identified to have a clayey SILT texture, but perhaps should have been silty CLAY. Variation between samples are likely due to variations within the Rangitawa Tephra deposit. The unit at Hillcrest Road is stratified with clayey silts and silty sands presumably resulting from eruption evolution during deposition. The top of the Rangitawa Tephra appeared to have a significant portion of very-fine sand-sized mica relative to the lower portion of the unit – for this reason the HCR3, HCR5 top and HCR6 top have a median size classification of very fine sand, whereas the rest classify as fine to very fine silts. The Rangitawa Tephra (H1) in Shepherd (1984) had 59% clay, 24 % silt, and 17% sand proportions. The variation between these results and mine most likely result from aggregated clays being measured as silts and sands in my samples, or normal intra-unit variations. Particle-size components relate directly to depositional material particle-size with geological evolution by modification from weathering and soil forming processes (Selby, 1993). High clay content relative to sand proportion provides evidence for highly weathered rhyolite pyroclastic fall materials. High clay and silt contents suggest weathered in-situ pyroclastic tephra (Selby, 1993).

6.5.5 Atterberg Limits

The sample taken from the Rangitawa Tephra at Hillcrest Road is a low compressibility silt mixed with either kaolinite or halloysite (dehydrated/hydrated) clay minerals. Selby (1993) contains a table with the expected values from Atterberg tests for common clay minerals. **Table 6.2** below suggests that using SEM analyses the materials were defined to be of halloysite morphology, thereby resulting in the suggestion that the Rangitawa Tephra contains halloysite in both hydrated and dehydrated forms.

Table 6.2 Properties of clay minerals. Adapted from Selby (1993).

	My samples	Hydrated halloysite	Dehydrated halloysite	Kaolinite
Particle thickness	5 – 10 tubular wall thickness	Tubular wall = 3	Tubular wall = 3	30 – 100
LL %	44 – 46	50 – 70	30 - 55	30 -110
PL %	30 – 32	47 – 60	30 – 45	25 – 40
Activity	0.29 – 0.40	0.10 – 0.40	0.50	0.30 – 0.50

Table 6.3 Atterberg limit indices adapted from Briaud (2013).

Parameter	Low	Medium	High
LL	10 – 40	40 – 80	> 80
PL	10 – 20	20 – 30	> 30
PI	0 – 20	20 – 50	> 50

Samples from the Rangitawa Tephra at Hillcrest Road express a combination of properties typical of rhyolite tephra-derived soils such as high plastic and liquid limits, low activity, high natural moisture contents, and plotting below the line in the A-line classification chart. These results are correlated to dominant clay mineralogy of hydrated halloysite in many cases (Jacquet, 1990 via Mills, 2016). **Figure 6.4** illustrates a plasticity chart with results of rhyolite tephra. The figure was taken directly from Mills (2016) with the average PI and LL from this study plotted as a comparison. The material is moderately sticky and highly plastic **(according to Table 6.3)** suggesting the clay fraction has developed due to weathering over time. Literature proposes halloysite and allophane in the Hamilton Ash sequence (Kamp and Lowe, 1981; Selby and Lowe, 1992; Lowe *et al.,* 2001). These findings suggest halloysite is present in the Rangitawa Tephra unit, therefore supported by the literature. Mineralogy analyses also support the claim that halloysite is present with the Rangitawa Tephra samples at Hillcrest Road, although suggesting the halloysite may be hydrated in the field rather than dehydrated.

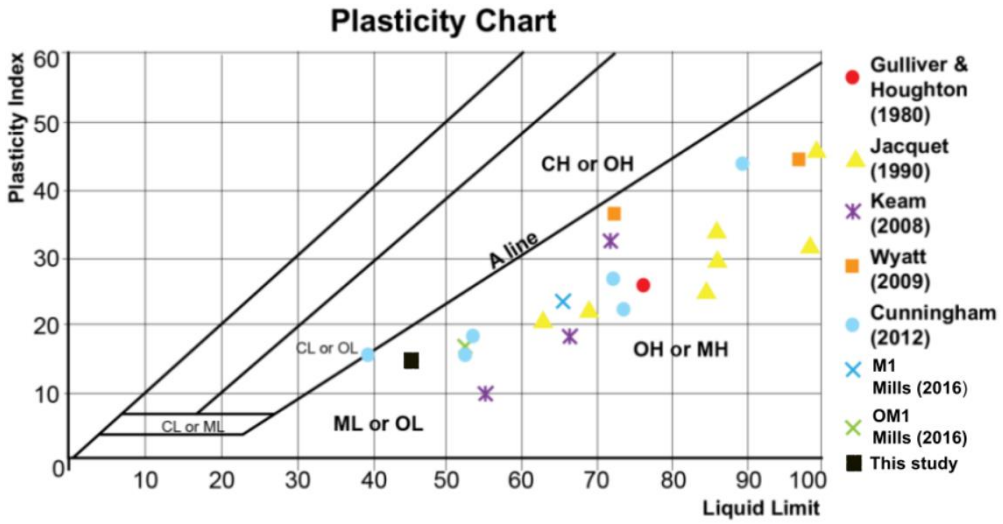

Figure 6.4 A-line chart illustrating a range of samples of rhyolite chemistry. Figure taken directly from Mills (2016) and adapted to include results from this study.

6.5.6 Triaxial shear strength

The Rangitawa Tephra samples from Hillcrest Road have been classified as dilatant. Dilative failure mechanisms are characterised by stress-strain curves with peaks above 15-20 % strain, and p'-q graphs that trend right along the critical state line post-failure together with pore pressure curves that result in negative pore water pressure, and post-failure specimens that express barrel to intermediate failure types **(Figure 6.5)**(Selby, 1993; Mills, 2016).

Normally consolidated, soft, and loose soils typically do not exhibit peaks in the stress-strain graphs, rather the strain increases gradually until reaching critical state. Over-consolidated, hard, or dense soils, by comparison, exhibit stress-strain peaks followed by a drop in stress typically known as strain softening **(Figure 6.5)** (Briaud, 2013). The over-consolidated sands suggested by the p'-q plots contradicts the normally consolidated soils suggested by the stress-strain graph. Particle-size analyses suggest the Rangitawa Tephra samples from Hillcrest Road do not contain significant proportions of the sand size fraction relative to the clay and silt fractions which suggest the p'-q plot may express error of some sort. The Rangitawa Tephra, thus, is considered a normally consolidated soil. Selby (1993) and Briaud (2013) state soft, normally consolidated, and loose soils are treated as elasto-plastic materials and exhibit ductile-plastic failure where peak deviator stress is reached at 15-20 %. Burbank and Anderson (2011) state that if a material does not rupture post-yield, the material deforms plastically. Plastic deformation is the result of irreversible

sliding of particles, especially of hydrated clay minerals (Selby, 1993). As halloysite is inferred to be hydrated in the field, I consider this the case in the Rangitawa Tephra, where the hydrated halloysite clay minerals slide next to each other, allowing plastic-style deformation.

The Rangitawa Tephra displayed total and effective friction angle and cohesion values of 29.7˚, 40.5˚ and cohesion values of 17.2 and 11.2 kPa respectively. The values presented in Selby (1993) for halloysite clay minerals suggest effective friction angles of 25-35°, the Swiss Standard (SN 670 010b) (~ 10 kPa cohesion, and 23-33° friction angle) for high plasticity silts. At similar PI (~15 %) effective friction angles in halloysite-rich materials is approximately 30° (Kluger *et al.,* 2018).
The material, therefore, is confirmed to be silt of high plasticity with significant clay fraction of halloysite clay minerals. The values calculated for The Hillcrest Rangitawa Tephra are somewhat higher than the other published values, potentially due to a higher proportion of sand which raises the friction angle, and larger clay influence (than other samples) resulting in a higher cohesion value than the published values. This difference could also be explained by lower than expected Atterberg limits due to partial dehydration of the samples during sampling, storage, and testing. The differences may also be accounted for when considering the varying proportions of particle-size fractions within each sample. With a high natural water content, the PI may have increased and the relationship between PI and effective friction angle may then fit with the halloysite-rich samples in Kluger *et al.* (2018). The high effective friction angle calculated in the Rangitawa Tephra samples might be explained by particle realignment during shear and complex interactions between the two different morphologies (tubular and spheroidal) present, leading to significant effect of asperities (Kluger *et al.,* 2018).

The specimens were tested in this project under static triaxial pressures modelling the effects of simple overburden stresses, but does not provide specimen reaction to earthquake loading which is important for indication of the geomechanical properties of the Rangitawa Tephra under earthquake (cyclic) stress. To support the theory that the Rangitawa Tephra exhibits plastic deformation and may liquefy under cyclic stress; the material should be tested under cyclic triaxial conditions in addition to static conditions.

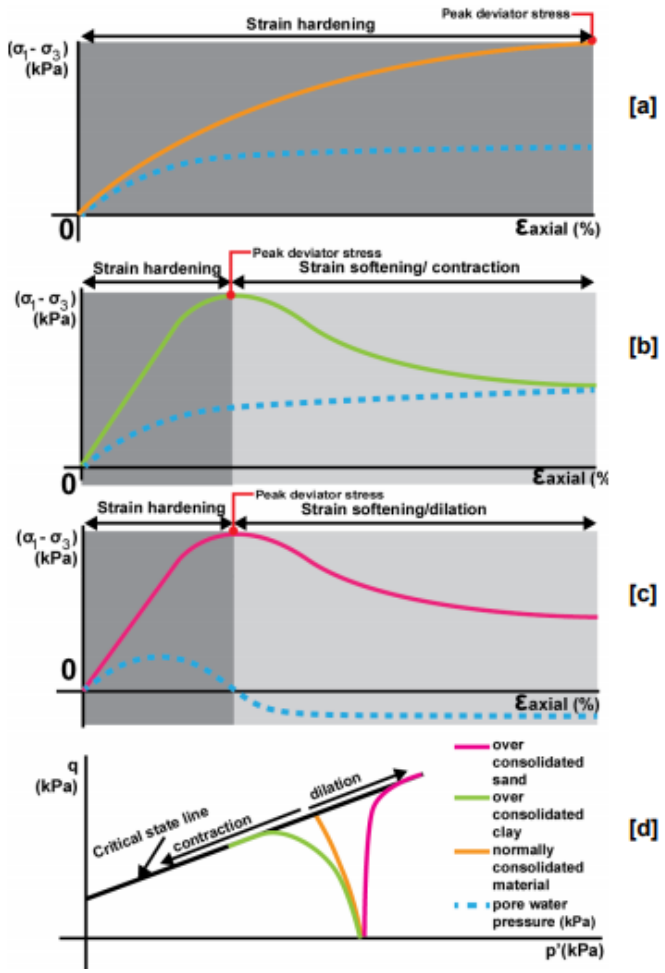

Figure 6.5 Different behaviours expected for over consolidated sand, overconsolidated clays, and normally consolidated material for both q' (deviator stress) vs εaxial, and q vs p' (effective stress). Schematics adapted from Boulanger and Idriss (2006) and Briaud (2013) via Mills, (2016).

6.5.7 Potential for Soft-Sediment Deformation

Liquefaction susceptibility is typically observed in materials of coarse silt to fine-medium sand textures (Selby, 1993; Owen and Moretti, 2011; Kluger *et al.,* 2018). The Rangitawa Tephra at Hillcrest Road has mean particle-sizes of very-fine silt and very-fine sands, with an average of medium silt sized particles. Thus, the Rangitawa Tephra does not fit the classical susceptibility to liquefy under cyclic stress (reference). Liquefaction structures have been observed in materials not perfectly fitting this criteria, however, suggesting under certain circumstances, materials not typically expected to liquefy may exhibit liquefaction-style structures. Boulanger and Idriss (2006) provide one example of such where soils of clay-dominated behaviour exhibited liquefaction following the 1999 earthquake in Adapazari (Bray *et al.*, 2004 In: Boulanger and Idriss, 2006). Boulanger and Idriss (2006) published a document titled "Liquefaction Susceptibility Criteria for Silts and Clays" detailing the capability

to indicate fine-grained materials, which may be susceptible to liquefy/exhibit cyclic softening, based on their Atterberg limits. Boulanger and Idriss (2006) present three scenarios for fine-grained liquefaction/cyclic softening susceptibility; A – susceptible to cyclic-induced liquefaction/cyclic softening, B – potential to liquefy/ exhibit cyclic softening, and C – not classically susceptible. Criteria for these scenarios are presented in **Table 6.4**. The Atterberg Limits from the Rangitawa Tephra samples almost fit within the criteria for B – potentially liquefiable fine-grained soils. The LL must be less than 47 %, PI less than 20 %, and ratio of water content (Wc) to LL must be more than 0.85. The Rangitawa Tephra samples expressed an average of LL: 45 %, PI: 15 %, and Wc:LL of 0.77, consequently fitting all criteria except the Wc:LL ratio where the Rangitawa Tephra samples do not exhibit sufficient water contents. Wc less than 0.8 are systematically more resistant to liquefaction/ cyclic softening, but with an increase in Wc in the case of shallow water tables or other saturation events, the material may be still be susceptible to cyclic-induced mobility (Boulanger and Idriss, 2006). As the Rangitawa Tephra dried and dehydrated slightly during sample collection, storage, and laboratory testing, the Rangitawa Tephra should have a slightly higher natural moisture content, and therefore higher Wc:LL ratio. The Rangitawa Tephra from Hillcrest Road has also undergone weathering processes, which would have increased the relative clay content by dissolution of minerals, together with pedogenesis (Shepherd, 1984; Lowe *et al.,* 2001). With a larger fraction of silts and sands, this would likely decrease the LL % and PI %, thereby the Rangitawa Tephra could once have fit criteria A – susceptible to classic cyclic-induced liquefaction/ cyclic softening. I infer based off these findings that the Rangitawa Tephra at Hillcrest could express cyclic softening under earthquakes stressors, which provides an explanation for the dike and sill intrusion structures identified in profiles 2 and 3. *In-situ* testing of material, along with cyclic triaxial analyses would support this theory.

Table 6.4: Susceptibility of fine-grained soils to liquefy under cyclic (earthquake) stress based on Atterberg limits (LL %, PI %, Water content (Wc): LL ratio). Table produced from Boulanger and Idriss (2006), with comparison to Hillcrest Road Rangitawa Tephra Atterberg limits averages.

Criteria	LL %	PI %	Wc / LL	Susceptibility
A	< 38	< 13	> 0.80	Susceptible to classic cyclic-induced liquefaction/ softening
B	38 – 47	13 – 20	> 0.85	Potential to liquefy/ cyclic soften.
C	> 47	> 20	-	Not classically susceptible
Rangitawa Tephra (Hillcrest Road)	45	15	0.77	Inferred: Potential to liquefy/ exhibit cyclic softening (with increased Wc)

6.6 Summary

Stratigraphic correlations and profile descriptions were supported by published literature. Due to non-invasive techniques of investigation applied at this site (Hillcrest Road), faulting could not be confirmed definitively. Evidence suggests tectonic deformation is present and therefore fault movement may have been present in the past, if not also expected in future. Even if the area has been/is tectonically active, the activity/deformation is not extensive or extreme thereby suggesting relatively low seismic effect here. Employed laboratory tests and analyses to support the findings in the field area for the Rangitawa Tephra and explain the deformation structures observed at Hillcrest Road.

The advanced weathering and alteration occurring from diagenesis, and pedological processes since deposition (340 kya) can explain the Rangitawa Tephra mineralogical, chemical, particle-size and microstructural observations, and geochemical characteristics. Advanced weathering of the Rangitawa Tephra unit is supported by the high clay content and prevalence of resistant primary minerals of quartz, feldspars, along with the loss of Si and increase of Al, Ti, and Fe during clay mineral formation.

Faulting is supported by the field observations where the displacement across the Rangitawa Tephra unit correlates with the apparent displacement and significant erosional structural observed within the (white) Walton Subgroup units. The displacement in the Rangitawa Tephra unit was observed to deform in a ductile-plastic fashion. The laboratory analyses suggested the Rangitawa Tephra expressed ductile-plastic deformation, which supports this theory, proving the presence of a fault plane within the exposure at Hillcrest Road.

The soft sediment deformation structures of contorted lobes along the base of the Rangitawa Tephra unit and the intrusion structures observed injected upwards into the Hamilton Ash Formation was theorised to be the result of structural influences rather than erosional. This theory was supported by comparison of laboratory analyses to published literature. Published literature (Boulanger and Idriss, 2006; Kluger *et al.,* 2018) proposed materials of very similar characteristics as the Rangitawa Tephra at Hillcrest Road may exhibit the potential to liquefy/cyclic soften. The soft sediment deformation structures, therefore, can be explained as folding and bending due to shaking, and injection of dykes and sills resulting from cyclic stressors.

Chapter 7
Conclusion

7.1 Summary of Key Objectives

The aims defined in chapter 1 were to characterise stratigraphy and materials at the Hillcrest Road site to determine whether or not deformation features indicating seismic activity are present. In particular, to characterise the Rangitawa Tephra unit in terms of mechanical behaviour.

In addressing objective 1) A typical stratigraphic sequence was found, with the Walton Subgroup at the base, followed by an erosional unconformity and the Kauroa Ash Formation. After another erosional conformity is the Hamilton Ash Formation with the key stratigraphic unit Rangitawa Tephra at the base. Above these units in the field is a sequence of disturbed fill materials. 2) Deformation structures within the Rangitawa Tephra unit, and elsewhere in the exposure were identified and described based on geometry, orientation, dimensions, texture, and colour. The features were then analysed relative to the laboratory properties in order to indicate the potential deformation processes, especially to indicate whether or not the deformation was caused by tectonic and seismic influences.

Objectives 3) and 4) During the field analyses, the Rangitawa Tephra was identified as a key unit for the research as it expressed significant deformation structures clearly. The unit was described and the material samples for laboratory analyses to characterise the key mineralogical, chemical, and geomechanical properties.

The Rangitawa Tephra has a particle-size distribution averaging at very-fine silt, and very-fine sands, with an overall average of medium silt. The clay fraction contained the highest proportions within the Rangitawa Tephra, followed by silt, then sand.

The mineralogy identified during thin section petrography and XRD analyses were an assemblage in the sand and silt fractions of quartz, feldspars and mica (biotite/muscovite), and in the silt and clay fractions was hydrated and dehydrated halloysite. SEM analyses indicated nanotubular and spheroidal forms of halloysite were present.

Atterberg limits analyses indicated the Rangitawa Tephra at Hillcrest Road was an inactive (0.33) silt of low compressibility (ML), with medium-range liquid limit (45%), high plastic limit (31%), and low plasticity index (15%), at an average natural moisture content of 34.41%. These values correlated to an inferred mineralogy of

dehydrated/hydrated halloysite, which was supported by XRD (fines) and SEM analyses.

Triaxial shear strength testing indicated the Rangitawa Tephra is a dilatant material and the samples did not rupture post-yield therefore indicates the material is of normally consolidated state, thereby treated as an elasto-plastic material that would exhibit ductile-plastic failure upon applied stress. The post-testing specimens also exhibited ductile-plastic deformation in the form of barrelling.

The analyses resulting in cohesion and effective cohesion values of 17.2 kPa and 11.2 kPa, and friction angle and effective friction angles of 29.7° and 40.5° respectively. These values indicate the material acts as high plasticity silt and correlates with halloysite-rich tephra of similar plasticity indexes, with some extra influence from the clay and sand fractions within the samples.

Key structures identified were large displacements in the Walton Subgroup and Rangitawa Tephra units, contorted lobe forms, and dykes and sills penetrating upwards. The significant (5.98 metre) displacement observed in the Rangitawa Tephra and Walton Subgroup units which was later determined to be a steeply dipping normal fault plane deforming the units in the field. The deformation did not express the typical brittle failure as expected along fault planes, but laboratory analyses identified the Rangitawa Tephra exhibits a ductile-plastic deformation style, which likely masked the brittle deformation by folding of the Rangitawa Tephra unit rather than fracturing along the inferred fault plane.

Contorted lobe forms were identified during field analyses at the base of the Rangitawa Tephra penetrating downwards into the upper Kauroa Ash Formation. These were determined to be result of either erosional or structural influences, but due to the shape of the lobes it was determined these were more likely soft sediment deformation structures. Later interpretations indicated the forms most closely fit contorted lamination deformation structures resulting from seismic stressors in the area. Within the Hamilton Ash Formation (units H3/H4 and H4/H5), thin dykes and sills of light grey silty material were observed. The source of the material could not be identified in the field but it was suggested the material could be a product of weathering and alteration, or injection of material within the site. It was determined based on the texture and colour; the structures were likely penetration of the Rangitawa Tephra upwards resulting from cyclic seismic stress within the area. Laboratory analyses and comparisons with literature suggested the Rangitawa Tephra, based on particle-size, Atterberg Limits, and triaxial shear strength analyses, could deform due to seismic stress, expressing cyclic softening and viscous-flow to

reduce pore water pressures (similar to liquefaction, but in clays). This supports the theory of injected Rangitawa Tephra upwards into the Hamilton Ash Formation. Based on the Law of Cross-cutting relationships, the dike and sill structures indicate the relative age of the most recent deformation at the Hillcrest Road. The unit in which the structures were present within would be older than the forms, while the material above is presumed older. Thus, the injectite forms must be younger than/similar age to H5 (c. 290–250 ka) but older than H4 (c. 240-190 ka) (Lowe *et al.,* 2001).

In summary, field analyses and laboratory analyses together confirm the presence of a steeply dipping normal fault present with ~ 6m displacement as ductile-plastic bending of the Rangitawa Tephra unit, and the fault plane in the Walton Subgroup masked by the large erosional structure observed in the white clays. Related soft sediment deformation forms of contorted bedding along the Rangitawa Tephra, and dykes and sills injected upwards in the Hamilton Ash Formation (H3/H4) from the Rangitawa Tephra, are indicated to be the result of cyclic stresses at the site, potentially during displacement on the fault plane within the same exposure.

7.2 Opportunities for future research

Suggestions to further support this research are included below;

1) Test the Rangitawa Tephra unit with cyclic triaxial shear strength testing to indicate and confirm the Rangitawa Tephra exhibits cyclic softening under cyclic stress;
2) Test intrusion structures within the Hamilton Ash Formation and compare the material to the Rangitawa Tephra to confirm the theory the structures are injection of the Rangitawa Tephra under cyclic stress;
3) Characterise and study the Rangitawa Tephra at more sites to indicate whether the Rangitawa Tephra strains by ductile-plastic deformation. This could suggest the other faults identified across the basin are younger than initially presumed.

References

Allen, J.R.L., 1982. Sedimentary structures: their character and physical basis. Vol. II. Elsevier, New York (663 pp.).

Boulanger, R. W. & Idriss, I. (2006). Liquefaction susceptibility criteria for silts and clays. J. Geotech. Geoenvironmental Engineering 132 (11), pp. 1413–1426.

Briggs, R., Houghton, B., McWilliams, M. & Wilson, C. (2005). 40Ar/39Ar ages of silicic volcanic rocks in the Tauranga-Kaimai area, New Zealand: dating the transition between volcanism in the Coromandel Arc and the Taupo Volcanic Zone. New Zealand J. Geol. Geophys. 48 (3), pp. 459–469.

Briggs, R.M., Itaya, T., Lowe, D.J., Keane, A.J. (1989). Ages of the Pliocene-Pleistocene Alexandra and Ngatutura Volcanics, western North Island, New Zealand, and some geological implications. New Zealand Journal of Geology and Geophysics 32, pp. 417-427.

Burbank, D. W., & Anderson, R. S. (2011). Tectonic geomorphology. John Wiley & Sons.

Campbell, B.R. (2017). Hamilton's Hidden Hazard: The Characterisation and Mapping of Zones of Tectonic Deformation within the Hamilton Basin. MSc thesis. School of Science, University of Waikato.

Campbell, D. J. 1975. Liquid limit determination of arable topsoils using a dropcone penetrometer. J. Soil Sci. 26, 234–40.

de Lange, P. J., Lowe D. J. (1990). History of vertical displacement of Kerepehi Fault and Kopouatai bog, Hauraki Lowlands, New Zealand, since c. 10,700 years ago. Journal of Geology and Geophysics, 33:2, pp. 277-283. DOI:10.1080/00288306.1990.1042685

de Lange, W., Moon, V.G., Lowe, D.J. (2015). Hidden faults in the Hamilton Basin. Geosciences 2015, Wellington, New Zealand. Geoscience Society of New Zealand Miscellaneous Publication 143a, pp. 29.

Edbrooke, S.W. (compiler) (2005). Geology of the Waikato area. Institute of Geological and Nuclear Sciences 1: 250,000 map 4. Institute of Geological and Nuclear Sciences, Lower Hutt. 1 sheet + 68 pp.

Froggatt, P.C. (1983). Toward a Comprehensive Upper Quaternary Tephra and Ignimbrite Stratigraphy in New Zealand Using Electron Microprobe Analysis of Glass Shards. Quaternary Research, 1983, Vol 19(2), pp. 188-200. Elsevier. https://doi-org.ezproxy.waikato.ac.nz/10.1016/0033-5894(83)90004-2

GNS. (2017). When is a Fault "Active". Retrieved September 11, 2017, from https://www.gns.cri.nz/Home/Learning/Science-Topics/Earthquakes/Earthquakes-and-Faults/When-is-a-Fault-Active.

Horrocks, J.L. (2000). Stratigraphy, chronology and correlation of the Plio-Pleistocene (c. 2.2–0.8 Ma) Kauroa Ash sequence, western North Island, New Zealand. Unpublished PhD thesis, University of Waikato, Hamilton.

Jacquet, D. (1990). Sensitivity to remoulding of some volcanic ash soils in New Zealand. Engineering Geology. 28 (1–2), pp. 1–25.

Joussein, E., Petit, S., Churchman, J., Theng, B., Righi, D. & Delvaux, B. (2005). Halloysite clay minerals – a review. Clay Minerals. 40 (4), pp. 383–426.

Kamp, P. J. J., & Lowe, D. J. (1981) Quaternary stratigraphy, landscape, and soils of the Hamilton Basin. In R. M. Briggs (Ed.), Geological Society of New Zealand 1981 Conference, Hamilton (pp. 14 - 28).

Kear, D., Schofield, J.C. (1978). Geology of the Ngaruawahia Subdivision. New Zealand Geological Survey Bulletin 88. 168 pp.

Kleyburg, M. A. (2015). Paleoliquefaction in Late Pleistocene alluvial sediments in the Hauraki and Hamilton basins. Masters thesis, University of Waikato, Hamilton, New Zealand.

Kluger, M.O., Kreiter, S., Moon, V.G., Orense, R.P., Mills, P.R. Morz, T. (2018). Undrained cyclic shear behaviour of weathered tephra. Géotechnique 69 (6). pp 489-500. https://doi.org/10.1680/jgeot.17.P.083

Kohn, B. P., Pillans, B., & McGlone, M. S. (1992). Zircon fission track age for middle Pleistocene Rangitawa Tephra, New Zealand: stratigraphic and paleoclimatic significance. Palaeogeography, Palaeoclimatology, Palaeoecology, 95(1), 73-94.

Lowe, D. J. (2000). Upbuilding pedogenesis in multisequal tephra-derived soils in the Waikato region.

Lowe, D. J. (2011). Tephrochronology and its application: a review. Quaternary Geochronology 6 (2), pp. 107–153.

Lowe, D.J. (2010). Introduction to the landscapes and soils of the Hamilton Basin. In: Lowe, D.J.; Neall, V.E., Hedley, M; Clothier, B.; Mackay, A. 2010. Guidebook for Pre-conference North Island, New Zealand “Volcanoes to Oceans” field tour (27-30 July). 19th World Soils Congress, International Union of Soil Sciences, Brisbane. Soil and Earth Sciences Occasional Publication No. 3, Massey University, Palmerston North, pp. 1.24-1.61.

Lowe, D.J. (2019). Using soil stratigraphy and tephrochronology to understand the origin, age, and classification of a unique Late Quaternary tephra-derived Ultisol in Aotearoa New Zealand. Quaternary 2 (1), pp. 9. (https://doi.org/10.3390/quat2010009).

Lowe, D.J., Tippett, J. M., Kamp, P.J.J., Liddell, I.J., Briggs, R.M., Horrocks, J.L. (2001). Ages on weathered Plio-Pleistocene tephra sequences, western North Island. New Zealand. In: Juvigné, E. T., Raynal, J. P. (Eds), Tephras: Chronology, Archaeology, CDERAD éditeur, Goudet. Les Dossiers de l’Archéo-Logis 1: 45-60.

McCraw, J. (2011) The wandering river: Landforms and geological history of the Hamilton Basin (Guidebook (Geoscience Society of New Zealand); no. 16). Lower, Hutt, N.Z.: Geoscience Society of New Zealand.

McKay, A. (2017). Evaluationg soil and landscape models to predict liquefaction susceptibility in the Hinuera Formation, Hamitlon Basin MSc thesis, The University of Waikato, Hamilton, New Zealand.

Mills, P.R., (2016). Failure mechanisms in sensitive volcanic soils in the Tauranga Region, New Zealand. MSc thesis. School of Science, University of Waikato.

Milne, J. D. G.; Clayden, B.; Singleton, P. L.; Wilson, A. D. (1994). Soil Description Handbook. Revised edition. First edition published: Lower Hutt, N.Z.: DSIR Land Resources, 1991. Manaaki Whenua Press.

Moon, V. G., & de Lange, W. P. (2017). Final Report on EQC Potential shallow seismic sources in the Hamilton Basin. Retrieved September 6

Moon, V., de Lange W., Cummins M. (2016/7). Movement of hidden faults within the Hamilton Basin. School of Science, University of Waikato.

Moon, V.G., Spinardi, F. (2019). Hamilton Basin faults. In: Lowe, D.J., Pittari, A. (2020). Field Trip Guides. Geosciences 2019 Conference, Hamilton, New Zealand (24-29 November). Geoscience Society of New Zealand Miscellaneous Publication 155B, pp. 1−15.

Moretti, M., van Loon A. J. (2014). Restrictions to the application of ‘diagnostic’ criteria for recognizing ancient seismites. Palaeoseismology and seismites: Journal of Palaeogeography 3(2), pp. 162-173. DOI: 10.3724/SP.J.1261.2014.00050

NZGS (New Zealand Geotechnical Society) (2001). Guideline for hand held shear vane tests. Wellington, New Zealand: New Zealand Geotechnical Society.

NZGS. (2017). Field description of soil and rock - field sheet. Retrieved January 11, 2017, from http://www.nzgs.org/library/field-description-of-soil-and-rock-field-sheet/.

Obermeier, S. F., Jacobson, R. B., Smoot, J. P., Weems, R. E., Gohn, G. S., Powars, D. S., & Monroe, J. E. (1990). Earthquake-induced liquefaction features in the coastal setting of South Carolina and in the fluvial setting of the New Madrid Seismic Zone. United States Geological Survey, Professional Paper; (USA), Medium: X; Size: Pages: 1-44.

Owen G., Moretti M. (2014). Identifying triggers for liquefaction-induced soft-sediment deformation in sands. Sedimentary Geology 235, pp. 141-147. Elsevier B.V.

Owen G., Moretti M., Alfaro P. (2011). Recognising triggers for soft-sediment deformation: Current understanding and future directions. Sedimentary Geology 235, pp. 135-140. Elsevier B.V.

Pillans, B.J., Kohn, B.P., Berger, G.W., Froggatt, P.C., Duller, G., Alloway, B.V., Hesse, P. (1996). Multi-method dating comparison for mid-Pleistocene Rangitawa Tephra, New Zealand. Quaternary Science Reviews 15, 1-14.

Selby, M.J. (1993). Hillslope Materials and Processes, 2nd Ed, Oxford University Press. Oxford.

Selby, M.J. and Lowe, D.J. (1992). The middle Waikato basin and hills, In: J.M. Soons and M.J. Selby (eds), Landforms of New Zealand, 2nd ed., Longman Paul, Auckland, pp. 233-255.

Shepherd, T.G. (1984). A Pedological Study of the Hamilton Ash Group at Welches Road, Mangawara, North Waikato. MSc thesis, The University of Waikato, Hamilton, New Zealand.

Spinardi, F. (2017). Preliminary evaluation of tectonic geomorphological signals in the Hamilton Basin (In Progress). MSc thesis, The University of Waikato, Hamilton, New Zealand.

Spinardi, F., Campbell, B., Moon, D. V., Pittari, A., Fox, B. R. S., & de Lange, W. P. (2017). Unravelling Fault Structures of the Hamilton Basin. Proc. 20th NZGS Geotechnical Symposium.

Suter, F., et al. (2011) Holocene soft-sediment deformation of the Santa Fe–Sopetrán Basin, northern Colombian Andes: Evidence for Hispanic seismic activity? Sediment. Geol. doi:10.1016/j.sedgeo.2010.09.018

Swiss Standard SN 670 010b, Characteristic Coefficients of soils, Association of Swiss Road and Traffic Engineers

Tonkin, P.J. (1970). Contorted stratification with clay lobes in volcanic ash beds, Raglan-Hamilton region, New Zealand. Earth Science Journal, 4(2), 129-140.